



HAL
open science

Thermally driven smart metamaterials

Qingxiang Ji

► **To cite this version:**

Qingxiang Ji. Thermally driven smart metamaterials. *Materials*. Université Bourgogne Franche-Comté; Harbin Institute of Technology (Chine), 2021. English. NNT: 2021UBFCD026 . tel-03454722

HAL Id: tel-03454722

<https://theses.hal.science/tel-03454722>

Submitted on 29 Nov 2021

HAL is a multi-disciplinary open access archive for the deposit and dissemination of scientific research documents, whether they are published or not. The documents may come from teaching and research institutions in France or abroad, or from public or private research centers.

L'archive ouverte pluridisciplinaire **HAL**, est destinée au dépôt et à la diffusion de documents scientifiques de niveau recherche, publiés ou non, émanant des établissements d'enseignement et de recherche français ou étrangers, des laboratoires publics ou privés.



THÈSE DE DOCTORAT EN CO-TUTELLE DE
L'UNIVERSITÉ BOURGOGNE FRANCHE-COMTÉ
ET DE HARBIN UNIVERSITY OF TECHNOLOGY

ÉCOLE DOCTORALE N° 37
SCIENCES POUR L'INGÉNIEUR ET MICROTECHNIQUES

Doctorat de Sciences pour l'ingénieur

PAR

Qingxiang JI

Métamatériaux thermiques
intelligents
*Thermally driven smart
metamaterials*

Soutenance de thèse prévisionnelle à Beijing, Chine, le 30 juillet 2021

Composition du Jury :

Gengkai Hu	President	Professeur, Beijing Institute of Technology
Richard Craster	Rapporteur	Professeur, Imperial College London
Chengwei Qiu	Rapporteur	Professeur, National University of Singapore
Linzhi Wu	Examineur	Professeur, Harbin Engineering University
Muamer Kadic	Encadrant	Maître de conférences, Université Bourgogne Franche-Comté
Vincent Laude	Co-directeur	Directeur de recherche, Université Bourgogne Franche-Comté
Jun Liang	Co-directeur	Professeur, Beijing Institute of Technology
Xiangqiao Yan	Co-directeur	Professeur, Harbin Institute of technology

Acknowledgment

Time flies! Now it comes to the end of my PhD study.

Gone are those wonderful time working with my dear supervisors Prof. Vincent Laude and Prof. Muamer Kadic. I would like to express my deepest acknowledgment to them, for their academic guidance in my researches and kind help in my daily lives, during my stay in Université Bourgogne Franche-Comté. I am deeply impressed by their rich knowledge, high academic levels, strong responsibility, and great sense of humor. I have learned quite a lot from them. These beautiful memory will never perish.

Many thanks to my Chinese supervisors Prof. Jun Liang, Prof. Guodong Fang and Prof. Xiangqiao Yan. They provide me the financial support and academic help in my PhD career. Thanks Sébastien Guenneau and Arnaud Spangenberg for their kind help and guidance. I am also thankful to my colleagues for their technical support and spiritual accompany. Special thanks to Dr. Johnny Moughames, Prof. Gwenn Ulliac, Dr. Julio Andrés Iglesias Martínez, Prof. Cédric Clévy, Dr. Nicolas Laforge, and many lovely guys who are not mentioned in this list.

I greatly acknowledge my best friend Dr. Xueyan Chen for his encouragement and accompany in France. With his perfect skills in cooking, I spent amazing days with delicious food in France. I would like to thank my best friend Dr. Ke Wang who helps me quite a lot in my career. Herein best wishes to her PhD career and happiness to her whole life!

I especially thank my motherland and China Scholarship Council for the financial support of this work. Here special remembrance to the great man Xiaoping Deng who is the founder of this foundation that offers me the opportunity to seek further education in France.

I am particular grateful to my father, mother, sisters and the whole family for their support and understanding during my whole life.

Finally, I owe a debt of gratitude to my wife, Dr. Qinghui Dai, for her selfless dedication and support without reservation. She is the brightest star in my night sky. Hope that my darling will never grow old and will keep young forever.

Contents

	Acknowledgment	iii
	Contents	v
I	Introduction	1
	I.1 Overview of thermal metamaterials	2
	I.1.1 Thermal metamaterials in heat diffusion manipula- tion.....	2
	I.1.2 Thermal metamaterials in heat radiation control.....	4
	I.1.3 Thermal metamaterials based on thermally driven deformation.....	5
	I.2 Objectives of this work	6
II	Thermal metamaterials for non-singular homoge- neous polyhedral heat cloak	9
	II.1 Introduction	10
	II.2 Methods	10
	II.3 Results and discussion	15
	II.3.1 Cloaks with 8 faces	15
	II.3.2 Cloaks with 32 faces	17
	II.3.3 Cloaks with curved boundaries.....	18
	II.3.4 Influence of geometrical parameters	22
	II.3.5 Effectiveness of homogenized multi-layered cloaks....	24
	II.4 Summary	28
III	Homogenization and optimization of thermal meta- materials for heat diffusion control	29
	III.1 Introduction	30
	III.2 Thermal metadevices design based on optimized mi- crostructures	31
	III.2.1 Nonlinear transformation yielding constant anisotropic conductivity	31

	III.2.2 Design and homogenization of the microstructures . . .	33
	III.2.3 Optimization based on Latin hypercube technique . . .	36
	III.2.4 Heat manipulation performances of the designed metade- vice	38
	III.3 Sample fabrication and experimental validation	46
	III.4 Summary	50
IV	Thermal metasurface for selective emission and heat radiation control	51
	IV.1 Introduction	52
	IV.2 Selective emission based on layered medium	52
	IV.2.1 Principle of thermal emission control	52
	IV.2.2 Surface emissivity calculation based on transfer ma- trix method	53
	IV.3 Theoretical realization of Infrared camouflage and other functionalities	56
	IV.4 Summary	61
V	Thermal metamaterials based on thermally driven deformation	63
	V.1 Introduction	64
	V.2 Concept design and samples fabrication	64
	V.2.1 Working mechanism of the bilayer beams	64
	V.2.2 Design of thermally driven smart metamaterials	66
	V.2.3 Fabrication technique	68
	V.2.4 Sample fabrication	72
	V.3 Thermally driven motions	76
	V.3.1 Concept validation	76
	V.3.2 Quantitative analysis on thermally driven motions	78
	V.3.3 Parameter analysis for further optimization	80
	V.4 Thermo-mechanical performances	81
	V.5 Summary	82
	Conclusions and outlook	83
	Bibliography	87

List of Figures 103

List of Tables..... 111

Chapter I

Introduction

I.1	Overview of thermal metamaterials.....	2
	I.1.1 Thermal metamaterials in heat diffusion manipulation...	2
	I.1.2 Thermal metamaterials in heat radiation control.....	4
	I.1.3 Thermal metamaterials based on thermally driven de- formation	5
I.2	Objectives of this work.....	6

I.1 OVERVIEW OF THERMAL METAMATERIALS

I.1.1 Thermal metamaterials in heat diffusion manipulation

Metamaterials are artificial materials that can achieve properties that do not occur naturally, such as negative index of refraction or electromagnetic cloaking. The theoretical properties of metamaterials were first described in the 1960s by Victor Veselago, who focused on the concept of negative index materials [Veselago 06]. Metamaterials have attracted wide scientific interest as promising candidates to achieve unusual effective properties and to realize extraordinary devices such as flat lenses and invisibility cloaks. Cloaking was first performed on electromagnetic waves with the transformation optics approach, based on form-invariance of the governing equations after coordinates transformation [Pendry 06]. In the transformation optics approach, the properties of invisibility cloaks are derived by transforming the virtual space to the physical space (see Fig. I.1a,b). Any shaped object can be “hidden” inside the cloaked space, as illustrated in Fig. I.1. In this design, the derived material property of the coating domain, i.e. negative index of refraction, does not exist in nature, and this has been enabled by using a metamaterial approach.

Beyond electromagnetism [Kadic 13, Schurig 06, Li 08, Chen 10], the transformation optics concept has been widely applied to elastic waves [Milton 06, Bückmann 14, Farhat 09, Brun 09, Bückmann 15, Stenger 12], acoustics [Farhat 08b, Cummer 07, Farhat 08a], and diffusion [Guenneau 13b, Schittny 14, Schittny 15, McCall 18]. Thermal cloaking, on the basis of thermal metamaterials, refers to making an object invisible to heat flows and is achieved by surrounding the object with a predefined heat cloak. Fan *et al.* [Fan 08] exploited shaped graded materials where heat energy was manipulated to transfer from regions of low temperature to regions of high temperature. Guenneau *et.al* [Guenneau 12] firstly proposed a transformed coordinate approach of thermal cloaking in the heat equation and established multi-layered structures with isotropic materials (see I.2), which was verified later by experiments [Schittny 13, Narayana 12, Han 14a, Xu 14]. Researchers have then made great achievements on heat manipulation with various thermal metadevices [Shang 18, Yang 17, Han 13, Han 14b, Li 15, Yang 15, Shen 16, Han 18, Li 19b, Xu 19b].

Thermal cloaks designed by the transformation optics approach have specific properties, which are usually anisotropic (having a thermal property that is different when measured in different directions) and inhomogeneous (having different values when measured at different positions). A thermal cloak covers a coating space and guides the heat flux to pass around the object without going through it. There are no perturbations to the external temperature field when heat flows exit the cloak, as if the object does not exist. The object is thus thermally “invisible”.

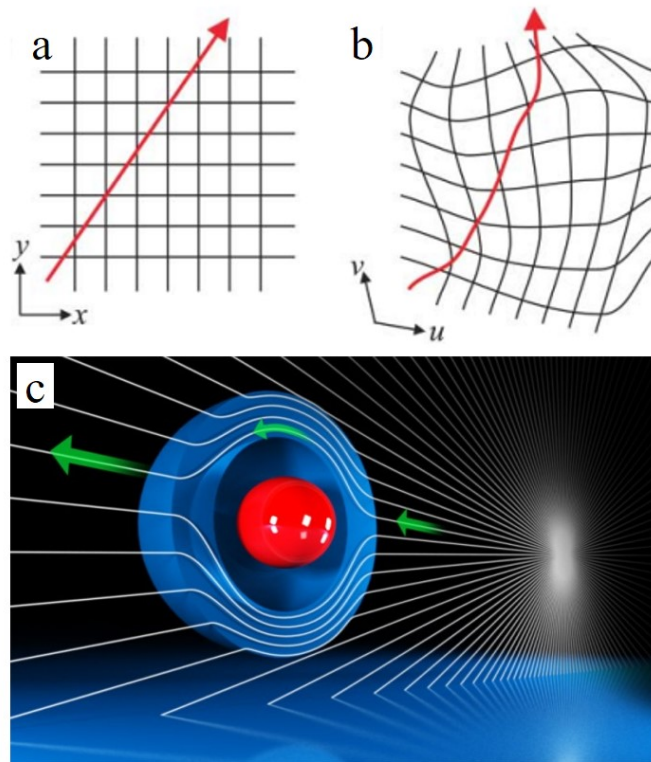


Figure I.1 – The principle of transformation optics: (a) A field line in the virtual space with the background Cartesian coordinate grid shown. (b) The distorted field line in the physical space with the background coordinates distorted in the same fashion. (c) A 3D ray-tracing program has been used to show the cloaking effects. The object (in red) is hidden [Pendry 06].

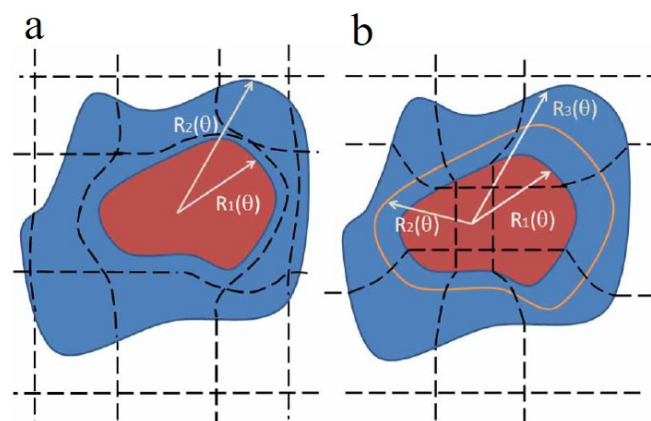


Figure I.2 – The principle of an invisibility cloak and a concentrator for heat flux. Sketch of the transformed metric (dotted lines) for (a) an invisibility cloak and (b) a concentrator. The coating (marked in blue) is realized with metamaterials with anisotropic heterogeneous conductivity. The object is shown in red [Guenneau 12].

In theory, thermal cloaks can be designed by the transformation optics method and realized with thermal metamaterials. However, the material properties of the cloaking region can be so extreme (i.e. infinite, inhomogeneous and anisotropic) that they cannot be built with materials in nature. Also note that since the transformation is not unique, the properties of the devices can be tailored intentionally. Therefore, more contributions are needed for thermal cloaks to be realized facilitating engineering applications.

I.1.2 Thermal metamaterials in heat radiation control

Thermal metamaterials have been designed to realize unusual effective thermal properties in order to create extraordinary devices that manipulate heat fluxes, such as thermal cloaks, thermal concentrators, thermal sensors or thermal illusion devices [Fan 08, Guenneau 12, Guenneau 13a, Kadic 13, Schittny 13, Schittny 14, Han 14b, Fleury 15a, Fleury 15b, Yang 15, Han 18, Qu 18, Ji 21]. These devices are based on heat conduction engineering including via the thermal conductivity tensor and the heat capacity. Furthermore, manipulation of out-of-plane radiation is very important for radiative cooling and thermal camouflage. Thermal camouflage refers to techniques that make a hot object invisible over the background, for instance enabling military targets such as tanks, aircrafts and even humans to evade infrared detection. Thermal camouflage can be realized by matching the detected radiative temperature of an object with its surroundings. By eliminating thermal radiation differences between the object and the background, it is possible to hide or disguise a given object from an observing thermal camera.

According to the Stefan-Boltzmann law, the detected intensity emitted from an object is proportional to the surface emissivity and to the fourth power of the thermodynamic temperature [Siegel 01]. Therefore, one can achieve thermal camouflage by controlling surface temperatures through transformation thermotics and thermo-regulation systems or by tuning the surface emissivity [Sakat 12, Arnold 12, Li 18b, Hong 20, Peng 20]. The later has the advantage of being passive and not to require an additional energy source.

Currently, infrared stealth has been realized by controlling the surface emissivity using metasurfaces [Liu 10, Ueba 12, Moghimi 18, Peng 18, Lee 19, Wang 19, Song 20], phase-change materials [Salihoglu 18, Qu 18, Lyu 19], and stimuli-responsive structures [Vasant 13, Liu 16, Krishna 19, Zhang 19]. These approaches were further developed to obtain adaptive thermal camouflage by dynamically tunable surface emissivity [Inoue 14, Brar 15, Cui 18, Xu 18a, Tang 20] and multispectral camouflage [Chandra 18, Kim 19, Pan 20].

So far, the thermal metamaterial approach is still the main paradigm for infrared camouflage. It requires exploring micro- and nano-structures with well-designed geometries that demonstrate the desired optical properties. This type of surface emissivity control relies on fine tuning the feature size of designed structures. It is therefore challenging to obtain a continuously changing surface emissivity. Most reported works have focused on camouflaging a given object with uniform temperatures [Liu 10, Ueba 12, Moghimi 18, Lee 19, Song 20]. To perfectly cam-

ouffrage a continuously changing thermal field, the required emissivity profile is position-dependent and varies continuously. This problem was tackled by employing a form of discretization, in which a step-wise approximation of ideal emissivity parameters was made at the sacrifice of camouflage performance [Song 20]. Besides, metasurfaces usually require wavelength-scale structures and thereby imply complicated fabrication. Therefore, to propose a easy and practical method that applies to complex thermal field is needed.

I.1.3 Thermal metamaterials based on thermally driven deformation

Mechanical metamaterials, the mechanical branch of metamaterials, are artificial materials with unusual effective mechanical properties that mainly result from structural design rather than from the properties of constituent materials [Florijn 14, Christensen 15, Milton 02, Kadic 19, Zangeneh-Nejad 20]. Using additional physical controls, scientists have designed composite structures that not only go beyond the properties of their constituents but whose effective properties can even have a sign opposite to the latter [Fleury 14, Kadic 15, Koschny 17, Qu 17, Spiegel 19]; they are categorized as stimuli-responsive metamaterials and are also known as 4D metamaterials [Hippler 19a, Hippler 19b, Gernhardt 19]. Mechanical metamaterials have been designed to show superior mechanical properties in various application fields. Taking a metamaterial approach toward the design of soft microrobots substantially increases the number of degrees of freedom in deformation and the available geometrical parameters [Coulais 17, Brandenbourger 19, Rafsanjani 19]. Indeed, the complex behavior of highly deformable mechanical metamaterials can substantially enhance the performance of soft microrobots. Soft shape-matching materials based on mechanical metamaterials were proposed [Mirzaali 18], with potential applications in soft robotics and wearable (medical) devices. Soft actuating materials are capable of changing their macroscopic shapes under external physical stimuli of the mechanical [Hippler 20], the electric [Acome 18, Amjadi 18, Liu 15], the photonic [Shi 17, Han 16], the thermotic [Haines 14, Chin 18], the hygrometric [Han 15a, Castaldo 19, Shin 18, Lee 13], or the magnetic [Tottori 12, Li 19a, Magdanz 13] type. Such stimuli-responsive materials play a key role in designing soft microrobots thanks to their brilliant shape recovery properties under applied stimuli that help the creation of programmable and accurate motion [Wang 12, Kotikian 18, Huang 20].

So far, actuating devices have been designed mainly using multilayered films or beams, exploiting the different physical response of two or more different materials. In the field of thermally driven metamaterials, actuators are usually realized by coupling two layers of materials with different thermal expansion coefficients and Young's moduli [Qu 17, Jiang 14]. However, realizations of actuating metamaterials have to date only been reported for simple deformations like self-bending or been demonstrated for macroscopic structures, at the centimeter or millimeter

scale. It remains a challenge to obtain more complex deformations under external stimuli, such as rotation and translation, by a more direct and practical fabrication approach directly at the microscale.

I.2 OBJECTIVES OF THIS WORK

A challenge for transformation optics based heat cloaks is that they often require inhomogeneous and anisotropic constitutive parameters which are difficult to realize especially for large-scale applications. This challenge is more prominent when dealing with cloaks of complex shapes. As most arbitrarily shaped cloaks can be approximated by polyhedra and further divided into a series of tetrahedra, we propose in the second chapter a linear mapping approach to design cloaks with tetrahedron shapes (i.e. tetrahedral cloaks). Homogeneous material properties of the cloak are straightforwardly obtained from coordinates of typical points. Consequently, most arbitrarily shaped thermal cloaks can be designed using homogeneous materials only. We construct polyhedral cloaks with increasing faces and show numerically that they successfully thermally conceal objects. We then demonstrate that cloaks with curved boundaries can also be obtained using this approach. Basing on the proposed approach, we analyze the effectiveness of the polygonal cloak composed of an alternation of homogeneous isotropic layers, and note that cloaking deteriorates at short times, then gradually become better.

In real applications, the material distributions obtained from transformation optics still need to be mapped onto a practical structure exhibiting predescribed anisotropic heat conduction. Anisotropic materials can be approximated by structures of thin and alternating layers based on effective medium theory [Schurig 06, Chen 10, Schittny 13, Narayana 12]. As the heterogenous constitutive profile is position-dependent and continuous, some form of discretization is required, at the sacrifice of accuracy. Other researchers realized thermal meta-devices with bulk isotropic materials using the scattering-cancellation approach [Han 14a, Zhang 20, Xu 14, Han 18, Xu 19b]. However, these meta-devices are always shaped as regular profiles (cylinder, sphere or ellipse), as the scattering-cancellation method is non-trivial for irregular or complex shapes. In the third chapter, we establish a general design road map to obtain realizable thermal meta-devices utilizing microstructures. We first design a cross-shaped microstructure and apply two-scale homogenization theory to obtain its effective properties. Optimal Latin hypercube technique, combined with a genetic algorithm, is then implemented on the microstructure to achieve optimized geometrical parameters. The optimized microstructure can accurately approximate the behavior of transformed materials. We design such devices and characterize good thermal energy harvesting performances by simulations and experiments. To validate the wide application range of our approach, we illustrate other types of microstructures like split rings and rectangles, and show that they mimic well the required constitutive parameters.

In the fourth chapter, we theoretically present an extremely simple and practicable design based on a multilayer film for infrared stealth, with distinctive advantages of scalability, flexible fabrication, and structural simplicity. Using this simple approach, we demonstrate spatial tunability and continuity in thermal emission. By locally changing the thickness of the coating film, we obtain a continuous change of emissive power and consequently implement thermal camouflage functionality. In addition, we demonstrate other functionalities like thermal illusion and thermal coding by thickness-engineered multilayer films.

Finally, we have designed thermal metamaterials towards microrobots, using thermal stimuli as driving forces. In the last chapter, a soft ultra compact and accurate microrobot is described which can achieve controlled motion under thermal stimuli. The system consists of an organized assembly of two kinds of functional structures: a rotational element and a translational one. Both elements are designed basing upon the principle of the thermo-elastic bilayer plate that bends in response to temperature changes. Samples are fabricated using gray-tone lithography from a single polymer but with two different laser writing powers, thus making each part different in its thermal and mechanical behaviors. Excellent motion-controllable, reversible and stable features in a dry environment are verified by simulations and experiments, revealing broad application prospects for the designed soft micro actuators. In addition, we estimate the potential torque (or force) that the designed structures can produce to move an object. It is found that the proposed unit cells with a temperature elevation $\Delta T = 20\text{K}$ can offer a considerable actuation torque (or force) that is able to move roughly 1000 times their own weight. The system is well controlled by a simple thermo-mechanical process (thermal expansion) in a dry environment. We demonstrate the possibility of building a three-axis microrobot with a single material using single-step lithography and thus bring thermoelastic metamaterials for microrobots closer to real applications. Our proposed design is a highly promising basis paving the way for the next micro-nanorobotic generation.

Chapter II

Thermal metamaterials for non-singular homogeneous polyhedral heat cloak

II.1	Introduction	10
II.2	Methods	10
II.3	Results and discussion	15
	II.3.1 Cloaks with 8 faces	15
	II.3.2 Cloaks with 32 faces	17
	II.3.3 Cloaks with curved boundaries	18
	II.3.4 Influence of geometrical parameters.....	22
	II.3.5 Effectiveness of homogenized multi-layered cloaks.....	24
II.4	Summary	28

II.1 INTRODUCTION

In this chapter we focus on non-regular shaped heat cloaks with simplified material properties. Cloaks with complicated boundaries have been studied in the field of electromagnetism and acoustics [Diatta 09, Zhang 08, Jiang 08, Ma 08, Rahm 08, Zhu 13, Li 14, Nicolet 08]. These transforms were later introduced to heat diffusion fields [Yang 13]. The obtained heat cloaks were inhomogeneous and anisotropic which is difficult to realize. Some researchers studied non regular-shaped cloaks and established systems with homogeneous parts [Li 16, Peralta 17, Wang 10], but they only dealt with limited geometries. Han *et.al* designed arbitrarily two-dimensional polygonal cloaks with homogeneous and non-singular parameters [Han 10], which was realized by Liu *et.al* with four kinds of natural bulk materials in bilayer configuration throughout [Liu 17]. Xu *et.al* designed arbitrarily two-dimensional polygonal thermal harvesting schemes using the linear mapping function [Xu 18b, Xu 19a]. Li *et.al* extended these works to three dimensions and proposed a multistep transformation approach for a tetrahedral acoustic cloak [Li 18a]. However, in Li's nice work, the transformation is realized in three steps. The transformation should be conducted in a certain order as the later transformation step is dependent on the former one. Herein we propose instead a one-step linear mapping for polyhedral cloaks where each transformation is independent. Homogeneous material parameters are obtained in this process, facilitating practical realizations.

It is known that an arbitrary shaped cloak can be approached by polyhedra, but a quantitative analysis based on this approximation was rarely considered [Liu 17, Xu 18b, Xu 19a, Li 18a]. We first show how cloaks with curved boundaries (regular spherical cloak and cylindrical cloak as cases here) are approximated by polyhedra and we demonstrate the good cloaking performances of the approximated cloaks. For non-regular shaped cloaks, the convergence behavior in homogenization process hasn't been studied, and this paper primarily focuses on this problem. We study the convergence behaviour of a multi-layered polygonal cloak in both steady-state and transient state cases. Influences of the cloak's shape and lapse of time on the convergence rate are numerically established.

II.2 METHODS

We first consider a linear transformation from the virtual tetrahedral space with local coordinate axes (x, y, z) to the physical tetrahedral space with local coordinate axes (x', y', z') (see Fig. II.1) by

$$\begin{pmatrix} x' \\ y' \\ z' \end{pmatrix} = \begin{pmatrix} a_{11} & a_{12} & a_{13} \\ a_{21} & a_{22} & a_{23} \\ a_{31} & a_{32} & a_{33} \end{pmatrix} \begin{pmatrix} x \\ y \\ z \end{pmatrix} + \begin{pmatrix} a_4 \\ a_5 \\ a_6 \end{pmatrix}, \quad (\text{II.1})$$

where the coefficients a_{ij} ($i, j=1,2,3$) and a_h ($h = 4, 5, 6$) are constant. Substituting four groups of corresponding vertices in Eq. II.1, we get 12 equations for the 12 coefficients. By solving the 12 equations, we find the transformation coefficients as

$$\begin{bmatrix} a_{11} & a_{12} & a_{13} & a_4 \\ a_{21} & a_{22} & a_{23} & a_5 \\ a_{31} & a_{32} & a_{33} & a_6 \end{bmatrix} = \begin{bmatrix} x'_A & x'_B & x'_C & x'_D \\ y'_A & y'_B & y'_C & y'_D \\ z'_A & z'_B & z'_C & z'_D \end{bmatrix} \begin{bmatrix} x_A & x_B & x_C & x_D \\ y_A & y_B & y_C & y_D \\ z_A & z_B & z_C & z_D \\ 1 & 1 & 1 & 1 \end{bmatrix}^{-1}. \quad (\text{II.2})$$

The transient heat conduction equation without sources can be written as

$$\nabla \cdot (k \nabla T) - \rho c \frac{\partial T}{\partial t} = 0, \quad (\text{II.3})$$

where T represents the temperature, k and ρc are thermal conductivity (in unit of $\text{Wm}^{-1}\text{K}^{-1}$) and the product of density by heat capacity (in unit of $\text{J Kg}^{-1}\text{K}^{-1}$), respectively. According to Ref. [Guenneau 12], this equation is form-invariant under coordinate transformation. Note that the transformed parameters are [Fan 08, Guenneau 12]

$$k' = \frac{JkJ^T}{\det(J)} \quad \text{and} \quad (\rho c)' = \frac{\rho c}{\det(J)}, \quad (\text{II.4})$$

where

$$J = \begin{pmatrix} a_{11} & a_{12} & a_{13} \\ a_{21} & a_{22} & a_{23} \\ a_{31} & a_{32} & a_{33} \end{pmatrix}. \quad (\text{II.5})$$

Now, the coefficient matrix J is a constant matrix which is independent of x , y , and z . As a result, material properties derived from Eq. II.4 are homogeneous.

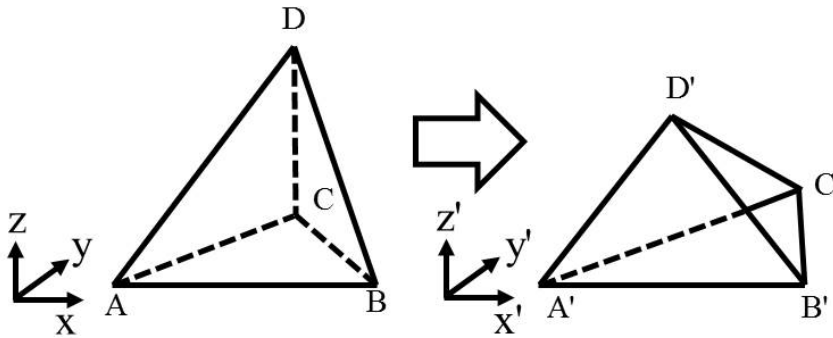


Figure II.1 – Coordinate transformation between two arbitrary tetrahedra. The virtual tetrahedral space (left) is mapped to a physical tetrahedral space (right) by linear transformation.

In Fig. II.2 we show a regular tetrahedral cloak presented by Ref. [Li 18a], where the shadowed domain denotes the designed domain (cloaking domain) while tetrahedron $OA_1B_1C_1$ represents the domain to be cloaked (cloaked domain). For simplicity, we select the edge OA_2 to be along the x -axis, and the face OA_2B_2 in the xoy plane. We further divide the polyhedral cloaking domain into three tetrahedral segments (marked in different colour in Fig. II.2) and apply linear coordinate transformation to each segment. Tetrahedron $A_1A_2B_2C_2$, $A_1B_1B_2C_2$ and $A_1B_1C_1C_2$ in physical space are mapped from $A_0A_2B_2C_2$, $A_0B_0B_2C_2$ and $A_0B_0C_0C_2$ in virtual space (outlined by green lines in Fig. II.2), respectively. Since all the points are located on three edges, we define $OA_0 = \lambda_1OA_2$, $OA_1 = \lambda_2OA_2$, $OB_0 = \mu_1OB_2$, $OB_1 = \mu_2OB_2$, $OC_0 = \varepsilon_1OC_2$ and $OC_1 = \varepsilon_2OC_2$, where λ_i , μ_i and ε_i are all known constants. In the transformation process, the physical space and virtual space are defined by the same coordinates system.

In the nice work by Ref. [Li 18a], where acoustic counterpart is studied, the transformation for a tetrahedron acoustic cloak is completed by multi-steps. In the first step, space $A_0A_2B_2C_2$ is compressed to tetrahedron $A_1A_2B_2C_2$ with transformation matrix J'_1 while space $OA_0B_2C_2$ is extended to tetrahedron $OA_1B_2C_2$ with transformation matrix J'_2 . In the second step, which continues after the first step, space $B_0A_1B_2C_2$ is compressed to tetrahedron $B_1A_1B_2C_2$ with transformation matrix J'_3 while space $OA_1B_0C_2$ is mapped to space $OA_1B_1C_2$ with transformation matrix J'_4 . In the second step, which follows the second step, space $C_0A_1B_1C_2$ is compressed to tetrahedron $C_1A_1B_1C_2$ with transformation matrix J'_5 . Then the Jacobian matrix for tetrahedron $A_1A_2B_2C_2$, $A_1A_2B_2C_2$ and $A_1A_2B_2C_2$ are J'_1 , $J'_3 J'_2$ and $J'_5 J'_4 J'_2$, respectively. We notice that three divided segments undergoes a one-, two-, or three-step transformation in sequence. The three segments should be mapped in a certain order as the later transformation step is dependent on the former one.

In our method, the transformations are all conducted by one step and each transformation is independent. Without losing generality, we first map the points in tetrahedron $A_0A_2B_2C_2$ to the points in tetrahedron $A_1A_2B_2C_2$. Vertices of the given polyhedron in virtual space $A_0(\lambda_1x_{A_2}, 0, 0)$, $A_2(x_{A_2}, 0, 0)$, $B_2(x_{B_2}, y_{B_2}, 0)$ and $C_2(x_{C_2}, y_{C_2}, z_{C_2})$ are mapped to $A_1(\lambda_2x_{A_2}, 0, 0)$, $A_2(x_{A_2}, 0, 0)$, $B_2(x_{B_2}, y_{B_2}, 0)$ and $C_2(x_{C_2}, y_{C_2}, z_{C_2})$ in physical space, respectively. Substituting these four typical coordinates in Eq. II.1, we get the transformation from tetrahedron $A_0A_2B_2C_2$ to tetrahedron $A_1A_2B_2C_2$ by

$$\begin{pmatrix} x'_1 \\ y'_1 \\ z'_1 \end{pmatrix} = \underbrace{\begin{pmatrix} b_{11} & b_{12} & b_{13} \\ b_{21} & b_{22} & b_{23} \\ b_{31} & b_{32} & b_{33} \end{pmatrix}}_{J_1} \begin{pmatrix} x_1 \\ y_1 \\ z_1 \end{pmatrix} + \begin{pmatrix} b_4 \\ b_5 \\ b_6 \end{pmatrix}, \quad (\text{II.6})$$

where

$$b_{11} = \frac{1 - \lambda_2}{1 - \lambda_1},$$

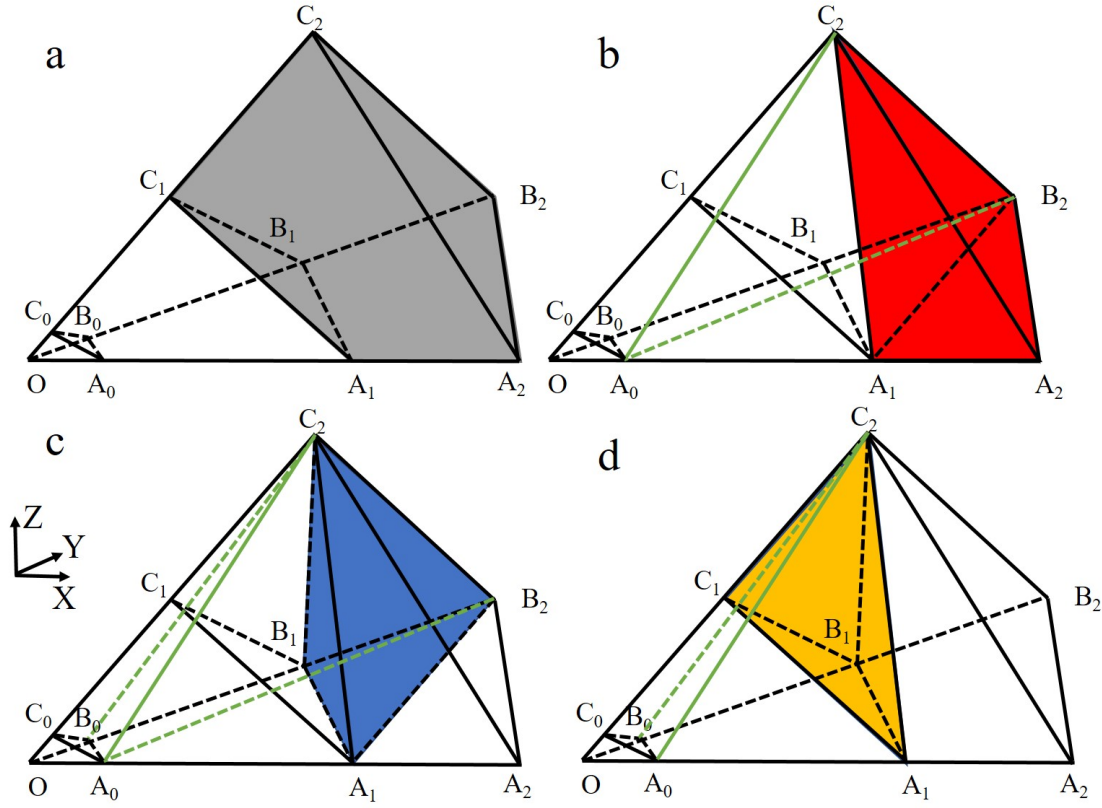


Figure II.2 – Division of a tetrahedron in coordinate transformation: (a) A general tetrahedron cloak and (b-d) the sub-domains of the cloaking domain.

$$\begin{aligned}
 b_{12} &= \frac{\lambda_2 - \lambda_1}{1 - \lambda_1} \frac{x_{B_2} - x_{A_2}}{y_{B_2}}, \\
 b_{13} &= -\frac{\lambda_2 - \lambda_1}{1 - \lambda_1} \frac{x_{B_2}y_{C_2} - x_{C_2}y_{B_2} + x_{A_2}(y_{B_2} - y_{C_2})}{y_{B_2}z_{C_2}}, \\
 b_4 &= \frac{\lambda_2 - \lambda_1}{1 - \lambda_1} x_{A_2}, \\
 b_{22} &= b_{33} = 1, \\
 b_{21} &= b_{23} = b_{31} = b_{32} = b_5 = b_6 = 0.
 \end{aligned}$$

Similarly, the points in tetrahedron $A_0B_0B_2C_2$ are mapped onto tetrahedron $A_1B_1B_2C_2$ by

$$\begin{pmatrix} x'_2 \\ y'_2 \\ z'_2 \end{pmatrix} = \underbrace{\begin{pmatrix} c_{11} & c_{12} & c_{13} \\ c_{21} & c_{22} & c_{23} \\ c_{31} & c_{32} & c_{33} \end{pmatrix}}_{J_2} \begin{pmatrix} x_2 \\ y_2 \\ z_2 \end{pmatrix} + \begin{pmatrix} c_4 \\ c_5 \\ c_6 \end{pmatrix}, \quad (\text{II.7})$$

where

$$\begin{aligned}
c_{11} &= \frac{\lambda_2}{\lambda_1} - \frac{x_{B_2}}{\lambda_1 x_{A_2}} \frac{u_2 - u_1}{1 - u_1}, \\
c_{12} &= \frac{x_{B_2}}{y_{B_2}} \left[\frac{u_2 - u_1}{1 - u_1} \left(\frac{x_{B_2}}{\lambda_1 x_{A_2}} - 1 \right) - \frac{\lambda_2 - \lambda_1}{\lambda_1} \right], \\
c_{13} &= \frac{u_2 - u_1}{1 - u_1} \left[\frac{x_{B_2}}{z_{C_2}} \left(\frac{x_{C_2}}{\lambda_1 x_{A_2}} - 1 \right) - \frac{x_{B_2} y_{C_2}}{y_{B_2} z_{C_2}} \left(\frac{x_{B_2}}{\lambda_1 x_{A_2}} - 1 \right) \right] - \frac{\lambda_2 - \lambda_1}{\lambda_1} \frac{x_{C_2} y_{B_2} - x_{B_2} y_{C_2}}{y_{B_2} z_{C_2}}, \\
c_4 &= \frac{u_2 - u_1}{1 - u_1} x_{B_2}, \\
c_{21} &= -\frac{u_2 - u_1}{1 - u_1} \frac{y_{B_2}}{\lambda_1 x_{A_2}}, \\
c_{22} &= \frac{u_2 - u_1}{1 - u_1} \left(\frac{x_{B_2}}{\lambda_1 x_{A_2}} - 1 \right) + 1, \\
c_{23} &= \frac{u_2 - u_1}{1 - u_1} \left[\frac{y_{B_2}}{z_{C_2}} \left(\frac{x_{C_2}}{\lambda_1 x_{A_2}} - 1 \right) - \frac{y_{C_2}}{z_{C_2}} \left(\frac{x_{B_2}}{\lambda_1 x_{A_2}} - 1 \right) \right], \\
c_5 &= \frac{u_2 - u_1}{1 - u_1} y_{B_2}, \\
c_{31} &= c_{32} = c_6 = 0, \\
c_{33} &= 1.
\end{aligned}$$

The mapping from points in tetrahedron $A_0B_0C_0C_2$ to points in tetrahedron $A_1B_1C_1C_2$ is given by

$$\begin{pmatrix} x'_3 \\ y'_3 \\ z'_3 \end{pmatrix} = \underbrace{\begin{pmatrix} d_{11} & d_{12} & d_{13} \\ d_{21} & d_{22} & d_{23} \\ d_{31} & d_{32} & d_{33} \end{pmatrix}}_{J_3} \begin{pmatrix} x_3 \\ y_3 \\ z_3 \end{pmatrix} + \begin{pmatrix} d_4 \\ d_5 \\ d_6 \end{pmatrix}, \quad (\text{II.8})$$

where

$$\begin{aligned}
d_{11} &= \frac{\lambda_2}{\lambda_1} - \frac{\varepsilon_2 - \varepsilon_1}{1 - \varepsilon_1} \frac{x_{C_2}}{\lambda_1 x_{A_2}}, \\
d_{12} &= \frac{1}{u_1 y_{B_2}} \left[\frac{\varepsilon_2 - \varepsilon_1}{1 - \varepsilon_1} x_{C_2} \left(\frac{u_1 x_{B_2}}{\lambda_1 x_{A_2}} - 1 \right) + \frac{\lambda_2 u_1 - \lambda_1 u_2}{\lambda_1} x_{B_2} \right], \\
d_{13} &= \frac{\varepsilon_2 - \varepsilon_1}{1 - \varepsilon_1} \frac{x_{C_2}}{z_{C_2}} \left[\frac{x_{C_2}}{\lambda_1 x_{A_2}} - \frac{y_{C_2}}{u_1 y_{B_2}} \left(\frac{u_1 x_{B_2}}{\lambda_1 x_{A_2}} - 1 \right) - 1 \right] + \frac{1}{z_{C_2}} \left[\frac{\lambda_2 u_1 - \lambda_1 u_2}{\lambda_1} \frac{x_{B_2} y_{C_2}}{u_1 y_{B_2}} - \frac{\lambda_2 - \lambda_1}{\lambda_1} x_{C_2} \right], \\
d_{21} &= -\frac{\varepsilon_2 - \varepsilon_1}{1 - \varepsilon_1} \frac{y_{C_2}}{\lambda_1 x_{A_2}}, \\
d_{22} &= \frac{\varepsilon_2 - \varepsilon_1}{1 - \varepsilon_1} \frac{y_{C_2}}{u_1 y_{B_2}} \left(\frac{u_1 x_{B_2}}{\lambda_1 x_{A_2}} - 1 \right) + \frac{u_2}{u_1},
\end{aligned}$$

$$\begin{aligned}
 d_{23} &= \frac{\varepsilon_2 - \varepsilon_1}{1 - \varepsilon_1} \frac{y_{C_2}}{z_{C_2}} \left[\frac{x_{C_2}}{\lambda_1 x_{A_2}} - \frac{y_{C_2}}{u_1 y_{B_2}} \left(\frac{u_1 x_{B_2}}{\lambda_1 x_{A_2}} - 1 \right) - 1 \right], \\
 d_{31} &= -\frac{\varepsilon_2 - \varepsilon_1}{1 - \varepsilon_1} \frac{z_{C_2}}{\lambda_1 x_{A_2}}, \\
 d_{32} &= \frac{\varepsilon_2 - \varepsilon_1}{1 - \varepsilon_1} \frac{z_{C_2}}{u_1 y_{B_2}} \left(\frac{u_1 x_{B_2}}{\lambda_1 x_{A_2}} - 1 \right), \\
 d_{33} &= \frac{\varepsilon_2 - \varepsilon_1}{1 - \varepsilon_1} \left[\frac{x_{C_2}}{\lambda_1 x_{A_2}} - \frac{y_{C_2}}{u_1 y_{B_2}} \left(\frac{u_1 x_{B_2}}{\lambda_1 x_{A_2}} - 1 \right) - 1 \right] + 1, \\
 d_4 &= \frac{\varepsilon_2 - \varepsilon_1}{1 - \varepsilon_1} x_{C_2}, \\
 d_5 &= \frac{\varepsilon_2 - \varepsilon_1}{1 - \varepsilon_1} y_{C_2}, \\
 d_6 &= \frac{\varepsilon_2 - \varepsilon_1}{1 - \varepsilon_1} z_{C_2}.
 \end{aligned}$$

Substituting the obtained transformation matrix J_1 , J_2 and J_3 into Eq. (II.4), we get the transformed material properties for each segment. In the above transformation, we assume the tetrahedron $OA_0B_0C_0$ to be void and we map it to the void tetrahedron $OA_1B_1C_1$, thus the object inside is cloaked. Remark that we can still fill the cloaked domain with a medium. Following Ref. [Kohn 08], the transformed parameters for the cloaked domain are given by

$$k'_{in} = \frac{\lambda_1 u_1 \varepsilon_1}{\lambda_2 u_2 \varepsilon_2} \text{diag}\left(\left(\frac{\lambda_2}{\lambda_1}\right)^2, \left(\frac{u_2}{u_1}\right)^2, \left(\frac{\varepsilon_2}{\varepsilon_1}\right)^2\right), (\rho c)'_{in} = \frac{\lambda_1 u_1 \varepsilon_1}{\lambda_2 u_2 \varepsilon_2} (\rho c). \quad (\text{II.9})$$

II.3 RESULTS AND DISCUSSION

II.3.1 Cloaks with 8 faces

We first build an octahedral cloak where OA_2 , OB_2 and OCA_2 lie on the x , y and z axes, respectively (see Fig. (II.3a)). The space to be cloaked is depicted in blue while the cloaking domain is depicted in grey. We split the top and bottom halves into four symmetric tetrahedra. Each tetrahedron is divided into three segments and then mapped following the method outlined in above section. In the octahedral cloak, we set $\lambda_1 = \mu_1 = \varepsilon_1 = 0.01$ and $\lambda_2 = \mu_2 = \varepsilon_2 = 0.5$. For convenience, we normalize the material properties with respect to unit conductivity and heat capacity in background medium. The octahedral cloak is totally divided into 8 tetrahedra and hence 24 segments. Owing to symmetry, we only present material properties of the three representative segments (properties of $A_1A_2B_2C_2$, $A_1B_1B_2C_2$ and $A_1B_1C_1C_2$ are marked with lower case 1,2 and 3, respectively), which are

$$\begin{cases} k_1^p = \text{diag} (0.38, 1.98, 2.58), (\rho c)_1' = 1.98 \\ k_2^p = \text{diag} (39.6, 50, 10.8), (\rho c)_2' = 0.04 \\ k_3^p = \text{diag} (1.98, 5.86, 0.0001), (\rho c)_3' = 0.0008 \end{cases} .$$

Properties of other parts can be easily obtained using symmetries. Numerical simulations are then conducted by COMSOL Multiphysics. We set temperatures of the left boundary (the boundary in negative x axis) and right boundary (the boundary in positive x axis) as $T_L = 2$ K and $T_R = 1$ K, respectively. Other boundaries are thermally insulated to ensure that conduction is the dominant heat transfer mechanism in this case. For clarity, we only show the cloaking performances on two typical sections where the white lines are iso-thermal lines. Simulation results for the steady-state case (see Fig. (II.3b)) show that heat fluxes pass through the object and return to their original trajectory. As a result, the external heat field is not disturbed. For an outside observer, it seems that the heat is transferred through a homogeneous medium.

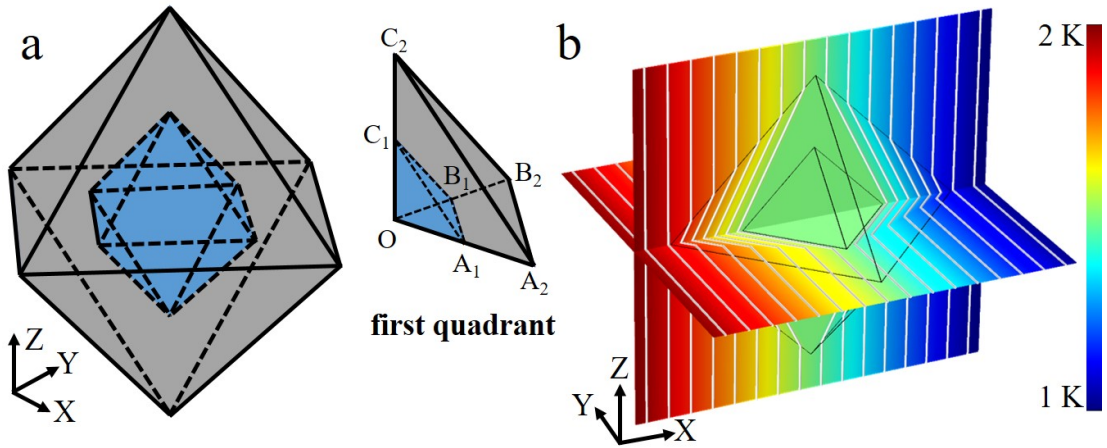


Figure II.3 – Schematic of (a) an octahedral heat cloak and (b) its steady-state cloaking performance.

In the dynamic case, we add perfect matched layer on the right boundary and apply two time-dependent thermal sources on the left boundary, which are $T_1 = T_0 \exp(-t^2/2) + 1$ and $T_2 = T_0 \sin(\pi t/2) + 2$. We set $T_0 = 1$ K and conduct simulations. Good cloaking performances are observed for both cases at different time. In Fig. II.4, we set continuously decreasing temperatures on the left boundary and observe good cloaking effects all the time. In Fig. II.5, we apply periodic thermal boundary on the left and notice that heat energy transfers from left to right. During the transfer process, good cloaking performance is observed at changing thermal profiles.

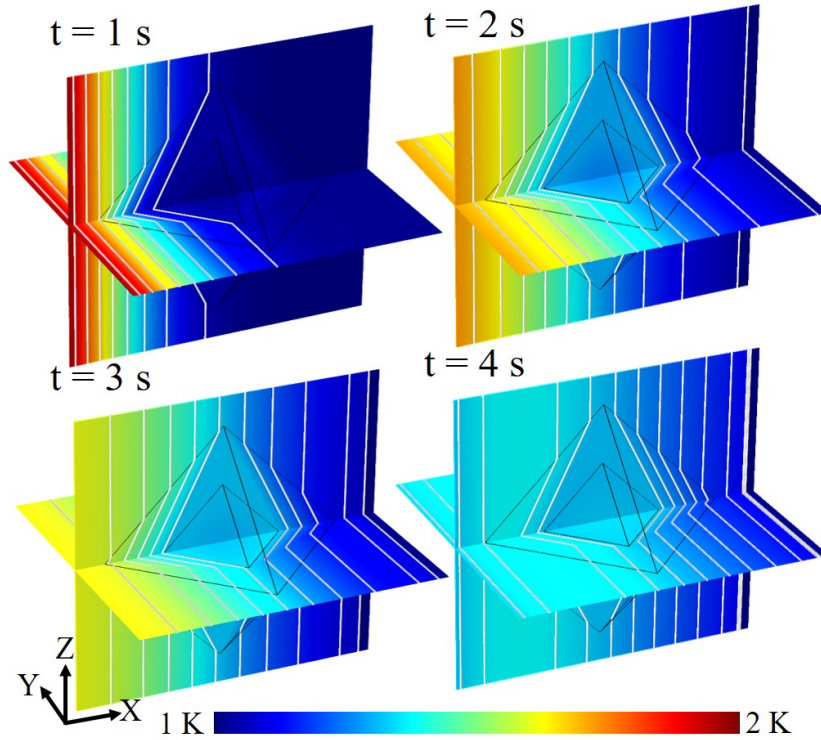


Figure II.4 – Dynamic cloaking performances of the octahedral cloak with the left boundary $T_1 = T_0 \exp(-t^2/2) + 1$.

II.3.2 Cloaks with 32 faces

We also designed more complicated cloaks with 32 faces (see Fig. II.6). Similar to the octahedral cloak, the polyhedral cloak is totally divided into 32 tetrahedra and hence 96 segments. We set $\lambda_1 = \mu_1 = \varepsilon_1 = 0.01$ and $\lambda_2 = \mu_2 = \varepsilon_2 = 0.5$. Owing to symmetry, we only take the parts in the first quadrant as the case and present material properties of the representative segments. In the first quadrant, the cloak is divided in four parts and each part is further divided into 12 segments, material properties of which can be obtained from two representative parts (6 segments) by symmetry. For the central part $OB_2C_2E_2$, the properties of the three segments are

$$\begin{cases} k_1^p = \text{diag}(0.51, 1.98, 1.98), (\rho c)_1' = 1.98 \\ k_2^p = \text{diag}(291.14, 0.05, 0.03), (\rho c)_2' = 0.04 \\ k_3^p = \text{diag}(3.92, 0.0001, 1.98), (\rho c)_3' = 0.0008 \end{cases}.$$

where properties of $B_1B_2C_2E_2$, $B_1C_1C_2E_2$ and $B_1C_1E_1E_2$ are marked with lower case 1,2 and 3, respectively. The other three parts on the edges have similar forms. Therefore, we present the representative part $OA_2B_2C_2$ with one edge on

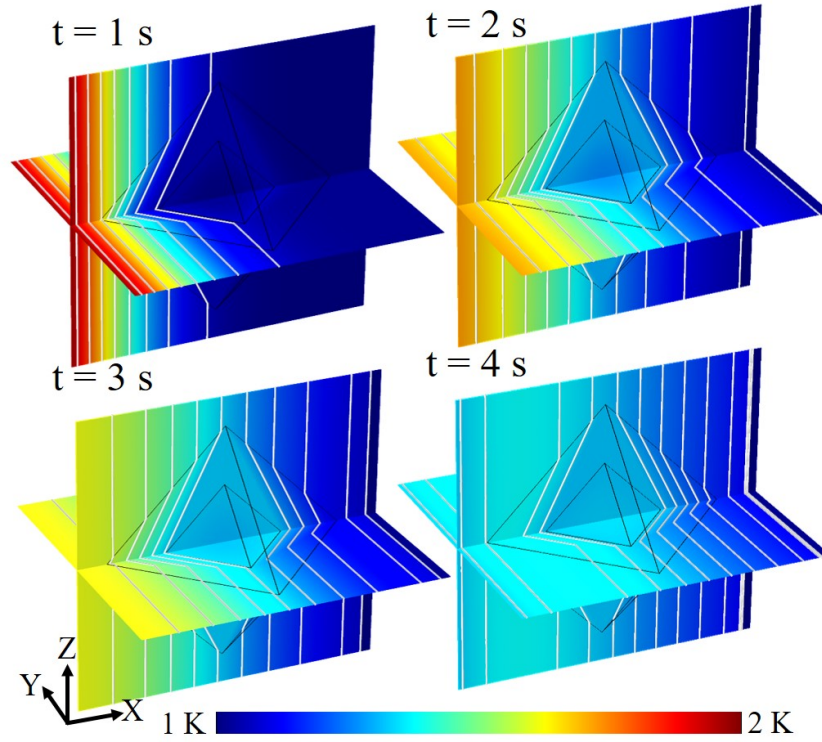


Figure II.5 – Dynamic cloaking performances of the octahedral cloak with the left boundary $T_2 = T_0 \sin(\pi t/2) + 2$.

the x -axis:

$$\begin{cases} k_1^p = \text{diag}(2.286, 0.437, 1.977), (\rho c)_1' = 1.98 \\ k_2^p = \text{diag}(146.755, 0.007, 0.035), (\rho c)_2' = 0.04 \\ k_3^p = \text{diag}(2.647, 0.002, 1.98), (\rho c)_3' = 0.0008 \end{cases} .$$

where properties of $A_1A_2B_2C_2$, $A_1B_1B_2C_2$ and $A_1B_1C_1C_2$ are marked with lower case 1,2 and 3, respectively. Simulation results for the steady-state case (see Fig. II.6b) again show that this polyhedral cloak achieves good cloaking.

In the dynamic case, we apply same boundary conditions as those of the octahedral cloak. In Fig. II.7 and Fig. II.8, good cloaking performances are observed at changing thermal profiles.

II.3.3 Cloaks with curved boundaries

We have shown in above section that the proposed method can be applied to polyhedral cloaks with more faces. Theoretically, an arbitrarily shaped cloak with curved boundaries can be approximated by an arbitrarily large number of polyhedral cloaks, hence our approach applies to a wide range of geometries. For cloaks with curved boundaries, they are firstly approximated as series of tetrahedra and then divided into homogeneous segments. In this process, we approximate the

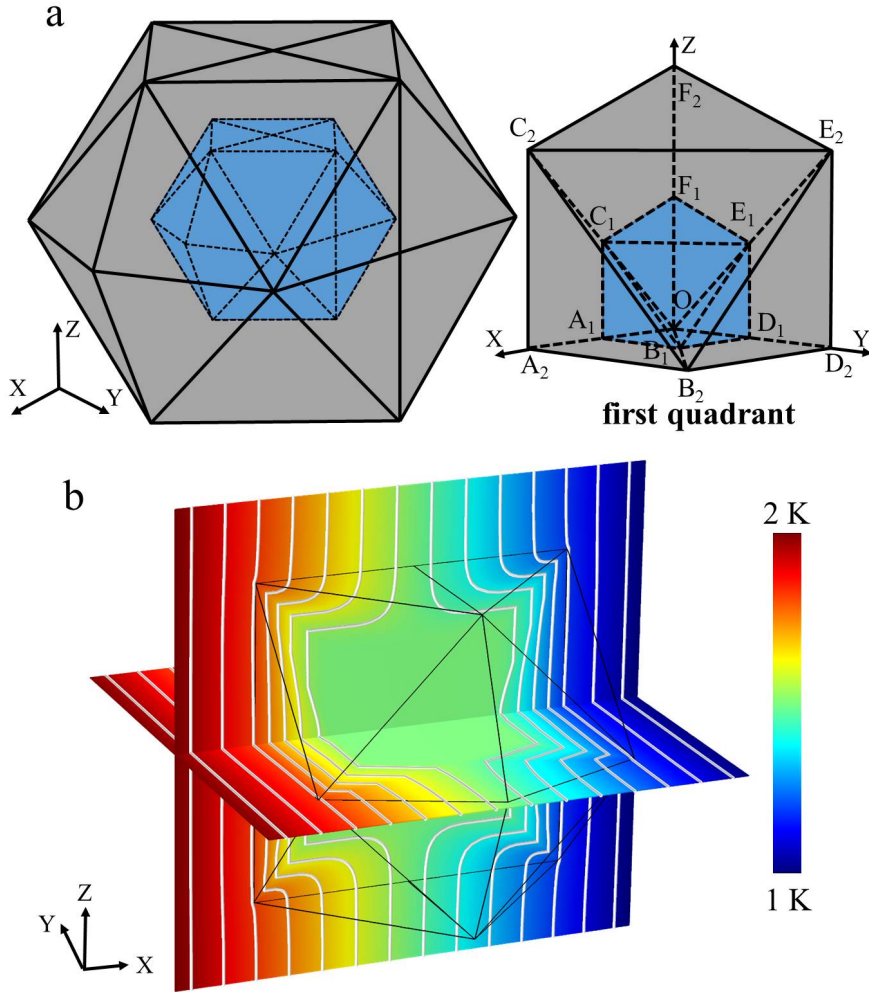


Figure II.6 – Schematic of (a) a polyhedral heat cloak and (b) its steady-state cloaking performance.

curves by piecewise lines and apply a linear transformation on each segment. As an illustration, we show in this section how sphere cloaks and cylindrical cloaks can be obtained by our method.

We built an arbitrary tetrahedron, three vertices of which lie on the surface of the sphere and one vertex lies on the centre (see Fig. II.9). We make simplifying assumptions that

$$\alpha = \beta = \gamma = \theta, \quad \lambda_1 = \mu_1 = \epsilon_1 = \eta_1 \quad \lambda_2 = \mu_2 = \epsilon_2 = \eta_2. \quad (\text{II.10})$$

The tetrahedron will increasingly approximate parts of the sphere as θ decreases. It is also worth noting that the second and third parts (denoted as $A_0B_0B_2C_2$ and $A_0B_0C_0C_2$ in Fig. II.2, respectively) occupy increasingly small relative fractions, and can be negligible as θ approaches 0. Therefore, we mainly focus on the first part. Basing on the approach presented above, we can easily get

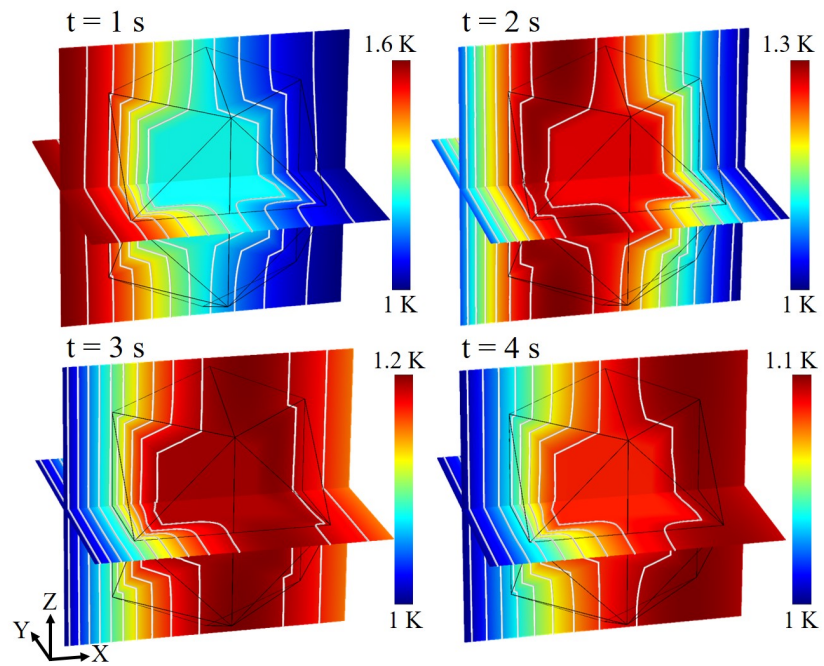


Figure II.7 – Dynamic cloaking performances of the polyhedral cloak with the left boundary $T_1 = T_0 \exp(-t^2/2) + 1$.

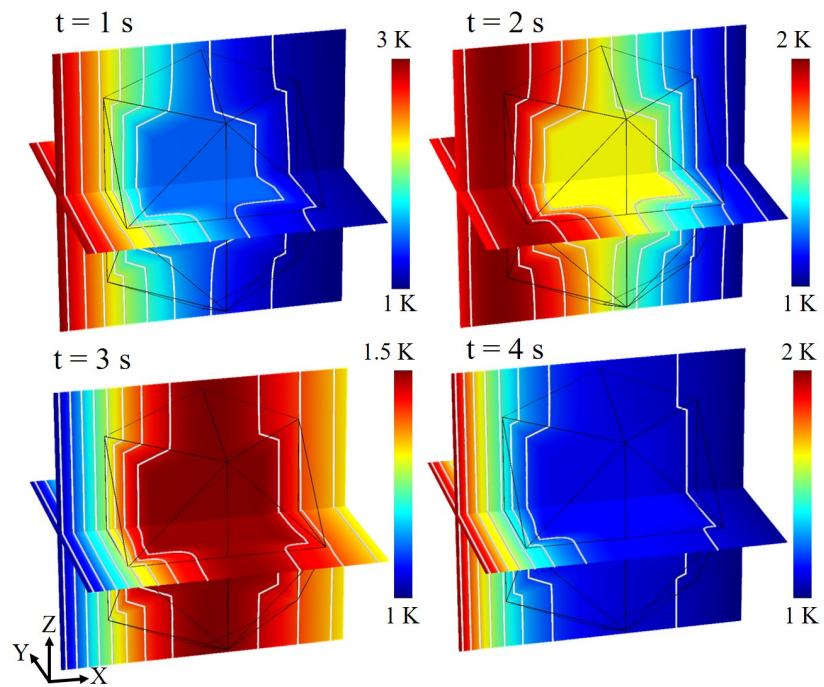


Figure II.8 – Dynamic cloaking performances of the polyhedral cloak with the left boundary $T_2 = T_0 \sin(\pi t/2) + 2$.

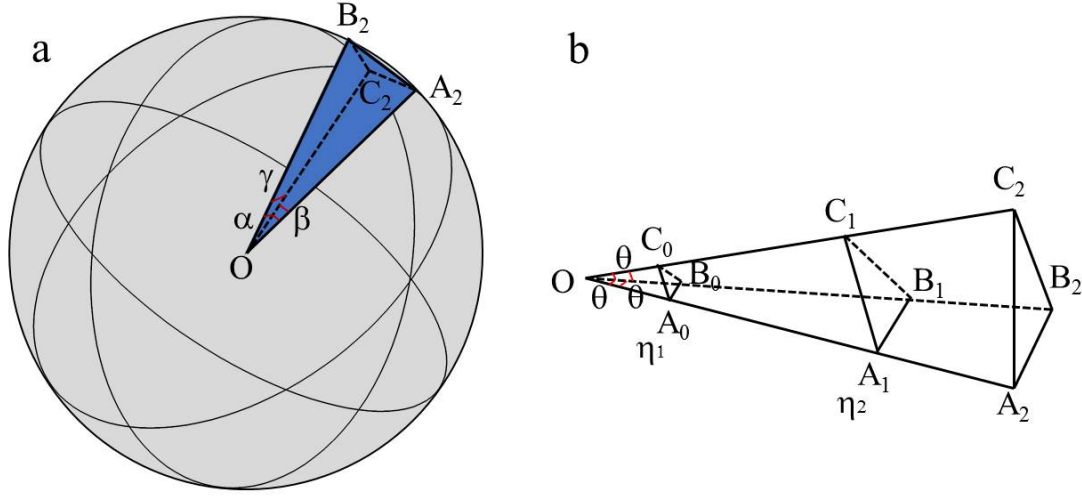


Figure II.9 – Diagram demonstration of (a) an tetrahedron derived from the sphere and (b) the studied tetrahedron with simplifying conditions.

material properties of the tetrahedron as

$$k' = \begin{pmatrix} \frac{1-\lambda_2}{1-\lambda_1} + \frac{2(1-\eta_1)}{1-\eta_2} \left(\frac{\eta_2-\eta_1}{1-\eta_1} \right)^2 \tan(\theta) & -\frac{\eta_2-\eta_1}{1-\eta_2} \tan(\theta) & -\frac{\eta_2-\eta_1}{1-\eta_2} \tan(\theta) \\ -\frac{\eta_2-\eta_1}{1-\eta_2} \tan(\theta) & \frac{1-\eta_1}{1-\eta_2} & 0 \\ -\frac{\eta_2-\eta_1}{1-\eta_2} \tan(\theta) & 0 & \frac{1-\eta_1}{1-\eta_2} \end{pmatrix}, (\rho c)' = \frac{1-\eta_1}{1-\eta_2}. \quad (\text{II.11})$$

As θ approaches 0, the heat conductivity in the principal direction can be expressed as

$$k'_s(\theta \rightarrow 0) = \text{diag} \left(\frac{1-\eta_2}{1-\eta_1}, \frac{1-\eta_1}{1-\eta_2}, \frac{1-\eta_1}{1-\eta_2} \right). \quad (\text{II.12})$$

We build spherical cloaks and conduct simulations where $\eta_2=0.5$ and η_1 is varied. The results In Fig. II.10 show that we can still get cloaking effects using the constitutive properties derived from the polyhedral cloaks. It is also observed that the cloaking performance deteriorates with increasing η_1 , as more and more heat fluxes invade the cloaked domain. When $\eta_1 = 0.5$, there is no physical transformation and hence no cloaking effects at all.

Similarly, we derive the material properties of a cylindrical cloak from the polyhedral approach as

$$k'_c(\theta \rightarrow 0) = \text{diag} \left(\frac{1-\eta_2}{1-\eta_1}, \frac{1-\eta_1}{1-\eta_2}, \frac{1-\eta_1}{1-\eta_2} \right). \quad (\text{II.13})$$

We build cylindrical cloaks and conduct simulations where $\eta_2 = 0.05$ and η_1 is varied. Again, we show that the polygonal approach is also applicable to cylindrical cloaks. The parameter η_1 shows similar influence on the cloaking performance. Though smaller η_1 is desirable in order to improve cloaking, one should consider other influential factors in realizations, e.g. materias anisotropy and availability. A smaller value of η_1 means more difficulties during realization, which we will discuss in the next section.

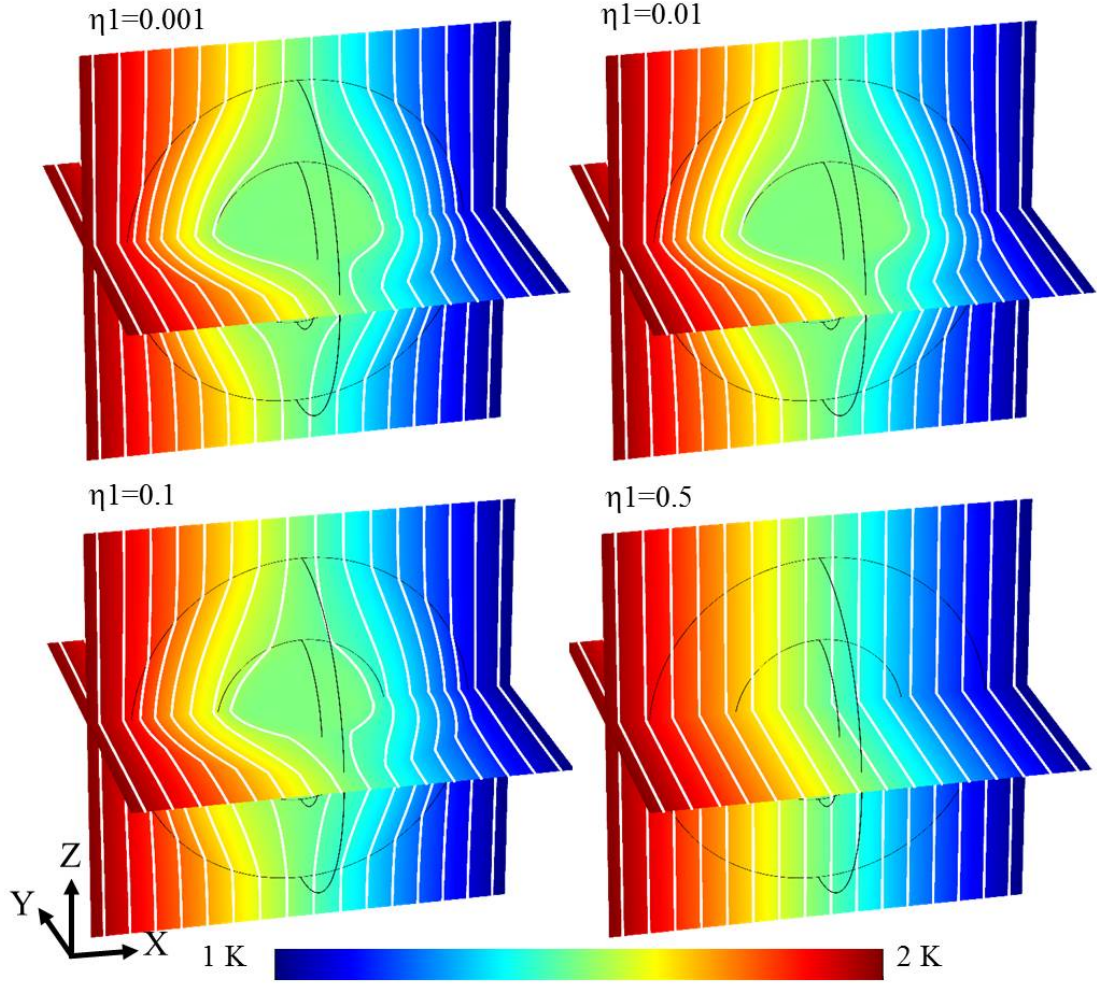


Figure II.10 – Performances of the approximated spherical cloak with varied parameters η_1 .

II.3.4 Influence of geometrical parameters

In the proposed method, we map a small hollow tetrahedron $OA_0B_0C_0$ to tetrahedron $OA_1B_1C_1$, thus the object inside the void tetrahedron is cloaked. As we conduct the transformation from a hollow tetrahedron instead of a point, we can obtain non-singular material properties. This is inspired by the regularized transform first proposed in Ref. [Kohn 08]. We choose the octahedral cloak in above section to illustrate the effect of geometry parameters on cloaking. Without lack of generality, we set $\lambda_2 = \mu_2 = \epsilon_2 = 0.5$ and $\lambda_1 = \mu_1 = \epsilon_1 = \eta_1$ where η_1 is a variable. A perturbation index is introduced to characterize the cloaking performance

$$M_V(t) = \frac{\int_{\Omega} |T(t, x, y, z) - T_r(t, x, y, z)| d\Omega}{\int_{\Omega} d\Omega}, \quad (\text{II.14})$$

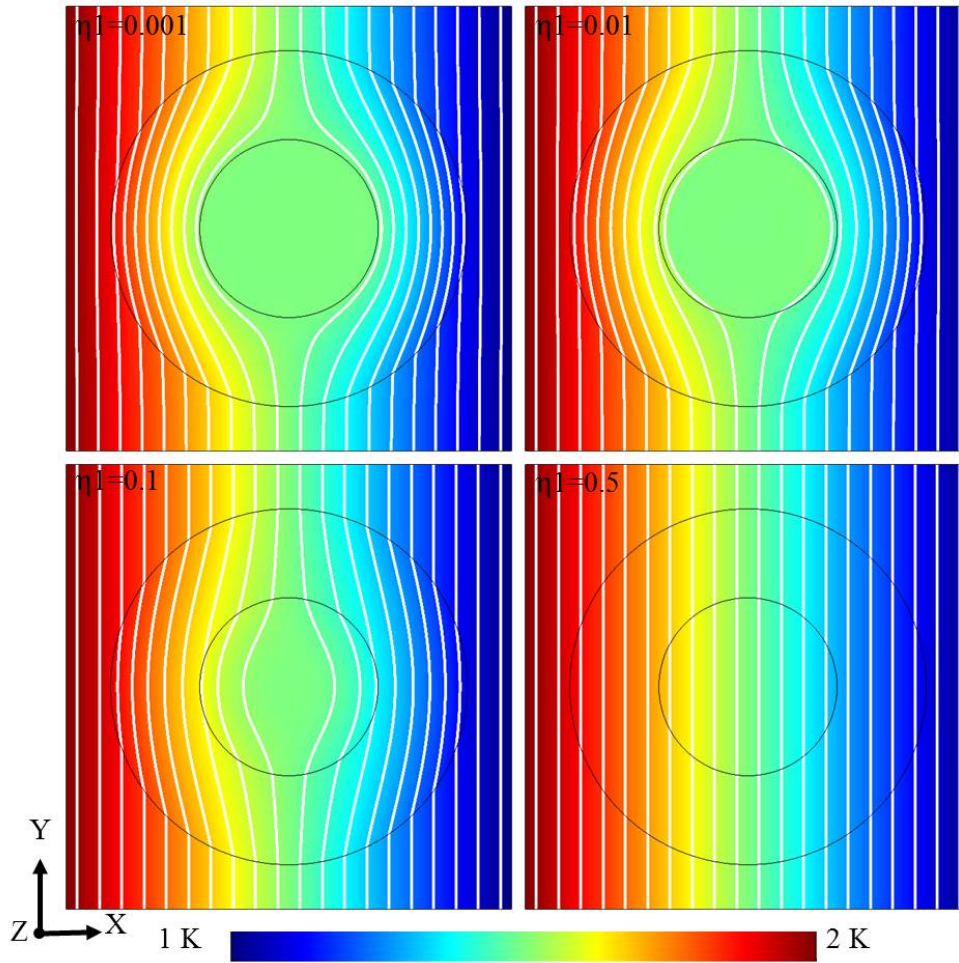


Figure II.11 – Performances of the approximated cylindrical cloak with varied parameters η_1 .

where Ω denotes the probe domain (the domain outside of the thermal cloak). T_r represents temperatures of the homogeneous medium. The index $M_V(t)$ reveals all perturbations of the external heat profile. A lower value of $M_V(t)$ denotes better cloaking performance. For clarity, we use the notation M_V to demonstrate the perturbations in the steady state case where t vanishes. M_v^1 and M_v^2 are employed to reveal the case of only a small hollow tetrahedron and a proposed cloak, respectively. We can observe in Fig. II.12(a) that the two values are always identical, demonstrating the effectiveness of our design. Besides, it can be seen that increasing η_1 results in larger perturbations and thus worsens the effects of cloaking. When η_1 equals the limiting value of 0.5, namely when the tetrahedron $OA_0B_0C_0$ coincides with tetrahedron $OA_1B_1C_1$, there is no cloaking at all.

It seems that we should make η_1 as small as possible to get better cloaking performance. However, the transformed material properties are always beyond the range of natural materials. Geometry parameters determine the material properties and they should be tailored to make the cloaks easier to realize. As we can see

in Fig. II.12, a smaller η_1 means a higher degree of material anisotropy, which poses more difficulties in practical realization. One quantity is necessarily improved at the cost of trading off the other one. Following the results in Fig. II.12(b-d), one should choose the cloaking performances considering the corresponding requirements of materials conductivities.

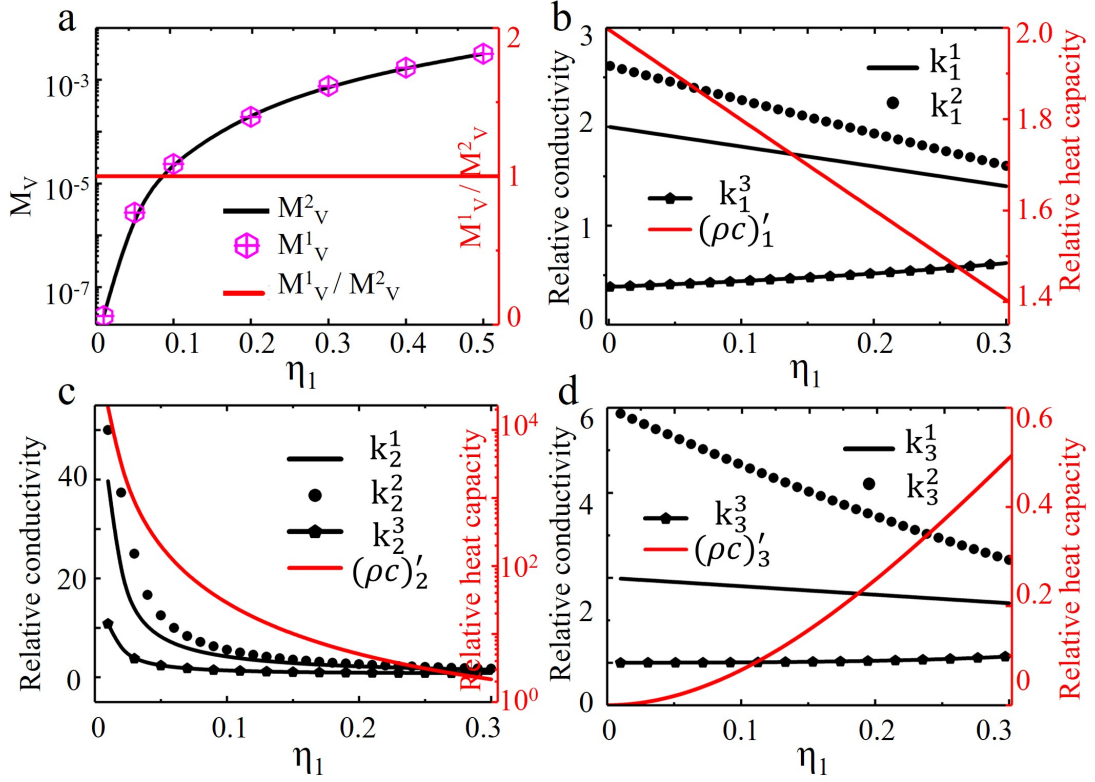


Figure II.12 – Effects of the geometry parameters on cloaking performances and material properties. (a) Comparisons of perturbations between a small hollow tetrahedron and the proposed cloak. (b-d) Materials properties via varied parameters for the three sub-domains.

II.3.5 Effectiveness of homogenized multi-layered cloaks

We have obtained polyhedral heat cloaks with non-singular homogeneous but anisotropic material properties. In real applications, the material parameters still need to be fulfilled by layered structures. For this purpose, we start from alternations of isotropic thin layers with respective constitutive properties $(k_1', \rho_1' c_1')$ and $(k_2', \rho_2' c_2')$. We study a polygonal cloak and derive material properties by the proposed approach. As the designed polygonal cloak is piecewise homogeneous, the constitutive properties are all locally constant and do not depend on the position. The required heat conductivity and product of density by heat capacity can be

approximated by [Guenneau 12]

$$k'_{\perp} = \frac{(l_1 + l_2) k'_1 k'_2}{l_1 k'_1 + l_2 k'_2}, k'_{\parallel} = \frac{l_1 k'_1 + l_2 k'_2}{l_1 + l_2}, \rho' c' = \frac{l_1 \rho'_1 c'_1 + l_2 \rho'_2 c'_2}{l_1 + l_2}, \quad (\text{II.15})$$

where l_1 and l_2 are thickness ratios of the two layers. For the cloak in Fig. II.13, geometrical parameters are $|OA_2| = |OB_2| = 1$, $|OA_1| = |OB_1| = 0.5$ and normalized material properties are $k_1 = 4.96$, $k_2 = 0.20$, $k_3 = 392.03$, $k_4 = 0.0026$. Perpendicular vectors of the layers are $V_{\perp}^1 = (-0.85, -0.52)^T$ and $V_{\perp}^2 = (-0.70, -0.71)^T$, respectively. As Petiteau *et al.* [Petiteau 14] proposed, we can determine quan-

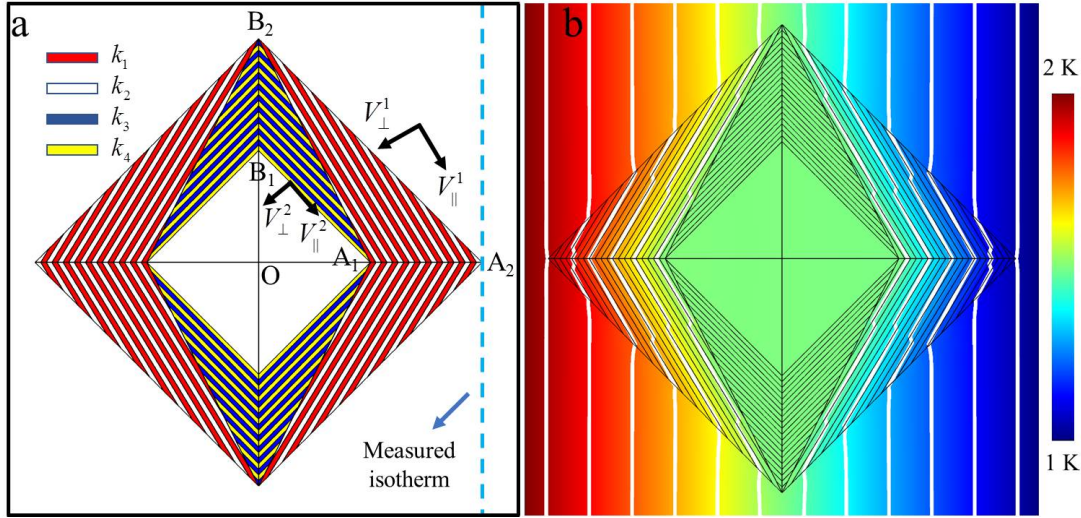


Figure II.13 – Two-dimensional polygonal cloak composed of four isotropic materials (left) and the cloaking performances (right).

tatively the effectiveness of a cloak by evaluating the standard deviation of the isotherms in the vicinity of the cloak. A theoretically perfect cloak gives a standard deviation value of zero for all isotherms outside the cloak as if the medium were completely homogeneous [Petiteau 14]. In the ideal case, all isotherms outside the cloak are straight. In Fig. II.13 we chose the isotherm that passes through vertex A_2 in the diffusion direction as it is the most difficult to straighten.

We performed numerical simulations to check the homogenization convergence as the number of layers N increases. In Fig. II.14, increasing effectiveness (decreasing standard deviation) is observed for multi-layered cloaks as the number of thin layers N increases. We obtain the polynomial fit relationship for the convergence rate as

$$y = -2.2218 - 1.8269x + 0.5347x^2, \quad (\text{II.16})$$

where y is the standard deviation and x is the logarithm of the number of layers: $x = \log_{10}(N)$. Eq. II.16 has a different form from Petiteau's cylindrical cloak [Petiteau 14], demonstrating that the cloak's shape directly determines convergence. Besides, the layered polygonal cloak consists of homogeneous isotropic layers, which is not the case in Petiteau's work where heterogeneous layers are used. This may also have an impact on convergence.

Now the goal is to ascertain that the homogenized multi-layered cloak mimics the perfect cloak (as built by transformed parameters). We derive the standard deviation of the perfect cloak for the measured isotherm by numerical simulations, and substitute the obtained value (8.61×10^{-16} in this case) in Eq. II.16. Direct calculation gives the number of layers required to achieve our goal: $N = 2.3354 \times 10^4$. It is difficult or even impossible to build a nearly perfect cloak with so many layers. However, the convergence analysis provides us with guidance on the number of layers needed for a certain effectiveness tolerance. We note that in Ref.

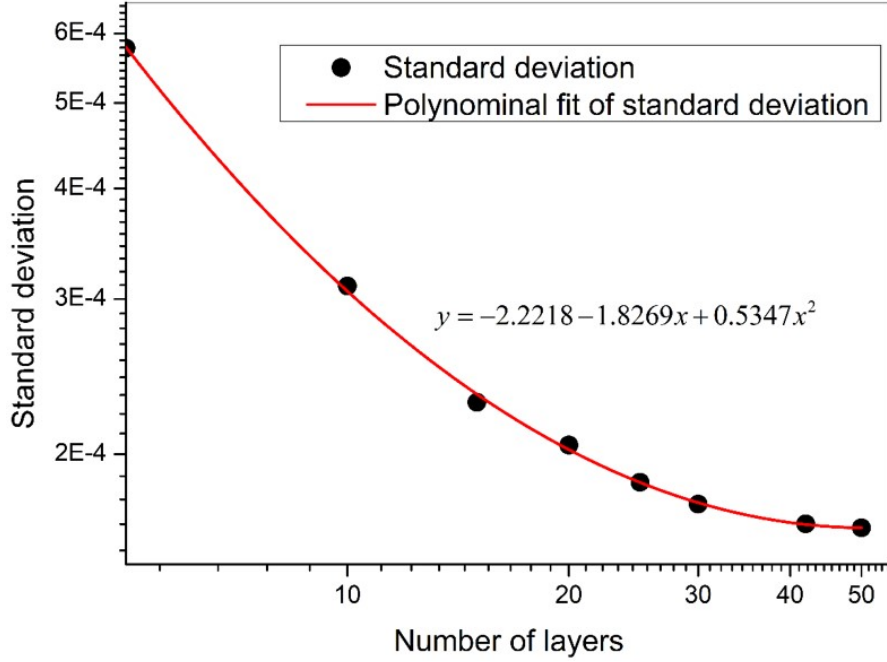


Figure II.14 – Logarithm of the standard deviation for the measured isotherm as a function of $\log_{10}(N)$. For clarity, the values of $\log_{10}(N)$ are replaced by values of N . The convergence rate was obtained by a polynomial fit.

[Craster 18], the following result is established for cloaks with a sufficiently regular (Lipschitz) boundary within a bounded domain Ω of boundary $\partial\Omega$

Proposition 1:

Given $\eta_1 > 0$, there exists a threshold time $t^*(\eta_1) < \infty$ such that for all $t \geq t^*(\eta_1)$ we have

$$\sqrt{\int_{\Omega \setminus \text{cloak}} |T(t, x, y, z) - T_r(t, x, y, z)|^2 d\partial\Omega} \leq C_1 \eta_1^D, \quad (\text{II.17})$$

where C_1 is a constant independent of η_1 and $D = 2, 3$ is the dimension of physical space. This means that after the lapse of a certain threshold time t^* , the temperature field T outside the cloak is close to the temperature field T_r of the uniformly conducting medium irrespective of the conductivity enclosed in the cloaked region. Boundary measurements on $\partial\Omega$ cannot tell apart T and T_r .

We first note that in Ref.[Pakhnin 13], the following homogenization result is established which can be applied to layered cloaks with a sufficiently regular (Lipschitz) boundary

Proposition 2: Given a large enough integer $N > 0$, there exists a threshold time $t^*(N) < \infty$ such that for all $t \geq t^*(N)$ we have

$$\sqrt{\int_{\text{cloak}} |T(t, x, y, z) - T_N(t, x, y, z)|^2 d\Omega} \leq C_2 N^{-1}, \quad (\text{II.18})$$

where C_2 is a constant independent of N , T is the temperature field in the ideal cloak and T_N that in the layered cloak with N layers.

A direct application of the triangular inequality to Propositions 1 and 2 leads to the following result for a bounded domain Ω encompassing either a polygonal ($D = 2$) or a polyhedral cloak approximated by isotropic homogeneous layers:

Corollary: Given a small parameter η_1 and a large enough integer $N > 0$, there exists a threshold time $t^*(\eta_1, N) < \infty$ such that for all $t \geq t^*(\eta_1, N)$ we have

$$\sqrt{\int_{\Omega \setminus \text{cloak}} |T_r(t, x, y, z) - T_N(t, x, y, z)|^2 d\partial\Omega} \leq (C_1 \eta_1^D + C_2 N^{-1}), \quad (\text{II.19})$$

where T_r is the temperature field in the homogeneous medium and T_N that in the homogeneous medium surrounding the layered cloak with N layers.

Using this theoretical result as a guidance, we then compare the effectiveness of the layered cloak and perfect cloak in the transient regime. It is observed in Fig. II.15(a) that the standard deviation for a layered cloak first increases and then gradually decreases with the lapse of time, which demonstrates that a layered cloak approximates well an ideal cloak only after a certain lapse of time, whereas at initial times the approximation will be fairly poor. In Fig. II.15(b) it is shown that the convergence rate is different at different time steps, demonstrating that in the transient regime the convergence depends on both the lapse of time and the shape of cloaks. We should also note that we use four isotropic materials in the layered polygonal cloak. In the approximation of cloaks with curved shapes, we divide the boundary curves into piecewise line sides and we need four materials for each side. Therefore, the number of heat conductivities needed in the homogenization directly depends on the number of divided sides of a cloak. In the two-dimensional case, we will need $4n$ different conductivities and thus $4n$ different types of layers for n sides. As an inhomogeneous spherical or cylindrical cloak can be approximated by a polyhedral cloak with a very large number of sides, this demonstrates that it is always easier to build a polyhedral cloak than a spherical cloak or a cylindrical cloak.

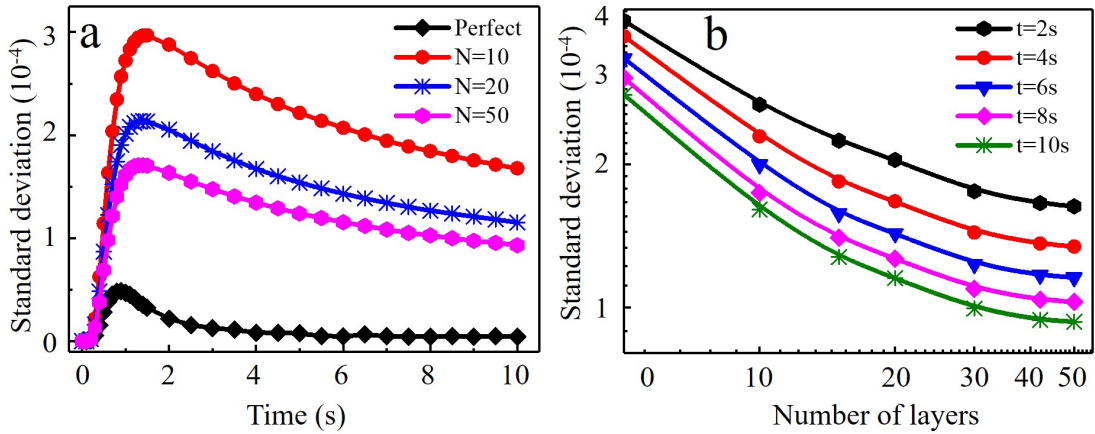


Figure II.15 – Standard deviation of the measured isotherm at different time steps with (a) varied time (b) varied number of layers.

II.4 SUMMARY

We have proposed a method to design three dimensional polyhedral cloaks, where the cloak is divided into tetrahedral parts. Constitutive properties are directly derived from typical coordinates by a straightforward one-step linear mapping. An octahedral cloak and a polyhedral cloak with 32 faces were built to verify the proposed method. Simulation results show that the designed cloaks work well in cloaking objects after a certain lapse of time. As most of arbitrarily shaped cloaks can be approximated by polyhedrons, the proposed method can be applied to a wide range of geometries. As verifying cases, we approximated spherical and cylindrical cloaks by polyhedrons and obtained the approximated material properties. It was shown that the approximated cloaks indeed achieve good cloaking.

The geometrical parameters used in the transformation affect the properties of each segment and thus the cloaking performance. An increment in η_1 provides a larger range of material properties, but at the sacrifice of some cloaking performance. In real applications, the parameters can be flexibly adjusted to achieve a trade-off between cloaking performance and complexity of the material properties.

Finally, we conducted an analysis of the effectiveness of multi-layered cloaks. In the static regime, the cloak's shape directly determines convergence. However, in the transient regime convergence depends on both the lapse of time and the shape of cloaks. The cloaking performance deteriorates at short times, and becomes gradually better after a certain lapse of time.

Chapter III

Homogenization and optimization of thermal metamaterials for heat diffusion control

III.1	Introduction	30
III.2	Thermal metadevices design based on optimized microstructures	31
	III.2.1 Nonlinear transformation yielding constant anisotropic conductivity	31
	III.2.2 Design and homogenization of the microstructures	33
	III.2.3 Optimization based on Latin hypercube technique	36
	III.2.4 Heat manipulation performances of the designed metadvice	38
III.3	Sample fabrication and experimental validation	46
III.4	Summary	50

III.1 INTRODUCTION

Transformation optics, which was the basis to perform cloaking, has been promoted in various physical fields [Schittny 14, Schurig 06, Bückmann 14, Kadic 13, Guenneau 12, Achaoui 20, Kadic 20, Cummer 07, Kadic 11] to create miscellaneous devices, like invisible cloaks [Farhat 09], carpets [Li 08], invisible sensors [Yang 15], illusion devices [Liu 12, Hu 18, Zhou 18] or hyperlenses [Liu 07, Li 09]. Transformation thermodynamics, a counterpart of transformation-optics, has been proposed to guide heat flux in thermal manipulation and generate novel thermal meta-devices, such as heat cloaks, thermal energy harvesting devices, thermal sensors, etc [Fan 08, Shen 14, Xu 20, Qin 19, Liu 17, Schittny 13, Han 14b, Peng 19, Huang 19]. Thermal energy harvesting devices, which can focus and harvest ambient thermal energy without severe perturbations to the heat profile outside the devices, have vast potential in improving the energy-conversion efficiency of existing technologies [Xu 18b].

Thermal meta-devices often require extreme constitutive parameters which are difficult to realize especially for large-scale applications. As the heterogeneous constitutive profile is position-dependent and continuous, some form of discretization is required. Moreover, anisotropic materials can be approximated by structures of thin and alternating layers based on effective medium theory [Schurig 06, Chen 10]. Thermal devices following this principle were fabricated and experimentally characterized [Schittny 13, Narayana 12]. In these works, step-wise approximation of the ideal parameters were made, which sacrificed the performances to reduce fabrication difficulty. Other researchers realized thermal meta-devices with bulk isotropic materials using the scattering-cancellation approach [Han 14a, Zhang 20, Xu 14, Han 18, Xu 19b]. Following this approach, a class of solar-shaped thermal harvesting devices were demonstrated, which could manipulate and concentrate the heat flux using natural materials without singularities [Chen 15, Han 13]. However, these meta-devices are always shaped as regular profiles (cylinder, sphere or ellipse), as the scattering-cancellation method is non-trivial for irregular or complex shapes. In some works, topology optimization method is applied to design thermal meta-devices, where the optimized structures always occupy irregular shapes that impose high requirements on fabrication [Fujii 19, Fujii 20, Alekseev 19].

Except for the mentioned strategies, do we have methods that can both offer good performance and fabrication simplicity? The answer is positive. Researchers [Mei 07, Torrent 08] demonstrated that the constitutive medium can be approximated by microstructures in the context of acoustic metamaterials. Thanks to similarities between the governing equations for acoustic and thermal fields, a similar approach can be implemented for thermal metamaterials. Then the key problem is to determine the effective property of the built microstructure and find the proper parameters of the microstructure to mimic desired transformed parameters. Ji *et al.* [Ji 18] achieved thermal concentration using fiber reinforced microstructures based on simplified effective medium theory. Pomot *et al.* [Pomot 20] realized

acoustic cloaking by microstructures with several types of perforations, combined with a genetic algorithm. We note that the partial differential equations (PDEs) therein have the same structure to the heat equation in the static limit, in which case one simply has to replace the density by the conductivity and all the asymptotic analysis carries through. Moreover, PDEs in Ref. [Pomot 20] are supplied with homogeneous Neumann boundary conditions that stand for rigid walls in acoustics, and insulating walls in thermodynamics. It is thus tempting to implement homogenization and effective medium theories similar to those already used in acoustic metamaterials, however bearing in mind that in the dynamic regime the acoustic wave (elliptic) PDE and the heat diffusion (parabolic) PDE are very different in nature.

In this chapter we focus on the thermal field and establish a general design road map to obtain realizable thermal harvesting devices utilizing micro-structures. We apply two-scale homogenization theory to determine the equivalent thermal properties and employ the Optimal Latin-Hypercube technique to obtain desired design parameters. Beyond this problem, the process is applicable to other microstructures and to wave problems (such as in acoustics). We stress that because of their complexity, the microstructures we investigate here would be challenging to achieve otherwise. We numerically characterize such thermal harvesting devices with natural materials and verify their harvesting efficiency by finite element simulations. Samples are manufactured by CNC machining technique and experiments are conducted. The experimental results agree with simulations, verifying the effectiveness of our design.

III.2 THERMAL METADEVICES DESIGN BASED ON OPTIMIZED MICROSTRUCTURES

III.2.1 Nonlinear transformation yielding constant anisotropic conductivity

We recall the transformed parameters aforementioned as

$$k' = \frac{JkJ^T}{\det(J)} \quad \text{and} \quad (\rho c)' = \frac{\rho c}{\det(J)}. \quad (\text{III.1})$$

The transformed conductivity k' derived by Eq. (III.1) is anisotropic and space dependent, which is difficult to achieve in practice. To remove the singularities and make the proposed device simpler to realize, we choose the following nonlinear transformation instead of the linear one.

Assuming that we map the virtual space $\Omega(r)$ onto the physical space $\Omega'(r')$ by a general two-dimensional radial transformation, of which the inverse mapping function is defined by $r' = g(r')$. Following Eq. II.4, the transformed conductivity

components in polar coordinates can be obtained as

$$\frac{k'_r}{k_b} = \frac{g(r')}{r' g'(r')} \quad \text{and} \quad \frac{k'_\theta}{k_b} = \frac{r' g'(r')}{g(r')}, \quad (\text{III.2})$$

In our work, we require that k'_r/k_b (or k'_θ/k_b) has a constant value C (or $1/C$) with $C > 1$ throughout the designed shell region. k_b denotes thermal conductivity of the background medium. The resulting ordinary differential equation for the mapping function $g(r')$ is

$$\frac{g(r')}{r' g'(r')} = C, \quad (\text{III.3})$$

which has a general solution

$$g(r') = C_1 r_1 \left(\frac{r'}{r_1} \right)^{\frac{1}{C}}, \quad (\text{III.4})$$

where C_1 is a dimensionless constant to be determined. Here, r_1 and r_2 are the inner radius and the outer radius of the designed shell region, respectively. A rigorous transformation maps the virtual space $r = [0, r_2]$ onto $r' = [r_1, r_2]$, which can not be satisfied by Eq. III.4. We propose a dimensionless small positive parameter s and map $r = [r_1 s, r_2]$ onto $r' = [r_1, r_2]$, which approximates the rigorous transformation asymptotically. Applying corresponding conditions $g(r_1) = r_1 s$ and $g(r_2) = r_2$ to Eq. III.4 gives

$$C_1 = \left(\frac{r_1}{r_2} \right)^{\frac{1}{C}-1}, \quad (\text{III.5})$$

which results in the transformation mapping function

$$g(r') = \left(\frac{r_1}{r_2} \right)^{\frac{1}{C}-1} r_1 \left(\frac{r'}{r_2} \right)^{\frac{1}{C}}, \quad (\text{III.6})$$

or

$$r' = r_2 \left(\frac{r}{r_2} \right)^C. \quad (\text{III.7})$$

Following this transformation approach, we derive the constant radial (k'_r) and tangential heat conductivity (k'_θ) in cylindrical coordinates as

$$\frac{k'_r}{k_b} = C \quad \text{and} \quad \frac{k'_\theta}{k_b} = \frac{1}{C}. \quad (\text{III.8})$$

In stark contrast to the material parameters obtained from rigorous linear transformation, such a device is homogeneous in materials composition and its performance is only determined by the thermal-conduction anisotropy (characterized by constant C). We employ this geometric transformation as it avoids the need for extreme spatially-varying parameters and thus the transformed medium will be much easier to implement in practice. Moreover, it is enough for the proof-of-concept demonstration. We stress that the method we describe is indeed also applicable to the design of rigorous transformation-based thermal devices.

III.2.2 Design and homogenization of the microstructures

For clarity, we outline the design process for the general case with a specific example. Assume that we create a cylindrically symmetric thermal harvesting device with inner radius $r_1 = 0.01$ m and outer radius $r_2 = 0.04$ m (see Fig. III.1). The proposed device can harvest thermal energy from the surroundings and concentrate it into the inner domain $r' < r_1$. Heat energy density in the inner domain is thus significantly increased. In our design, the thermal conductivity of the background is $k_b = 132 \text{ Wm}^{-1}\text{K}^{-1}$. We set $C = 2$, which implies that for the shell region we have $k'_r = 264 \text{ Wm}^{-1}\text{K}^{-1}$, $k'_\theta = 66 \text{ Wm}^{-1}\text{K}^{-1}$. Now we turn to the realization of shell region parameters by two natural materials A and B through optimized microstructures. The material distributions in Eq. (III.8) need

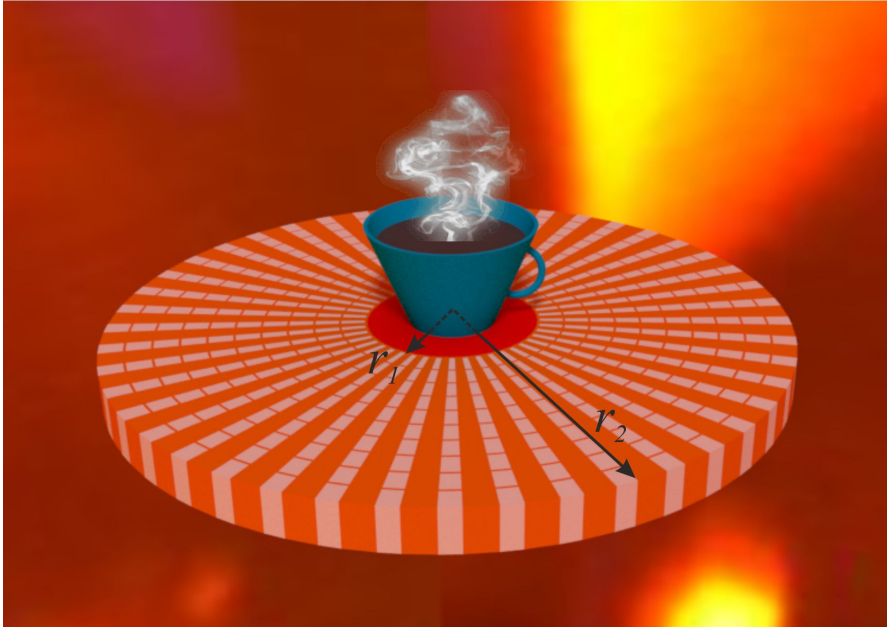


Figure III.1 – Schematic representation of a possible realization of the thermal harvesting device. The shell displays some periodicity along the azimuthal direction, which is a hallmark of a concentrator. Such a device can harvest thermal energy from its surroundings. Heat flows are concentrated into the inner domain $r' < r_1$ thanks to the designed shell region $r_1 \leq r' \leq r_2$.

to be mapped onto a microstructure exhibiting prescribed constitutive parameters. We build a medium with identical elementary cells repeating periodically in space (see Fig. III.2). Generally, the well-established effective medium theory plays a dominant role in determining effective properties and is easy and direct for simple geometries. When designing meta-devices with complex-shaped structures, however, it would be far from trivial to evaluate the equivalent properties. Here we apply instead two-scale homogenization theory [Zolla 03] to determine effective parameters with an asymptotic approach. We consider a two-dimensional periodic

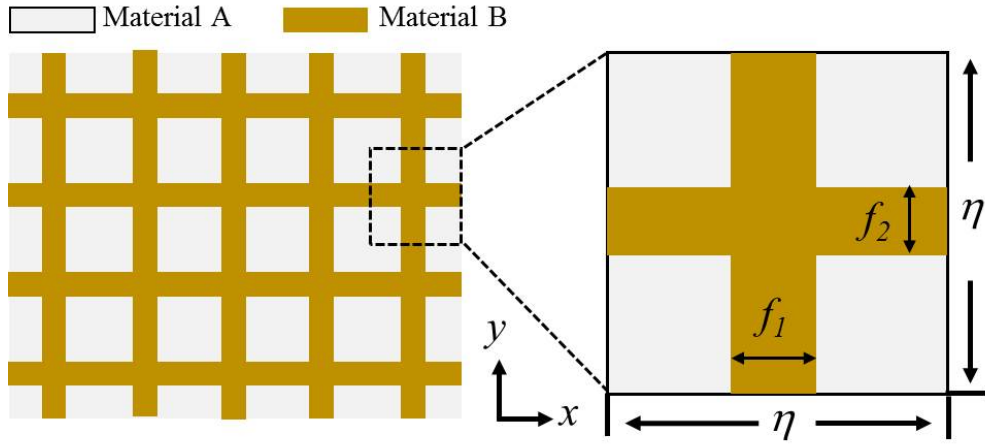


Figure III.2 – Schematic illustration of 2D periodic lattices defined by 2 parameters (area fractions f_1 and f_2). We choose this microstructure to mimic the desired medium of the shell region through homogenization and optimization.

medium with square elementary cells $[0, \eta]^2$ of side-length $\eta \ll 1$. The solution T_η of the steady-state heat equation with fast oscillating parameters $A_\eta = k(x/\eta, y/\eta)$

$$\nabla \cdot (k_\eta \nabla T_\eta) = 0 \quad (\text{III.9})$$

two-scale converges [Allaire 92], when η tends to zero, to the solution T_{hom} of the homogenized heat equation

$$\nabla \cdot (k_{hom} \nabla T_{hom}) = 0. \quad (\text{III.10})$$

The effective property of the periodic medium is given by

$$k_{hom} = \begin{pmatrix} \langle k \rangle - \langle k \partial_x V_1 \rangle & -\langle k \partial_x V_2 \rangle \\ -\langle k \partial_y V_1 \rangle & \langle k \rangle - \langle k \partial_y V_2 \rangle \end{pmatrix}, \quad (\text{III.11})$$

where $\partial_x := \partial/\partial x$, $\partial_y := \partial/\partial y$ and $\langle \cdot \rangle$ denotes the mean operator over the periodic cell. $V_1(x, y)$ and $V_2(x, y)$ are solutions defined up to an additive constant of auxiliary problems of thermostatic type on the periodic cell [Zolla 03]:

$$\begin{cases} \nabla \cdot [k(x, y) \nabla (V_1 - x)] = 0 \\ \nabla \cdot [k(x, y) \nabla (V_2 - y)] = 0 \end{cases}. \quad (\text{III.12})$$

We solve the auxiliary problems in weak form by using COMSOL Multiphysics, which sets up the finite element problem with periodic conditions imposed to the field on opposite ends of the elementary cell. We note in passing V_1 and V_2 are unique solutions of Eq. (III.12) up to additive constants, but these constants do not affect the homogenized conductivity, as one can see that in Eq. (III.11) only the partial derivatives of V_1 and V_2 are involved. The potentials $V_1(x, y)$ and $V_2(x, y)$ of an illustrative case ($f_1 = 0.6576$, $f_2 = 0.0835$) are shown in Fig. III.3, where we obtain the effective conductivity as

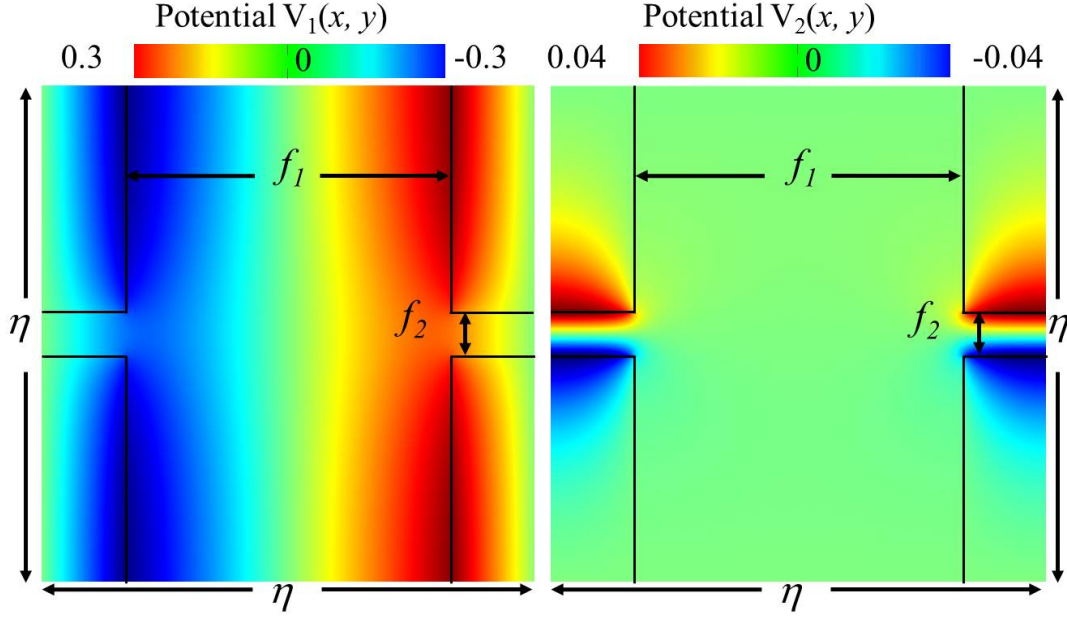


Figure III.3 – Potentials $V_1(x, y)$ and $V_2(x, y)$ of the illustrative case where $f_1 = 0.6576$, $f_2 = 0.0835$.

$$k_{hom} = \begin{pmatrix} 66.01 & 3.3 \cdot 10^{-11} \\ -1.2 \cdot 10^{-11} & 263.97 \end{pmatrix} \approx \begin{pmatrix} k_1 & 0 \\ 0 & k_2 \end{pmatrix}. \quad (\text{III.13})$$

It is noticed that in Eq. (III.13) the off-diagonal components are almost negligible and originate from numerical errors. The resulting spurious artificial anisotropy can be safely ignored. We emphasize that with the finite element method, the effective tensor can be obtained for any periodic composite and that the same technique was implemented before in acoustics [Pomot 20] and electromagnetism [Zolla 03], in which case the effective density and permittivity tensors can be deduced from the same annex problems as in our thermal case.

The effective properties of the medium can be tuned by several design parameters such as geometrical (here we use area fractions f_1 and f_2) and material properties (thermal conductivities k_A and k_B). We restrict our attention here to predefined material properties and set the geometrical parameters as variables. Our goal is to find the set of geometrical parameters which properly mimic the homogenized medium. Therefore, the geometry of elementary cells should be tuned to obtain desired equivalent properties. Considering the heavy workload of the trial-and-error method, we implement an Optimal Latin hypercube technique to solve the problem. We note here that the two-scale homogenization technique has been already used to design a thermal concentrator similar to the one shown in Fig. III.1 and to show that a concentrator consisting of concentric layers would require some complex valued conductivities with sign-shifting imaginary parts [Petiteau 15]. In the present case, we investigate doubly periodic designs and thus we do not face such pitfalls.

III.2.3 Optimization based on Latin hypercube technique

Optimal Latin Hypercube Sampling (OLHS) technique is applied to optimize the spatial positions of control points. The aim of this process is to design a matrix where the sample points spread as evenly as possible within the design region. This method is efficient and robust due to its enhanced stochastic evolutionary algorithm and significant reduction in matrix calculations to evaluate new/modified designs during searching [Park 94]. In this work, we pre-define the two materials as air ($k_A = 0.026$) and copper ($k_B = 400$) in units of $\text{Wm}^{-1}\text{K}^{-1}$ and select the geometrical (area fraction) parameters f_1 and f_2 as design variables. The ranges of these variables are defined as $0.5 < f_1 < 0.8$ and $0.05 < f_2 < 0.1$ after initial estimation. We generate one hundred sample points by OLHS technique, and calculate corresponding effective thermal conductivity of the periodic medium for each sample point using the two-scale homogenization theory. We emphasize the importance of choosing proper ranges of the variables. If, for instance, we use much larger ranges for f_1 and f_2 , the derived values can be less accurate unless a more refined discretization (more sample points) is chosen.

We then create an approximation surrogate model from the obtained one hundred space samples [Mak 00]. The surrogate model is built by the Elliptical Basis Function Neural Network technique which establishes a relation between design targets (k_1 and k_2) and variables (f_1 and f_2), as shown in Fig. III.4 (a-b).

We use two estimators to evaluate the reliability of the surrogate model, the coefficient of determination (R^2) and the root mean square error (RMSE). These are defined as

$$R^2 = 1 - \frac{\sum_{i=1}^m (y_i - \hat{y}_i)^2}{\sum_{i=1}^m (y_i - \bar{y}_i)^2}, \quad (\text{III.14})$$

$$\text{RMSE} = \sqrt{\frac{\sum_{i=1}^m (y_i - \hat{y}_i)^2}{m}}, \quad (\text{III.15})$$

where y_i and \hat{y}_i are respectively the real value and the predicted value of the objective function over the same sample points, \bar{y}_i is the mean value of all objective functions and m is the total number of sampling points. The closer R^2 is to 1 and RMSE is to 0, the more accurate the model. In Fig. III.4 (c-d), we can observe that the predicted values (values obtained by the surrogate model) are in good agreement with the actual values (values on the sample points).

The calculated R^2 and RMSE are listed in Table III.1. The average error and the maximum error among all samples are also shown. In the constructed surrogate models, R^2 is larger than 0.99997 and RMSE are smaller than 0.00012. The maximum error remains close to 0, which demonstrates that the surrogate model is accurate.

Now we proceed with the inverse homogenization problem, that is, we want to find the particular set of design parameters which best mimic the transformed medium [Cherkaev 01]. The optimization problem amounts to minimizing the objective function:

$$E(k_1, k_2, \alpha, \beta) = \alpha |k_1 - k'_r| + \beta |k_2 - k'_\theta|, \quad (\text{III.16})$$

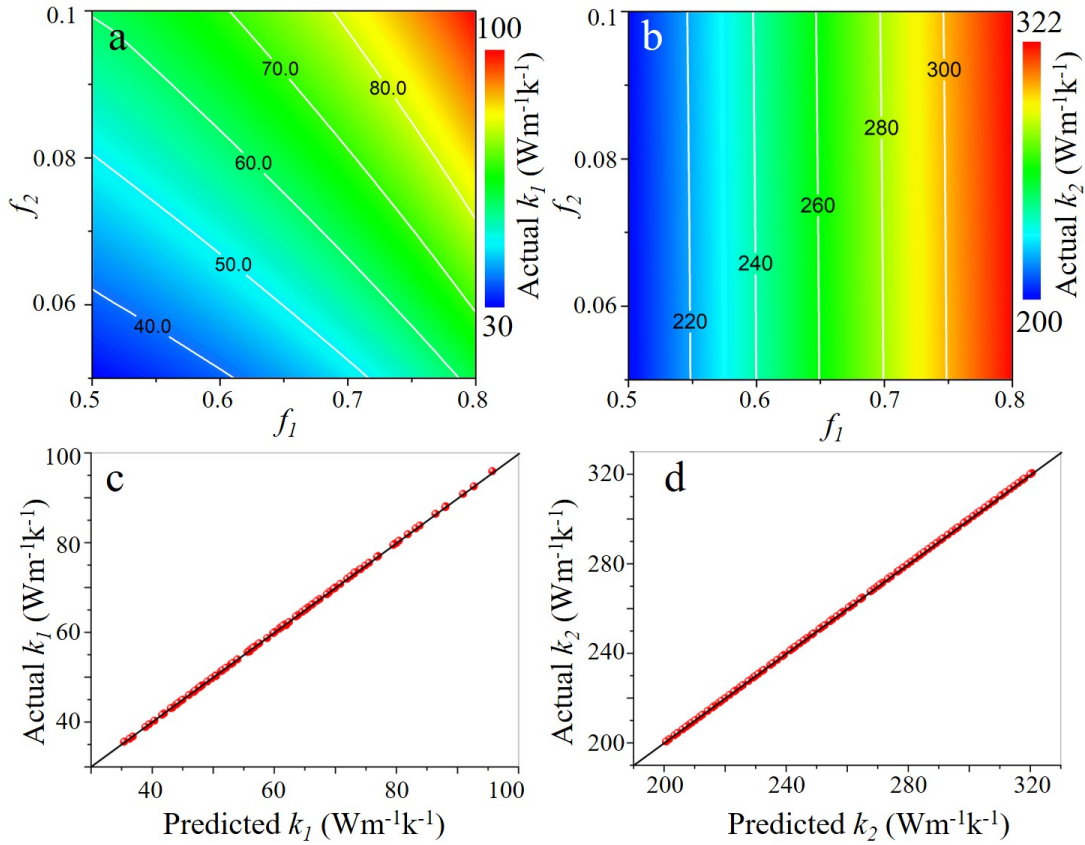


Figure III.4 – Panels (a) and (b) show the relation between design targets (heat conductivities k_1 and k_2) and design variables (geometrical parameters f_1 and f_2). The results are obtained basing on the chosen sample points and using two-scale homogenization theory. Panels (c) and (d) show good agreement between actual values and predicted values of the heat conductivities, demonstrating the reliability of the surrogate model. The indices k_1 and k_2 denote heat conductivity of the elementary cell in the x and y directions, respectively.

Error type	k_1	k_2
RMSE	$1.2 \cdot 10^{-3}$	$4.88 \cdot 10^{-5}$
Average	$6.45 \cdot 10^{-4}$	$3.52 \cdot 10^{-5}$
Maximum	$5.47 \cdot 10^{-3}$	$1.88 \cdot 10^{-4}$
R^2	0.9997	1

Table III.1 – Accuracy of the constructed surrogate model.

where α and β are weighting factors for the two objective sub-functions such that $\alpha + \beta = 1$. The function $E(k_1, k_2, \alpha, \beta)$ measures the overall difference between obtained and objective values. We define $\alpha = \beta = 0.5$, i.e. equal weights for the diagonal tensor elements k_1 and k_2 . The principle is to obtain a global min-

	Predicted	Targeted	Relative difference
$k_1(\text{Wm}^{-1}\text{K}^{-1})$	263.97	264	0.01%
$k_2(\text{Wm}^{-1}\text{K}^{-1})$	66.01	66	0.02%

Table III.2 – Comparison of predicted value and targeted value for the derived set of parameters.

imum within the discrete solution space. We solve this inverse problem by using a Non-Dominated Sorting Genetic Algorithm approach [Deb 02]. The one hundred random structures, corresponding to the parameter space samples obtained by the OLHS method, form the first generation. During the search process, the population size and the number of generations are defined as 12 and 200, respectively. New generations are created using crossover and mutation processes. We set the mutation distribution index and crossover distribution index as 20 and 10, respectively. The crossover probability is set as 0.9. For the sake of clarity, we do not detail the well-established genetic algorithm approach. In short, the Non-Dominated Sorting Genetic Algorithm performs well enough in our case and enables us to determine efficiently the desired design parameters.

Following this approach, we obtain the desired set of parameters as $f_1 = 0.6576$ and $f_2 = 0.0835$ for $C = 2$. We then implement the microstructure and calculate the corresponding heat conductivities. The result are listed in Table.III.2. It can be seen that the obtained parameters closely mimic the desired transformed medium.

III.2.4 Heat manipulation performances of the designed metadvice

We now turn to the theoretical recipe for realizing thermal harvesting based on optimized composite microstructures. Note that the heat conductivity in Eq. (III.8) is expressed in (r, θ) polar coordinates while the microstructure is designed in (x, y) Cartesian coordinates. To build a cylindrical thermal harvesting device, we discretize the shell region into numerous units and transplant microstructures with matched geometrical parameters into each unit. We design in this paper a discrete thermal harvesting device with 15 radial layers and 45 tangential sectors. Similarly to what has been done in Ref. [Pomot 20], we could have considered an increasing number of layers and sectors to very accurately approximate the idealized thermal concentrator parameters. However, we focus here on a practically implementable design. The materials constituting the microstructure are naturally available materials: copper (material A) and air (material B). It is understood that the device could be built from other materials. We use copper and air here considering their applicability for realistic experiments.

Numerical calculations were conducted, where temperatures at the left and right boundary are respectively imposed as 1 K and 0 K, for easiness in normalization. We apply Neumann (perfect insulator) conditions at other boundaries. As indicated in the scheme (Fig. III.5), iso-thermal lines are significantly compressed to the inner domain ($r \leq r_1$). Hence, heat flux density in the inner domain is enlarged, implying that more heat energy is concentrated into the central region. In addition, iso-thermal lines in the background are uniform with little perturbations. That is, the heat energy is harvested and concentrated into the central region without much perturbation of the external thermal field. We emphasize that similar computations would also hold for time-harmonic acoustic and electromagnetic equations. We further conduct a quantitative analysis of the thermal

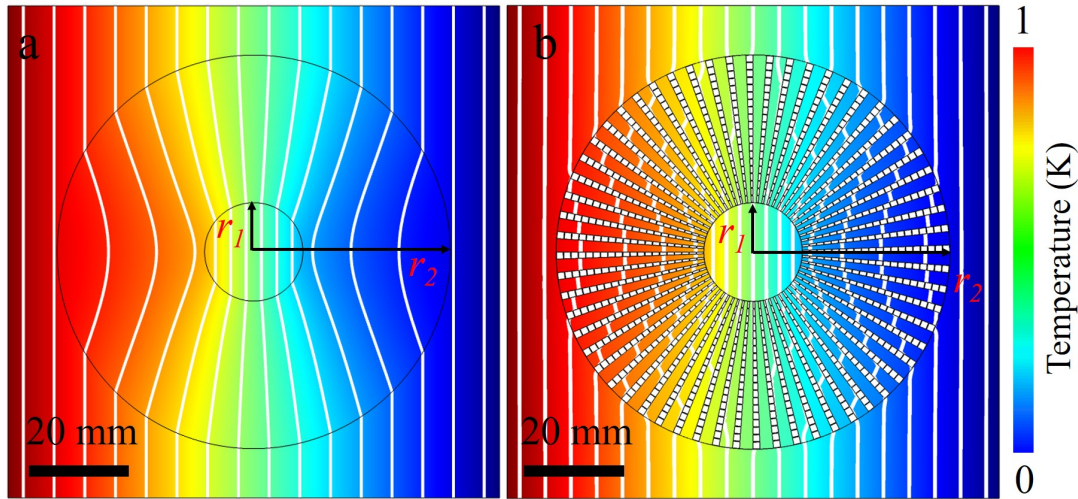


Figure III.5 – Temperature fields in the steady state for (a) the ideal case and (b) the proposed thermal harvesting device. In both cases, heat flows are concentrated to the inner domain without much perturbations to the external thermal field.

harvesting behavior of the proposed scheme. Two measurement lines are defined. An horizontal line ($y = 0$) is selected to reveal perturbations of the external thermal field whereas a vertical line ($x = r_2$) is chosen to illustrate the heat harvesting efficiency. We also build an additional contrast plate that occupies the same area as the harvesting device but that is composed only of a homogeneous background medium. The following index η_0 is defined to evaluate the energy harvesting efficiency as

$$\eta_0 = \left| \frac{T_{x=r_1} - T_{x=-r_1}}{T_{x=r_2} - T_{x=-r_2}} \right|. \quad (\text{III.17})$$

The index M_V is introduced again to characterize the perturbations to external fields (*i.e.* the thermal neutrality of the concentrator)

$$M_V = \frac{\int_{\Omega} |T(x, y, z) - T_r(x, y, z)| d\Omega}{\int_{\Omega} d\Omega}, \quad (\text{III.18})$$

where Ω denotes the probe domain of external thermal fields and T_r represents the temperature field of the homogeneous medium. The index M_V reveals all perturbations to the external heat profile.

It is apparent in Fig. III.6(a) that thermal energy is significantly concentrated into the inner domain, as a tight focusing with a local heat-intensity increase is observed. We list thermal gradients inside the inner domain (characterized by $\Delta T_{in} = |T_{x=r_1} - T_{x=-r_1}|$) and harvesting efficiencies for different cases in Tab. III.3. The results indicate that thermal gradients in the central region are almost twice as large as in the contrast plate. The concentration efficiency is significantly lifted. Both results reach nearly theoretical values, demonstrating that the heat concentrating scheme is both effective and accurate.

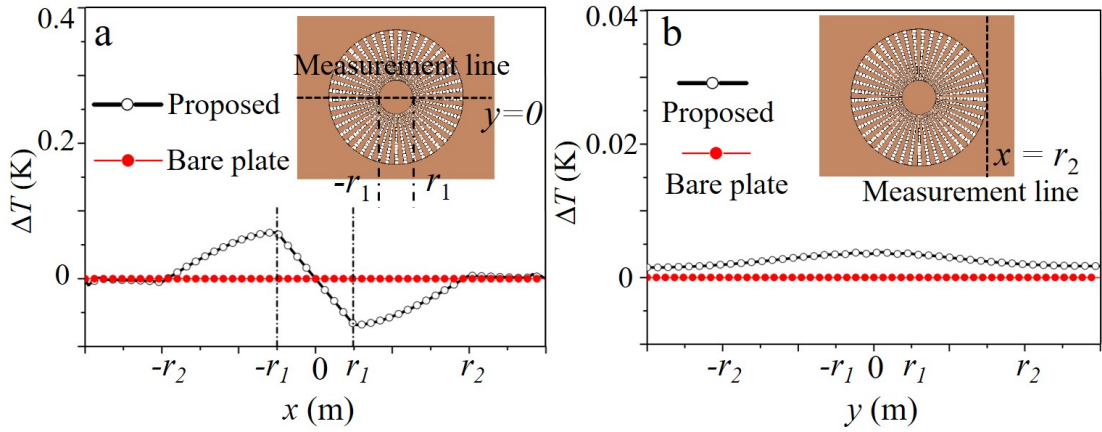


Figure III.6 – Comparison of temperature profiles between the harvesting device and the contrast plate along the measurement lines (a) $y = 0$ and (b) $x = r_2$. All results are obtained in the steady-state and the insets denote positions of measurement lines. We define $\Delta T = |T(x, y, z) - T_r(x, y, z)|$ to quantitatively demonstrate the heat harvesting performances. Significant heat-focusing in the inner domain ($-r_1 < x < r_1$) and minor fluctuations in external domain (along $x = r_2$) are both observed, demonstrating good heat concentrating performances.

It can be observed in Fig. III.6(b) that temperatures along the vertical measurement line are almost uniform, indicating that the external thermal field is only slightly influenced. We notice some minor perturbations in Tab. III.3 which are mainly due to the discretization process and to numerical errors.

Thus far, all that has been achieved for heat can be directly translated to airborne acoustics (with rigid inclusions) and electromagnetism (with perfectly conducting inclusions, in the case when the magnetic field is polarized perpendicular to the xy -plane), since governing equations are identical in the static limit,

Index	Ideal	Proposed	Bare plate
ΔT_{in} (K)	0.4	0.39	0.2
η_0	0.5	0.49	0.25
M_V (K)	0	0.0025	0.0003

Table III.3 – Thermal harvesting performances for different cases.

and so results in Fig. III.5 and Fig. III.6 hold for the acoustic and electromagnetic counterparts of the thermal concentrator. We would like to investigate now the diffusive nature of heat conduction. We define same boundary conditions as the steady state case and focus here on the evolution of thermal harvesting performance over time. Temperature distributions at different time steps t are shown in Fig. (III.7), where thermal gradients and perturbations are also plotted as a function of time. It is observed that perturbations of the external thermal profile increase and then decrease after a certain lapse of time, whereas the thermal gradient of the object increases gradually toward its maximum value. The distortions to external thermal field is mainly caused by ignoring heat capacity [Schittny 15]. Generally, the proposed design performs well for harvesting thermal energy, with significant heat flux concentrated in the inner domain and little perturbation to the outside thermal field, once the permanent regime has been reached. We stress that the design process proves feasible as the created device works efficiently and converges to almost the same harvesting performance as in the ideal case.

The heat concentration efficiency is directly determined by the constant C [Han 13], which in turn can be approached by the material properties and the geometry of the microstructures. To gain more insights into the underlying mechanism of the microstructure, we derive and show in Fig. III.8 the relation between design variables (area fraction f_1 and f_2) and the heat concentration efficiency. For comparison, we further assume two other materials C and D to substitute for material B, with heat conductivity $k_C < k_B < k_D$. It is observed that higher concentration efficiency requires larger f_1 and smaller f_2 which directly indicates larger geometrical anisotropy. Besides, we notice that smaller design variables are needed to achieve a given efficiency for a larger conductivity of the second material (for constant material A). Larger material anisotropy also allows for a larger maximum concentration efficiency.

Note that the microstructure we employed in Fig. III.2 is not the unique choice. One can use other elementary cells as long as they are appropriate to obtain the required anisotropy. To validate the wide-range application of our approach, we further present several other elementary cells and build corresponding devices. Steady state simulations are conducted with same boundaries with the aforementioned case. In Fig. III.9, we set material properties as design variables and recover the widely used solar-shaped device in literatures. In Fig. III.10, we obtain the same design as in Fig. III.1 but based on a different elementary cell obtained by a sub-lattice translation.

Besides, we show in Fig. III.11 a split ring element cell for which it seems unlikely that the effective medium theory could be easily applied. We observe that in all these cases, thermal gradient are elevated within the object domain $-r_1 < r < r_1$, revealing that heat fluxes are concentrated to this domain. Besides, the surrounding temperature profile are not influenced, showing that good harvesting performance is achieved without much perturbations to the external field. As a note, the symmetry of the split ring element cell is reduced compared to the other cases, but the effective tensor remains diagonal. The strength of our approach becomes apparent when dealing with such more complex geometries, where the application of effective medium theory is far from trivial.

We stress that using the optimization approach in this paper high-performance thermal-harvesting designs can be obtained that meet given external constraints, such as maximum or minimum values for material properties and geometrical parameters. We can search for the best solution among materials properties, microstructures and geometrical parameters within the full available range, providing a substantial flexibility and many degrees of freedom in practical applications.

Note that the impact of volumetric heat capacity is ignored, as steady-state is the more practical case and more widely studied, from the point of real applications [Guenneau 12, Han 13, Han 15b]. But they can also be considered as additional design targets in the optimization process. Besides, we considered in this paper two-dimensional (2D) harvesting devices as fabrication and measurement are presumably simpler than in 3D. The proposed optimization method, however, is also well suited to the design of 3D thermal harvesting devices. A major difference is that more design variables are required in 3D, and thus more computational resources would be required to undertake such a study, for which the theoretical part of the present work would apply *mutatis mutandis*.

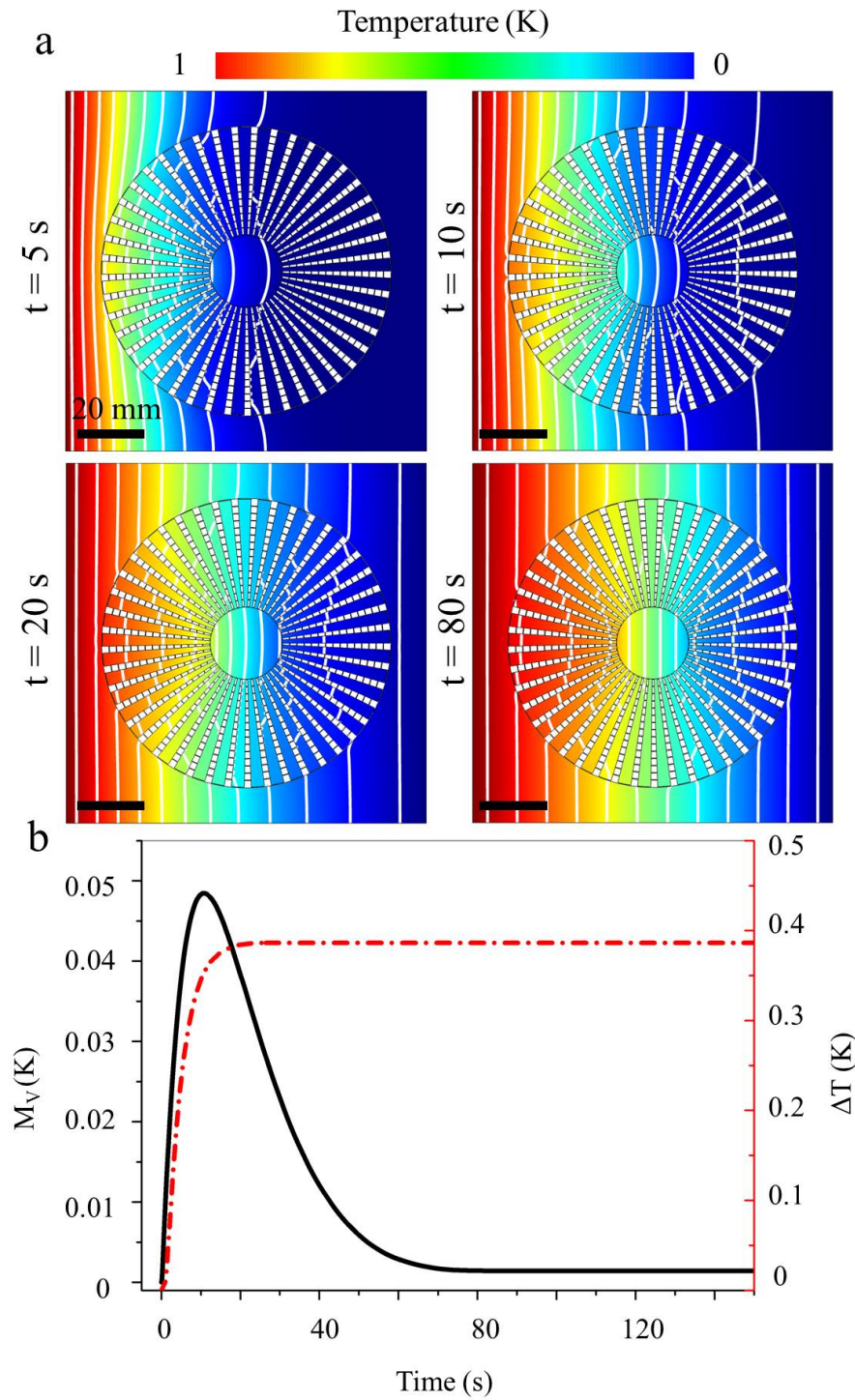


Figure III.7 – Thermal harvesting performances of the proposed device in the transient regime. (a) Temperature fields are illustrated at different times t . The performances get gradually better after a certain lapse of time. The scale bar denotes 20mm. (b) Thermal gradients of the inner domain ($\Delta T_{in} = |T_{x=r_1} - T_{x=-r_1}|$) and perturbations to external thermal field (M_V) are plotted as functions of time. The quantitative results agree well with those revealed in (a).

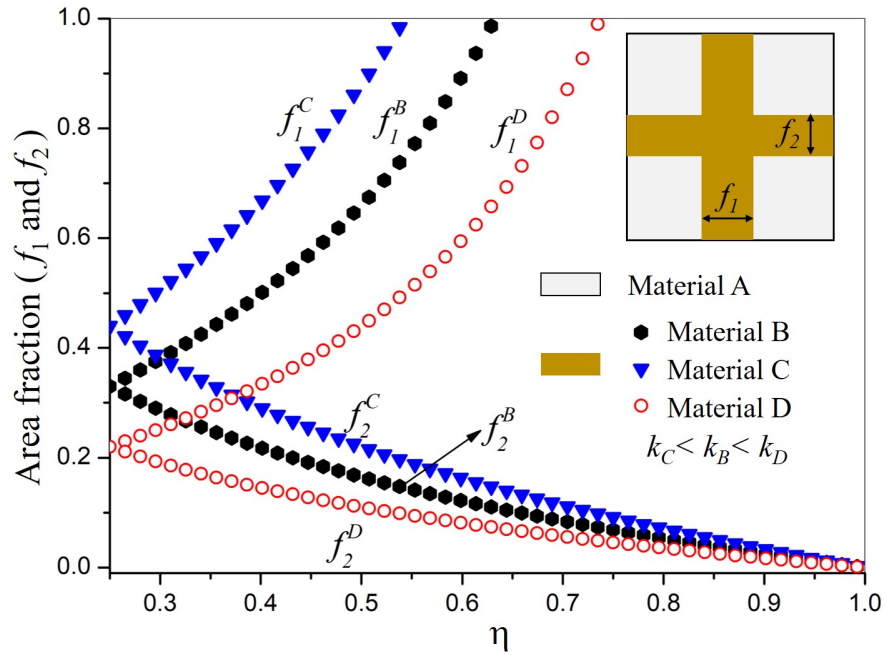


Figure III.8 – Relation between design variables (area fractions f_1 and f_2) and the concentration efficiency. The inset shows the studied elementary cell where one material is pre-defined as $k_A = 0$ and another material is varied. In addition to material B ($k_B = 400 \text{ Wm}^{-1}\text{K}^{-1}$), we also considered material C ($k_C = 300 \text{ Wm}^{-1}\text{K}^{-1}$) and material D ($k_D = 600 \text{ Wm}^{-1}\text{K}^{-1}$) for a comparison.

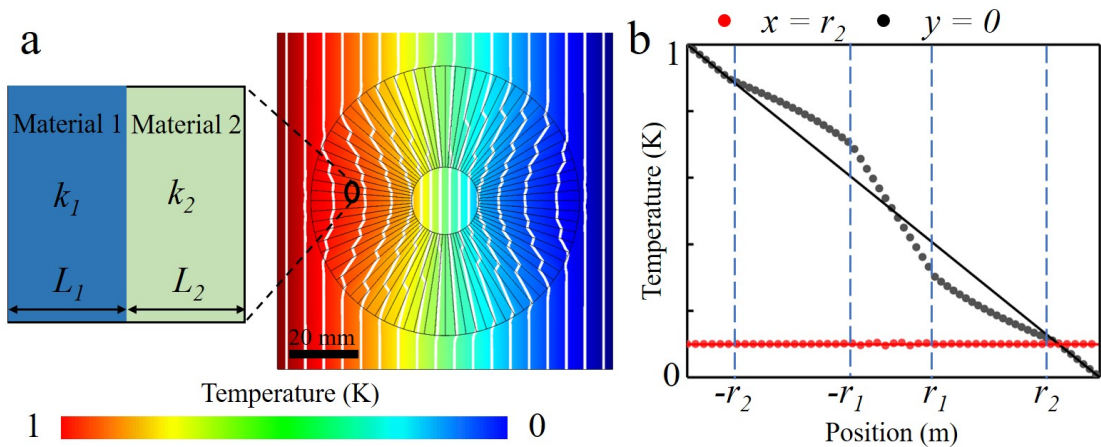


Figure III.9 – (a) Laminar structures defined by two material parameters (k_1 and k_2) if $L_1 = L_2$ and two additional geometrical parameters if $L_1 \neq L_2$. The optimized parameters are $k_1 = 0.26782$ and $k_2 = 3.7328$ if we impose $L_1 = L_2$. (b) Corresponding thermal harvesting performance.

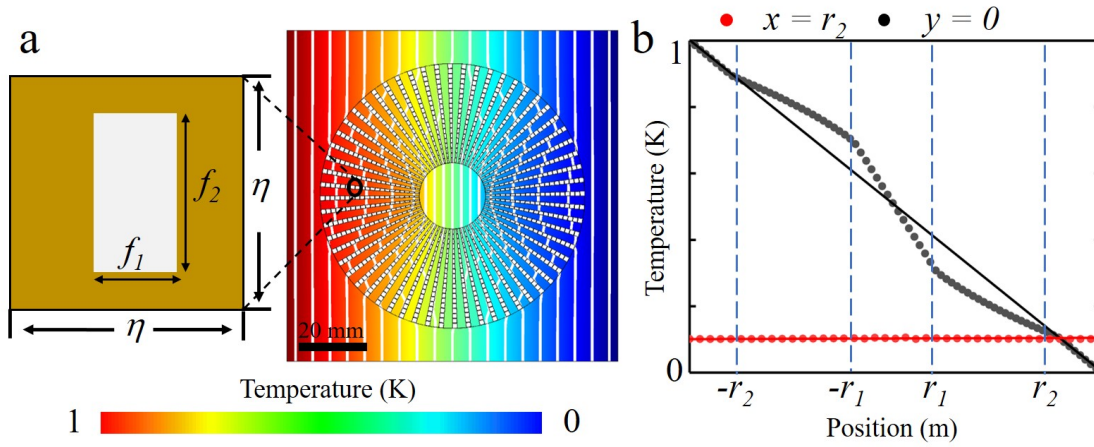


Figure III.10 – Additional optimized microstructures and corresponding thermal harvesting performance. (a) Elementary cell defined by two geometrical parameters $f_1 = 0.34238$, $f_2 = 0.91675$. The materials used are same with those in Fig. III.2. (b) Corresponding thermal harvesting performance. The scatters denote temperatures of the proposed device while the solid line are the temperatures from a bare plate. Following the proposed design process, we have dealt with different microstructures and obtained same thermal conductivities as $k'_r = 264 \text{ Wm}^{-1}\text{K}^{-1}$, $k'_\theta = 66 \text{ Wm}^{-1}\text{K}^{-1}$.

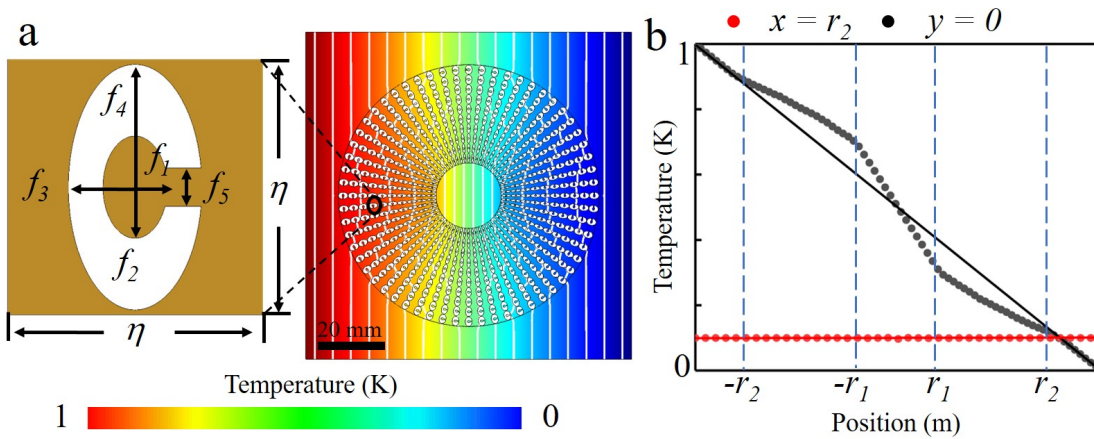


Figure III.11 – (a) Split ring structure defined by five geometrical parameters. The optimized parameters are $f_1 = 0.1037$, $f_2 = 0.1261$, $f_3 = 0.4799$, $f_4 = 0.2614$, and $f_5 = 0.0994$. (b) Corresponding thermal harvesting performance.

III.3 SAMPLE FABRICATION AND EXPERIMENTAL VALIDATION

We have fabricated and characterized the proposed thermal harvesting devices that mold the flow of heat around the object in a metal plate. To obtain the heat conductivity $k_b = 132 \text{ Wm}^{-1}\text{K}^{-1}$ in the background and central region, we design a composite structure by drilling holes into a copper plate. The corresponding (room temperature) bulk heat conductivities of the two materials are $k_A = 0.026 \text{ Wm}^{-1}\text{K}^{-1}$ and $k_B = 400 \text{ Wm}^{-1}\text{K}^{-1}$. The latter is larger than the former by more than 4 orders of magnitude, which facilitates the design. The effective heat conductivity can be achieved by two-scale homogenization theory or by Maxwell-Garnett theory as

$$k_e = k_s \left[1 + \frac{2(k_f - k_s) f}{k_f + k_s - (k_f - k_s) f} \right] \quad (\text{III.19})$$

where k_e is the effective heat conductivity, k_s and k_f are heat conductivities of the solid materials (copper here) and filling materials (air here). Following this approach, we built holes array (diameter 1.6 mm) in the background and central plate with equal space 2 mm.

For the fabrication of the proposed structure, we used the CNC machining technique to produce the pattern shown in Fig. III.12b,c. We design in the numerical analysis a discrete thermal harvesting device with 15 radial layers and 45 tangential sectors. However, such a structure can not be obtained due to accuracy limitations of the CNC machining technique. Hence, we rather fabricate a device with less refined discretization in both tangential and radial directions. As mentioned above, we could have considered an increasing number of layers and sectors to very accurately approximate the idealized thermal concentrator parameters, but here we focus on a practical design. Considering the trade-off between functionality and fabrication difficulty, we have made the samples shown in Fig III.12b,c.

To measure the temperature profiles via Planck thermal emission, we used a conventional infrared thermal camera (FLIR A6702sc) to capture thermal images. Considering that copper is highly reflective, we cover the sample surface with white paint which significantly reduces the surface reflectivity. Furthermore, we coat the sample with a thin layer of polydimethylsiloxane (PDMS) with thickness around $200 \mu\text{m}$. The PDMS layer is nearly "black" for the wavelengths detected by the infrared camera which facilitates the capture of thermal images. Besides, the PDMS layer serves as a heat insulator on the related boundaries. It can also reduce heat convection between the sample and the surroundings, which has considerable influence on the thermal images.

A photograph of the experiment setup is shown in Fig. III.12a, where local heating on the left side of the plate is realized by a tank filled with hot water and the right side is immersed in an identical tank with room-temperature water. The

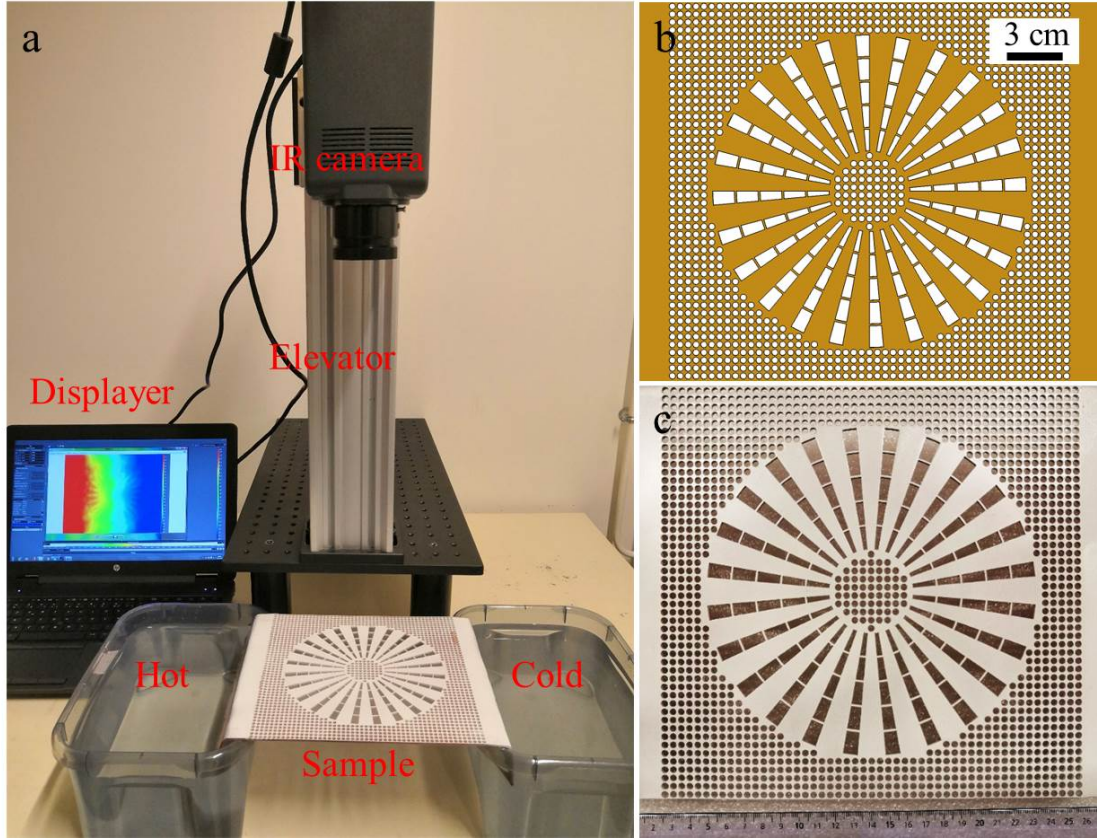


Figure III.12 – Fabricated samples and experimental setup. (a) Photograph of the experimental setup. (b) Blueprint of the designed thermal harvesting device. The red areas are bulk copper ($k_B = 400 \text{ Wm}^{-1}\text{K}^{-1}$) whereas the white regions denote air ($k_A = 0.026 \text{ Wm}^{-1}\text{K}^{-1}$). (c) Photograph of the sample made by CNC machining. White paint and thin PDMS layer are added on the sample to reduce surface reflectivity. The PDMS layer also acts as a heat insulating layer that reduces heat convection to the surroundings.

other sides are left free and are covered with a PDMS thin layer. An elevator is used to tailor the position of the infrared camera to capture images of the temperature profiles.

In Fig. III.13, we show the numerical and experimental results for the proposed device at various times t after exposing the plate to the heat baths at $t = 0$ s. We observe that the thermal harvesting device successfully fulfills its tasks in that heat fluxes are focused to the central region. The heat density are elevated compared to the surroundings. Furthermore, the temperature field outside of the device is almost not affected, as if nothing was there. Our experimental results agree with the corresponding numerical calculations (performed with COMSOL Multiphysics), validating the effectiveness of the design.

We note some differences between experimental and numerical results. When designing the samples, we made compromises between functionality and fabrication difficulty. This discretization process would be minimized by building a large

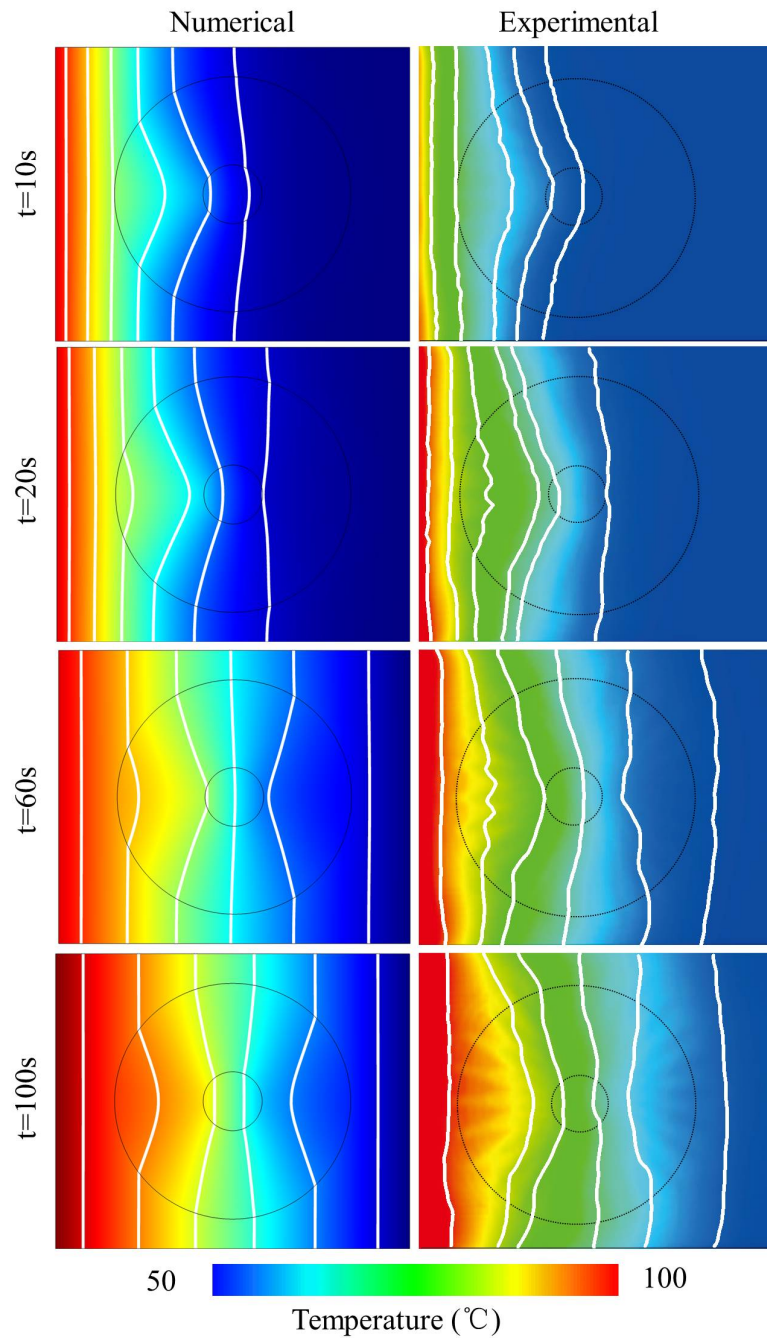


Figure III.13 – Measured temperature distributions at different times t as indicated. At $t = 0$ s we start from a homogeneous room temperature profile. Numerical results are shown in the left column, whereas experimental results are depicted in the right column. The white lines are isotherm lines.

enough number of layers and sectors. Besides, in the ideal case we did not account for heat conduction and thermal radiation to the surrounding air, which also con-

tribute to the remaining discrepancies. In addition, although some measures have been adopted to decrease heat convection, like coating the surface with a PDMS layer, the negative influence of heat convection is still not eliminated.

Generally, the fabricated structure accomplishes the two goals: concentrating heat fluxes to the central region and imposing no perturbations to the external temperature fields. To gain a better vision on the experimental results, we propose a model considering the above aspects though they not part of the device design. The temperature profiles in the steady state are studied, as shown in Fig. III.14. In the numerical simulations, we define surface emissivity as 0.9 and natural convection coefficient $20 \text{ Wm}^{-2}\text{K}$. The hot end and the cold end, in agreement with experiments, are defined as 373 K and 323 K, respectively. Compared with the bare plate (Fig. III.14a), the simulation results in Fig. III.14c clearly show thermal concentrating performances that, however, not as good as the ideal case shown in Fig. III.14b, due to thermal convection and emission effects. We observe that the experimental results (Fig. III.14d) agree better with the numerical simulations in Fig. III.14c, demonstrating that the abovementioned aspects are the main factors contributing to the differences between experimental and simulation results. Here a relatively larger convection coefficient is employed as we are considering not a pure plate but a surface with many holes that contributes to more thermal convection. In addition, we show that by using larger convection coefficients, the simulation results agree better with the experiments, illustrating that it is an effective influencing aspect.

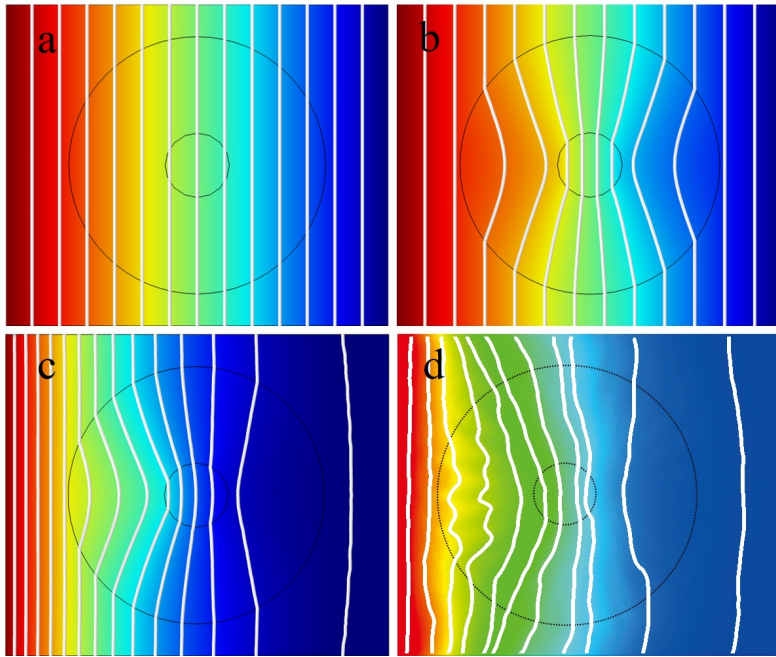


Figure III.14 – Temperature distributions in the steady state for (a) a bare plate; (b) transformed parameters without considering thermal convection and emission; (c) transformed parameters considering thermal convection and emission; (d) experiments.

III.4 SUMMARY

We proposed a general method to design thermal-energy harvesting devices from naturally available materials. We designed composite microstructures and calculated their effective conductivity by the two-scale homogenization technique. We then implemented the Optimal Latin hypercube method to obtain design parameters that can best mimic the transformed medium. We built a harvesting device model based on the obtained optimized microstructures. A sample is fabricated with copper and PDMS. Experiments are conducted subsequently. Both numerical and experimental results demonstrate good thermal harvesting performance, thereby validating the effectiveness of the design method.

The optimization method adds great flexibility to the constraints that can be imposed on devices, which allows one to find the best possible solutions with different geometrical structures and component materials. We stress that the flexibility and simplicity of the method is a good addition to existing heat manipulation techniques, including other thermal functionalities, *i.e.* cloaking and illusion. It also paves a path for novel optical, acoustic and electromagnetic devices based on form-invariant governing equations.

Chapter IV

Thermal metasurface for selective emission and heat radiation control

IV.1	Introduction	52
IV.2	Selective emission based on layered medium	52
	IV.2.1 Principle of thermal emission control	52
	IV.2.2 Surface emissivity calculation based on transfer matrix method	53
IV.3	Theoretical realization of Infrared camouflage and other functionalities	56
IV.4	Summary	61

IV.1 INTRODUCTION

In this chapter, we propose a simple strategy to realize thermal camouflage based on infrared-transparent thin films thickness engineering. Using this simple approach, we demonstrate spatial tunability and continuity in thermal emission. By locally changing the thickness of the coating film, we obtain a continuous change of emissive power and consequently implement the desired thermal functionalities. This technique of thermal radiation manipulation has the following advantages: 1) In theory, perfect camouflage can be achieved since the required continuously changing thermal radiation can be realized by a calculated thickness distribution that is also continuous, without further discretization and approximation. 2) The same surface emissivity can be obtained with coating films of different thickness, allowing for size flexibility in fabrication. 3) Structural simplicity follows from the fact that only bilayer films are employed.

IV.2 SELECTIVE EMISSION BASED ON LAYERED MEDIUM

IV.2.1 Principle of thermal emission control

When observed by an infrared camera, an object is detected as it has different thermal radiation power with its surroundings. According to the working principle of an infrared camera, the observed temperature of an object is based on the detected radiation from the target surface, which includes mainly three parts, i.e., object radiation P_o , surroundings reflection P_r and air radiation P_a , expressed respectively as

$$P_r = R_\lambda P_{b\lambda}(T_a), P_o = \epsilon_o P_{b\lambda}(T_o), P_a = \epsilon_a P_{b\lambda}(T_a) \quad (\text{IV.1})$$

where R_λ and ϵ_o are surface reflectivity and emissivity of the object, ϵ_a is the emissivity of the surrounding air, T_a and T_o are temperatures of the surrounding air and the object, $P_{b\lambda}$ is the radiation of a blackbody. The detected thermal radiation can be expressed as

$$E_\lambda = A_o d^{-2} [\tau_{a\lambda}(P_r + P_o) + P_a], \quad (\text{IV.2})$$

where A_o is the viewing area of the object, d is the distance between the infrared camera and the object, $\tau_{a\lambda}$ is the spectral transmittance of the air. The infrared camera transfers the detected radiation into corresponding signal voltage as $V_S = A_R \int_{\Delta\lambda} E_\lambda \phi_\lambda d\lambda$, where A_R is the lens area of the infrared camera and ϕ_λ is the spectral response function [Song 20].

Understanding the working principle of an infrared camera, we realize that the key to achieving selective emission and obtaining related functionalities lies on tailoring the detected thermal radiation. Following Eq. IV.2, we easily find that we can tune the detected thermal radiation by controlling the object temperature T_o or

by controlling the surface emissivity ϵ_o . Comparably, regulating the temperatures of an object to match with its surroundings is far from easy and often needs external energy consumption. Some researches reports on thermal camouflaging through transformation thermodynamics, but with complicated structures difficult to fabricate [Li 18b]. Here we realize selective thermal radiation through tuning surface emissivity by engineering the thickness of an optical thin-film.

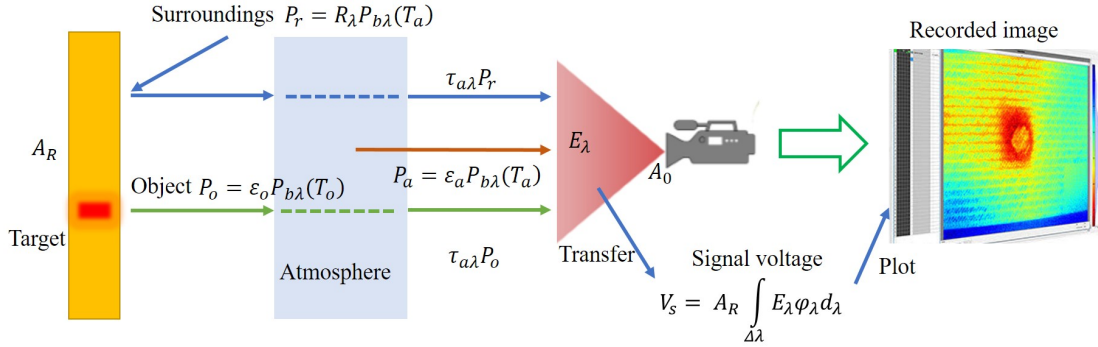


Figure IV.1 – Illustration of the working principle of an infrared camera: capture thermal radiation of an object and transfer the detected radiation to signal voltage, and further plot contour images.

IV.2.2 Surface emissivity calculation based on transfer matrix method

Our design is based on multilayered structures whose the optical properties are analytically obtained using the transfer matrix method depicted in Fig. IV.2. We consider three arbitrary layers and two interfaces. The tangential electric field at any position within the layer, is a superposition of two plane waves traversing the medium at opposite directions with

$$\begin{cases} E_{j-1,j} = E_{tj} + E_{sj} \\ \eta_0 H_{j-1,j} = (E_{tj} - E_{sj}) n_j \end{cases}, \quad (IV.3)$$

at the first interface and

$$\begin{cases} E_{j,j+1} = E_{ij} + E_{rj} \\ \eta_0 H_{j,j+1} = (E_{ij} - E_{rj}) n_j \end{cases}, \quad (IV.4)$$

at the second interface, respectively. Considering that

$$\begin{cases} E_{ij} = E_{tj} e^{-i\delta_j} \\ E_{sj} = E_{rj} e^{-i\delta_j} \end{cases}, \quad (IV.5)$$

we relate the field amplitudes on two sides by

$$\begin{pmatrix} E_{j-1,j} \\ \eta_0 H_{j-1,j} \end{pmatrix} = \begin{pmatrix} \cos \delta_j & \frac{i}{n_j} \sin \delta_j \\ in_j \sin \delta_j & \cos \delta_j \end{pmatrix} \begin{pmatrix} E_{j,j+1} \\ \eta_0 H_{j,j+1} \end{pmatrix}. \quad (IV.6)$$

The transmission matrix of the j -th layer can be thus obtained as

$$M_j = \begin{bmatrix} \cos \delta_j & \frac{i}{n_j} \sin \delta_j \\ in_j \sin \delta_j & \cos \delta_j \end{bmatrix}, \quad (\text{IV.7})$$

and the transfer matrix for the whole multilayer film structure, consisting of N layer read as

$$M = \begin{pmatrix} m_{11} & m_{12} \\ m_{21} & m_{22} \end{pmatrix} = \prod_{j=1}^N M_j, \quad (\text{IV.8})$$

where $n_j = n'_j + in''_j$ and $\delta_j = 2\pi\lambda^{-1}n_j d_j \cos \alpha_j$ is the effective phase shift thickness of the j -th layer, with d_j the geometrical thickness and n_j the refractive index. The reflectivity R_λ and transmittivity T_λ of the multilayer film read as

$$R_\lambda = |r_\lambda|^2 = \left| \frac{m_{21}}{m_{11}} \right|^2, T_\lambda = |\tau_\lambda|^2 = \left| \frac{m_{22}}{m_{11}} \right|^2. \quad (\text{IV.9})$$

Kirchhoff's law states that the emissivity of an object in thermal equilibrium is equal to its absorptivity, i.e.,

$$\epsilon_{\text{obj}}(\lambda) = A_\lambda = 1 - R_\lambda - T_\lambda. \quad (\text{IV.10})$$

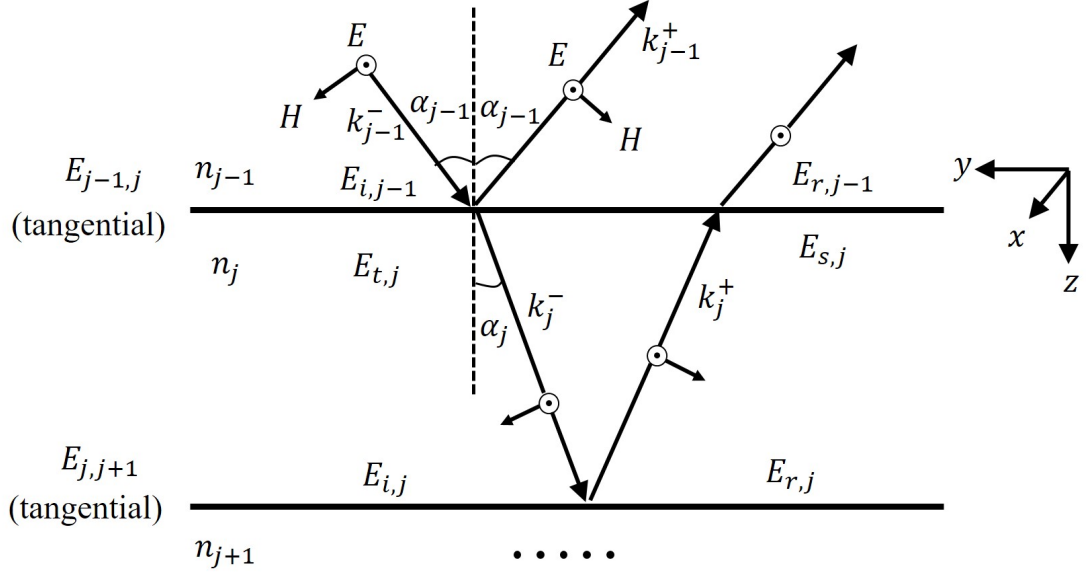


Figure IV.2 – Notation of electric field amplitudes within an arbitrary multilayer. The subscripts indicate the medium, the signs + and – distinguish between incident and reflected waves, respectively.

Using Planck's law, the thermal radiance of an object in the atmosphere window is given by

$$P_{\text{obj}}(T) = \int_{\lambda_1}^{\lambda_2} I_{\text{obj}}(\lambda, T) d\lambda = \int_{\lambda_1}^{\lambda_2} \epsilon_{\text{obj}}(\lambda) I_{\text{BB}}(\lambda, T) d\lambda, \quad (\text{IV.11})$$

where $I_{\text{obj}}(\lambda, T)$ is the spectral radiance of the object, $I_{\text{BB}}(\lambda, T) = 2hc^2\lambda^{-5}(e^{(h_Pc/(\lambda k_B T))} - 1)^{-1}$ is the spectral radiance of a blackbody at temperature T , h_P is Planck's constant, k_B is the Boltzmann constant, c is the vacuum speed of light, λ is the wavelength, $\epsilon_{\text{obj}}(\lambda)$ is the spectral emissivity and $[\lambda_1, \lambda_2]$ is the spectral range of the infrared camera.

Eq. IV.11 demonstrates that the perceived radiation by an IR camera can be effectively tuned by engineering the emissivity of the metasurface. Note that the operating wavelength range is often $3 - 5 \mu\text{m}$ or $8 - 14 \mu\text{m}$. Outside those two windows, infrared radiation is mostly attenuated by the surrounding air.

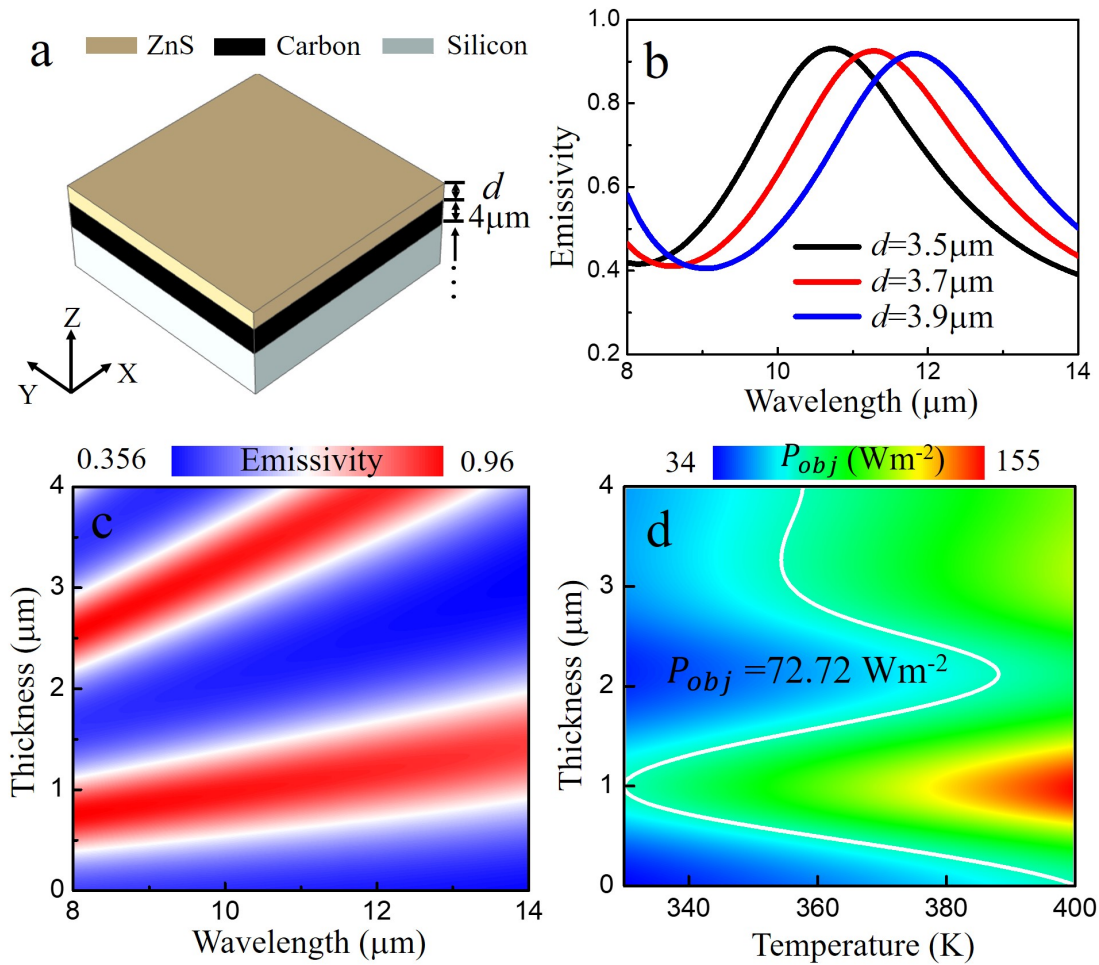


Figure IV.3 – (a) Schematic of the bilayer film deposited on a substrate (silicon). (b) Spectral emissivity as a function of wavelength. (c) Dependence of surface emissivity on film thickness and wavelength, obtained from Eq. (IV.10). (d) Integrated radiation power as a function of film thickness and temperature, obtained from Eq. (IV.11). The white iso-contour line depicts the radiation power of $P_{\text{obj}}(T) = 72.72 \text{ Wm}^{-2}$.

A thermal IR camera integrates the received energy over its operational wavelength and transfers the integration values to recorded temperatures in thermal images, which can be expressed by

$$T_r = C P_{\text{obj}}(T) = C \int_{\lambda_1}^{\lambda_2} \epsilon_{\text{obj}}(\lambda) I_{\text{BB}}(\lambda, T) d\lambda, \quad (\text{IV.12})$$

where C is a constant related to the lens area and spectral responsivity of a thermal camera [Qu 18]. Clearly, the detected radiation temperature T_r of an object (not a black-body) recorded in infrared images is not equal to its real temperature T . T_r is directly related to $P_{\text{obj}}(T)$ which is dependent on both the emissivity ϵ_{obj} (tuned by the film thickness d in this work) and the real temperature T . To achieve perfect thermal camouflage, the recorded temperature T_r (or $P_{\text{obj}}(T)$) should be spatially constant. Considering that each surface unit has a different temperature, we tune the spectral emissivity of each unit to make T_r (or $P_{\text{obj}}(T)$) the same over the whole sample by depositing over each unit a thin film of the corresponding thickness. We emphasize that the proposed strategy also applies to thermal radiation illusion or coding.

IV.3 THEORETICAL REALIZATION OF INFRARED CAMOUFLAGE AND OTHER FUNCTIONALITIES

We now proceed to realize thermal radiation modulation by engineering optical properties of the surface. For clarity, the design process for the general case is outlined through a specific example. Let us focus on the integrated radiation power $P_{\text{obj}}(T)$ in the operating wavelength range $8 - 14 \mu\text{m}$ that is directly related to the observed temperatures in the infrared images of the IR camera. We choose carbon as the ground layer with a thickness of $4 \mu\text{m}$, leading to zero transmission ($T_\lambda = 0$). Silicon is chosen as a substrate. Then, we use a dielectric layer made of zinc sulfide (ZnS) as a transparent material within the range of wavelengths $8 - 14 \mu\text{m}$ [Debenham 84, Lee 19] (see Fig. IV.3(a)). On the basis of energy balance, we calculate the emissivity from Eq. (IV.10). Spectral emissivity for various film thicknesses is shown in Fig. IV.3(b,c). With an increment of film thickness from $3.5 \mu\text{m}$ to $3.9 \mu\text{m}$, the emissivity peak shifts from 0.93 at $10.7 \mu\text{m}$ to 0.92 at $11.8 \mu\text{m}$. Here the emissivity range $[0.356, 0.96]$ is obtained, which can not be broadened, and can only be changed by choosing other materials. We note by passing that ZnS is not the only choice. Other transparent materials may also be good alternations, but in condition that the multilayered medium can offer broad tailorable emissivity ranges.

The emissivity as a function of thickness of ZnS and wavelength is depicted in Fig. IV.3(c). It can be seen that one can control the emissivity by engineering the thickness of ZnS. Using Eq. (IV.11), the radiated power is calculated as a function of ZnS thickness and temperature (see Fig. IV.3(d)). For example, the integrated power $P_{\text{obj}}(T) = 72.72 \text{ Wm}^{-2}$ is shown by a white iso-contour line in Fig. IV.3(d).

Objects having temperatures spanning the range 330 – 400K would be effectively detected to have the same emissive power if their surfaces were deposited with a dielectric layer whose thickness is determined by corresponding white iso-contour line.

In the following, we design thermal camouflage based on our multilayered media approach. Figure IV.4(a) shows a continuous temperature distribution generated by a heat spot located at the center of the silicon substrate (thermal conductivity $k_s = 1.3 \text{ W}^{-1}\text{m}^{-1}\text{K}^{-1}$). The side length of the simulated plate is 100 mm and the radius of the heat source is 2 mm. The surface is in contact with air with natural convection coefficient $2 \text{ W}^{-1}\text{m}^{-2}\text{K}^{-1}$ at temperature 340 K. As an example, we outline the camouflage of surface points along the center line of the plate. Figure IV.4(b) shows the integrated radiation power at three typical points along the center line (namely A, B and C), where it is observed that higher temperatures result in larger radiation powers, in general. The first step is to select a desired radiation power P_{obj} that all points can achieve with a selected film thickness. The possible range of the integrated radiation power is outlined in grey area. The camouflaged temperatures range from 340 K to 380 K (see Fig. IV.4b). We select the thickness profile shown in Fig. IV.4c for $P_{\text{obj}} = 72.72 \text{ Wm}^{-2}$.

The observed uniform camera temperature is shown in Fig. IV.4(b) with black line for the designed film with inhomogeneous thickness. The camera temperature field is obtained using Eq. (IV.12), where C is obtained using blackbody radiation. Therefore, the heat spot located at the center is hidden for an IR camera. This illustrating case demonstrates the thermal camouflage functionality by selective emission and thickness engineering.

It is noted that there is not only one possible thickness distribution that can realize such camouflage effects. We marked in Fig. IV.4(b) two groups of potential film thickness that can achieve same intergrated radiation power. This size flexibility will add much convenience to practical applications.

Based on the approach above, we can further engineer the whole surface emissivity (thickness) to realize thermal functionalities such as camouflage, illusion, and coding (Fig. IV.5).

In Fig. IV.5(a1-a3), we illustrate thermal camouflage. The required layer thickness is smallest at the central position and increases from the center outward (see Fig. IV.5(a2)). We observe that the camera temperature field is uniform ($T_r = 319.8\text{K}$) after film deposition, and thus the heat spot in the background plate is invisible to the detector, demonstrating perfect camouflage functionality (see Fig. IV.5(a3)).

By tailoring the distribution of the thickness of the coating film, we further obtain the thermal coding functionality in Fig. IV.5(b1-b3). Instead of making an object invisible, here we aim at make some desgined thermal messages appear from the "nothing" state. In an uniform thermal field (Fig. IV.5(b1)) (360 K), we leave out a subarea "HI" and deposit a coating layer of thickness $0.5 \mu\text{m}$ everywhere else (see Fig. IV.5(b2)). As a result, the heat signature "HI" (camera temperature 360 K) emerges from the background thermal field (camera temperature 319.8 K depicted in Fig. IV.5(b3)). We determine coating layer thicknesses using

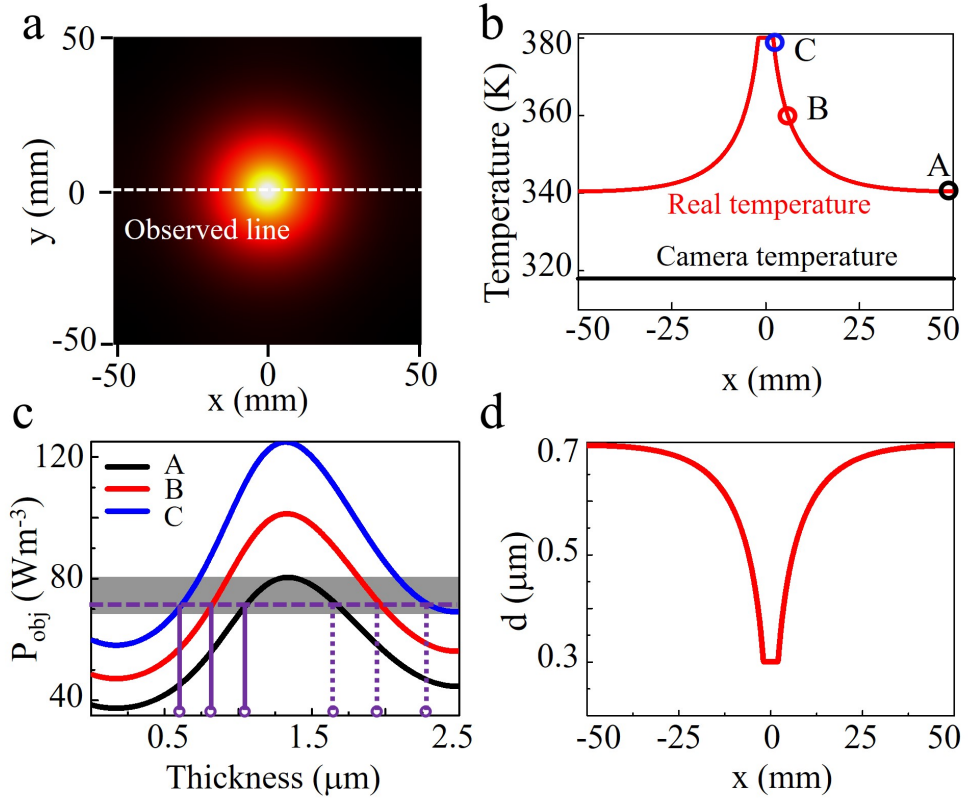


Figure IV.4 – Outline of the process to realize thermal camouflage. (a) A continuous temperature distribution generated by a heat spot located at the center of the silicon substrate. We aim to make the detected temperatures uniform along the white center line. (b) Original temperature distribution (red line) and pseudo camera temperature (black line) observed along the center line. (b) Integrated radiation power at three typical points along the center line versus film thickness. The grey region outlines the available integrated radiation power range that is accessible to camouflage by thickness engineering. The dashed line is for $P_{\text{obj}}(T) = 72.72 \text{ Wm}^{-2}$. (d) Film thickness distribution required to obtain the apparent uniform temperature in panel b, plotted along the center line.

the radiation power of $P_{\text{obj}} = 72.72 \text{ Wm}^{-2}$. We finally demonstrate the thermal illusion functionality in Fig. IV.5(c1-c3), where the heat signature "NO" is observed instead of the original message "YES" to confuse observers. This illusion functionality is also realized by properly engineering the film thickness. The surface is divided into three sub-regions: "YES", "NO", and background (Fig. IV.5(c2)). We deposit the sub-regions "YES" and background with film thicknesses $0.3 \mu\text{m}$ and $0.5 \mu\text{m}$, respectively, whereas sub-region "NO" remains uncoated. After deposition, the sign "NO" will be observed in the camera image instead of the original sign "YES" (Fig. IV.5(c3)). The thermal illusion functionality works like a combination of thermal camouflage and thermal coding, where real thermal messages are rendered invisible while misleading messages are observed instead. We empha-

size that more functionalities can be obtained through the proposed flexible film thickness engineering strategy. In applications, the spatially-distributed thickness can be realized by micro- or nano-fabrication like plasma deposition.

In our design, a very important aspect is the huge scale difference between variations of physical quantities (such as the temperature) inside the layer thickness and in the lateral directions. Whereas, the layer thickness is of the order of a few microns, the thermal gradient and thus the thermal distribution only change significantly over very large lateral distances. Considering a meter-size object and a temperature difference between the two sides of $\Delta T = 100$ K, then at the scale of a typical infrared (IR) wavelength of $10 \mu\text{m}$, the temperature change is only about 10^{-3} K. At that scale, the temperature variation can be considered continuous and the local change in thickness will not lead to any significant lateral scattering. Based on this reasoning, in the coding and illusion devices depicted in Fig. IV.5(b1-b3) and Fig. IV.5(c1-c3), the apparent discontinuities in the thickness and temperature can be made continuous to avoid scattering from the edges. Here we have ignored this aspect in the plots as the discontinuities can be smoothed out easily.

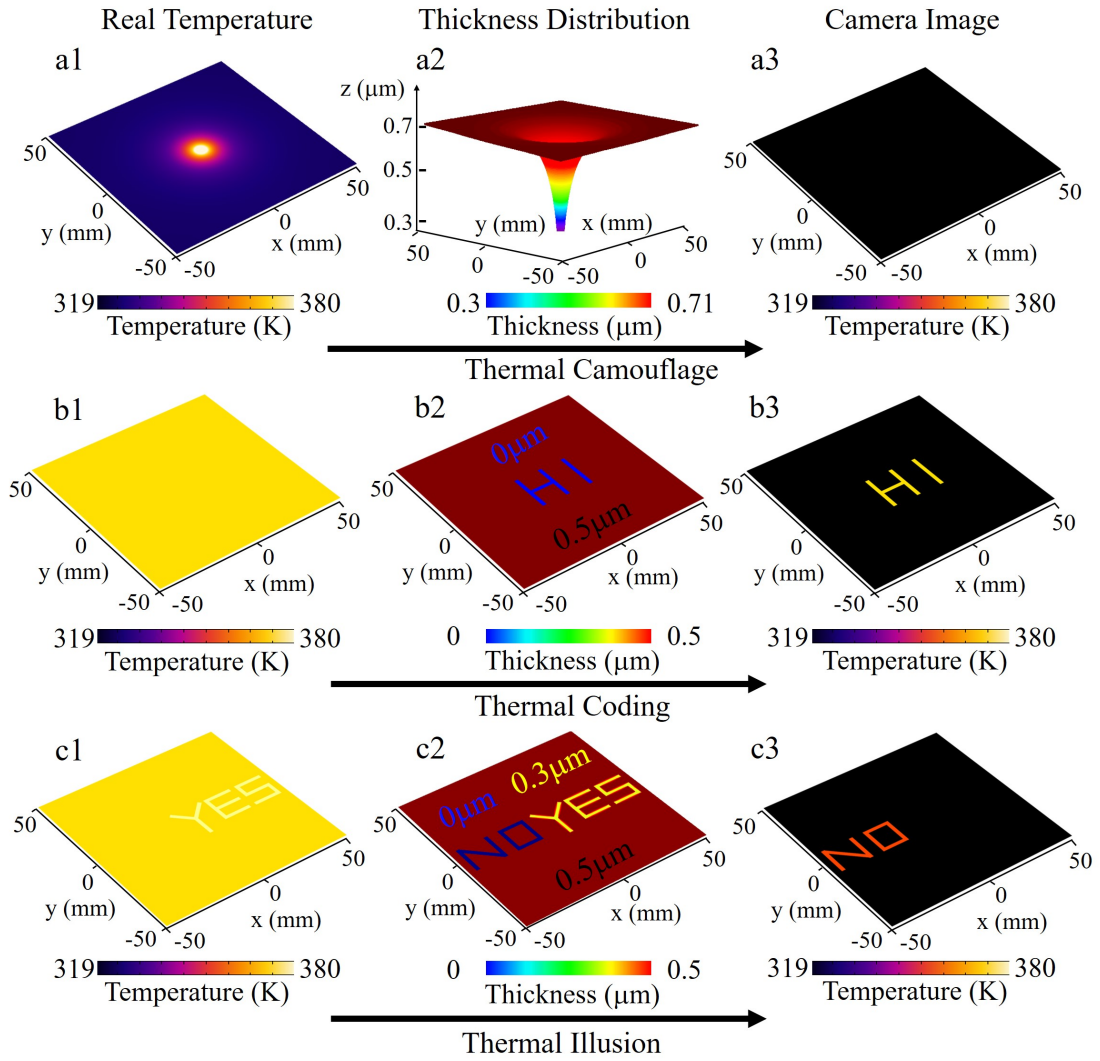


Figure IV.5 – Demonstration of different thermal functionalities. Thermal camouflage: a heat source in the background plate (see panel a1) is hidden to the IR camera (see panel a3) after thickness engineering (see panel a2). Pseudo camera temperature is $T_r = 319.8$ K. Thermal coding: For an uniform temperature field (see panel b1), the message "HI" is observed by the IR camera instead (see panel b3). The sub-area "HI" is unchanged while the remaining area is coated with a film of thickness $0.5 \mu\text{m}$ (see panel b2). Camera temperatures of the subarea "HI" and the remaining area are $T_r = 360$ K and $T_r = 319.8$ K, respectively. Thermal illusion: An original thermal image "YES" (see panel c1) is recorded as a different image "NO" in the IR camera (see panel c3). Original temperatures of the sub-area "YES" and other regions are 380 K and 360 K, while after thickness engineering camera temperatures in the sub-area "NO" and other area are 360 K and 319.8 K, respectively. For all cases, the selected radiation power is $P_{\text{obj}} = 72.72 \text{ Wm}^{-2}$.

IV.4 SUMMARY

In conclusion, a multilayer film based selective emission strategy was proposed and investigated for applications in infrared camouflage, thermal coding and thermal illusion. Through thickness engineering, the emissivity can be tuned continuously over a large range. The technique features advantages of a simple structure, easy fabrication and size flexibility. Our work provides an alternative solution to infrared stealth and other thermal radiation management technology based on selective emission.

Chapter V

Thermal metamaterials based on thermally driven deformation

V.1	Introduction	64
V.2	Concept design and samples fabrication	64
	V.2.1 Working mechanism of the bilayer beams.....	64
	V.2.2 Design of thermally driven smart metamaterials.....	66
	V.2.3 Fabrication technique	68
	V.2.4 Sample fabrication.....	72
V.3	Thermally driven motions	76
	V.3.1 Concept validation.....	76
	V.3.2 Quantitative analysis on thermally driven motions.....	78
	V.3.3 Parameter analysis for further optimization.....	80
V.4	Thermo-mechanical performances	81
V.5	Summary	82

V.1 INTRODUCTION

In this chapter, we design thermally actuated elements that provide fundamental mechanical motions (rotation and translation) at the microscale, which are crucial deformations highly required by a microrobot performing in a controlled manner. Then we fabricate functional stacks combining the proposed elements. The fabrication of such complex bimaterial samples is realized using a single material system but locally varying laser exposure. The stacks produce accurate movement under an applied thermal stimulus and totally recover to the rest state when the external stimulus is switched off. The system supports accurate motional amplitudes, reversible response, and is well controlled by a simple thermo-mechanical process (thermal expansion) in a dry environment. We demonstrate the possibility of building a three-axis microrobot with a single material using single-step lithography and thus bring thermoelastic metamaterials for microrobots closer to real applications. Our proposed design is a highly promising basis paving the way for the next micro-nanorobotic generation.

V.2 CONCEPT DESIGN AND SAMPLES FABRICATION

V.2.1 Working mechanism of the bilayer beams

Our thermally actuated structures are based on bilayer beams, utilizing the different thermal and mechanical properties of two different layers. As shown in Fig. V.1, the bilayer beam length becomes longer (or shorter) under temperature elevation (or decrement). Upon a temperature change dT , the original length changes from L_0 to $L_1 = L_0(1 + \alpha_1 dT)$ and $L_2 = L_0(1 + \alpha_2 dT)$ for the two layers, respectively, when exposed to unbounded state. Note that we consider the small thermal deformation in the linear stage. In the case that $\alpha_2 > \alpha_1$, a length difference is thus generated with a magnitude $L_0(\alpha_2 - \alpha_1)dT$. In the presence of perfect bonding of the two layers, this length gap is bridged by prescribing internal forces of opposing directions. Arising from the moment imbalance due to prescribed axial load through the cross sectional centroids of each layer, equilibrium of moment is maintained by prescribing the internal moments of both layers. This will give rise to the curvature depicted in Fig. V.1 [Lim 19].

The absence of external forces requires the axial forces acting on the two layers to be of opposing directions but equal magnitude $\sigma_1 h_1 = \sigma_2 h_2$ with the stress $\sigma_1 = E_1 \epsilon_1$ and $\sigma_2 = E_2 \epsilon_2$, where E_1, E_2 are Young's moduli and the strains are obtained by $\epsilon_1 = dL_1/L_1$ and $\epsilon_2 = dL_2/L_2$. Assuming equal layer thickness $h_1 = h_2$, the force equilibrium becomes

$$\frac{E_1 dL_1 h_1}{L_0(1 + \alpha_1 dT)} = \frac{E_2 dL_2 h_2}{L_0(1 + \alpha_2 dT)}. \quad (\text{V.1})$$

The length gap $L_0(\alpha_2 - \alpha_1)dT$ diminishes via shortening layer 1 and lengthening layer 2 by magnitude of dL_1 and dL_2 , respectively, i.e.

$$dL_1 + dL_2 = L_0(\alpha_2 - \alpha_1)dT. \quad (\text{V.2})$$

Combining Eq. V.1 and V.2, we obtain

$$dL_1 = \frac{L_0(\alpha_2 - \alpha_1)dT}{1 + \frac{E_1}{E_2} \frac{1+\alpha_2 dT}{1+\alpha_1 dT}}, dL_2 = \frac{L_0(\alpha_2 - \alpha_1)dT}{1 + \frac{E_2}{E_1} \frac{1+\alpha_1 dT}{1+\alpha_2 dT}}, \quad (\text{V.3})$$

from which we calculate the bilayer arc length as

$$L_{arc} = L_0(1 + \alpha_1 dT) - dL_1 \text{ or } L_{arc} = L_0(1 + \alpha_2 dT) + dL_2. \quad (\text{V.4})$$

The curvature of the bent bilayer beam can be obtained by

$$\frac{1}{r} = \frac{(\alpha_2 - \alpha_1)dT}{\frac{h}{2} + \frac{2}{h}(E_1 I_1 + E_2 I_2)\left(\frac{1}{E_1 h_1} + \frac{1}{E_2 h_2}\right)} \quad (\text{V.5})$$

where $h = h_1 + h_2$ denotes the total thickness and I_n ($n = 1, 2$) are second moments of area determined by $I_n = \frac{h_n^3}{12}$. Note that the Timoshenko model applies to Euler-Bernoulli beams only which confines its validity to slender beam only [Lim 19].

The thermally induced horizontal displacement of a bilayer beam can be obtained by

$$|dx| = r \left[1 - \cos\left(\frac{L_{arc}}{r}\right) \right]. \quad (\text{V.6})$$

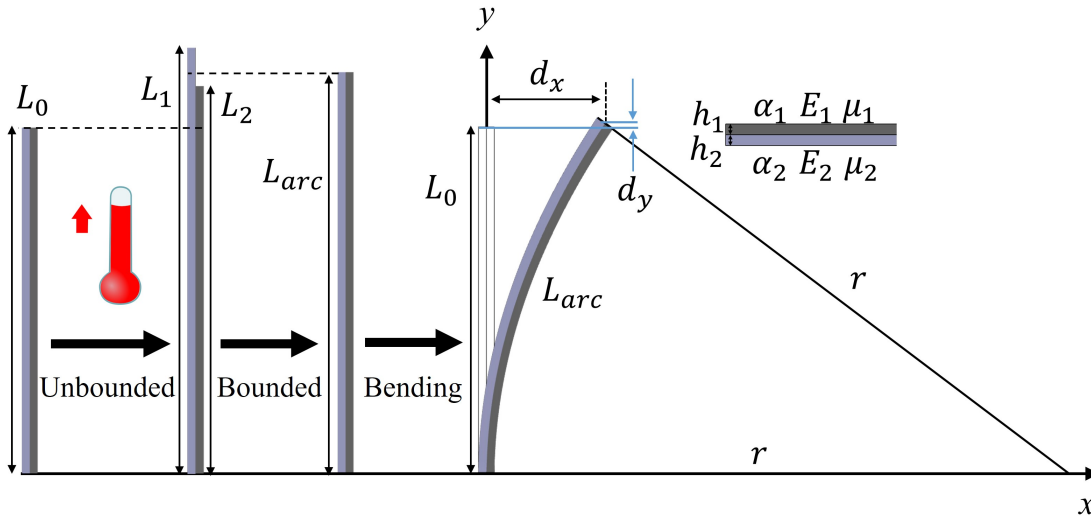


Figure V.1 – Illustration of the changes in bilayer beam length caused by thermal expansion.

Vertical displacement is also induced under temperature changes

$$|dy| = L_{arc} - r \sin\left(\frac{L_{arc}}{r}\right). \quad (\text{V.7})$$

We notice that vertical displacement is not needed in our design, which indeed has a negative influence. To obtain the maximum thermally induced motion and hence the best actuation performance, improvement of the bilayer beams was conducted. For a single bilayer beam under a thermal stimulus, both axial and tangential movements are induced. The end of a bilayer beam will be tilted (Fig. V.2a). Such a tilt angle at the end of the bilayer beams significantly reduces the effective motional amplitude of the whole structure. Instead of a simple single bimaterial beam, a S-shaped pattern is chosen here (Fig. V.2b). If two bilayer beams with inverted layer compositions are connected to form a S-shaped beam, indeed, the tilt angle at the end of the second beam is compensated for (see Fig. V.2) [Jia 09]. An overlap part was added to connect the two inverted bilayer beams, making the structures mechanically more robust. Besides, the overlap part largely facilitates the fabrication process.

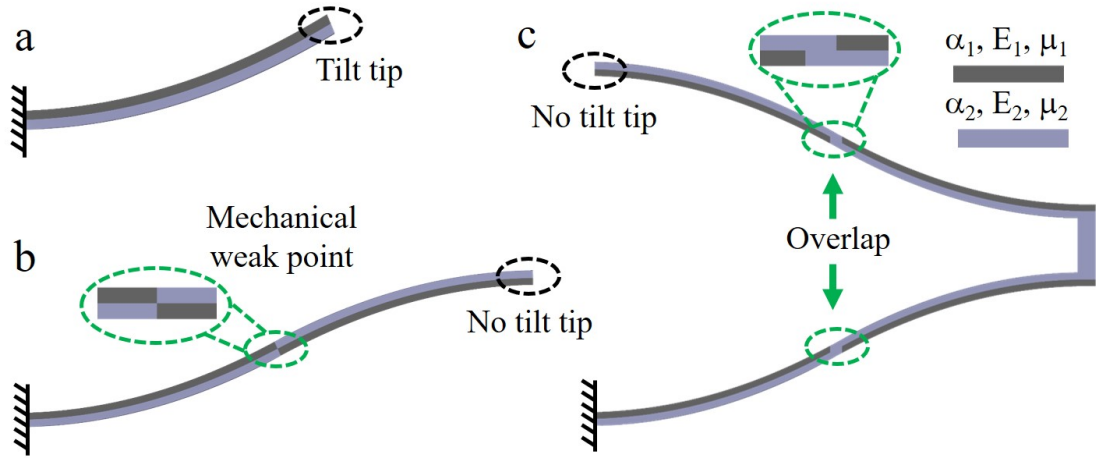


Figure V.2 – Deformation of the bilayer beams. (a) Schematic of a simple single bilayer beam showing the tangential tilt end in response to a temperature change. (b) Two bilayer beams with inverted layer compositions are connected to form an S-shaped beam. (c) The proposed structure with an overlap shows no tilt angle at the end of the beams. It is also mechanically more robust.

V.2.2 Design of thermally driven smart metamaterials

We start by designing two elementary robotic unit cells that produce either rotational or translational motion under a thermal stimulus (see Fig. V.3). We illustrate the operating principle of the elements as follows: the bilayer beam expands and bends upon heating, due to the difference in thermal expansion properties, giving rise to a net translation (rotation) of the element (see Fig. V.3b-c). For the constructed parameters we used in Fig. V.3 and for the temperature elevation of 40 K, we obtained a rotation angle of around 1.8° and an translational amplitude of $0.92 \mu\text{m}$, respectively.

Key parameters marked in the panels are: $\alpha_1 = 3.84 \times 10^{-5} \text{ K}^{-1}$, $\alpha_2 = 4.67 \times 10^{-5} \text{ K}^{-1}$, $E_1 = 3.98 \text{ GPa}$, $E_2 = 3.9 \text{ GPa}$, $\mu_1 = \mu_2 = 0.4$, $h_1 = h_2 = 3 \text{ }\mu\text{m}$, $h_3 = 54 \text{ }\mu\text{m}$, $h_4 = 21 \text{ }\mu\text{m}$, $h_5 = 36 \text{ }\mu\text{m}$, $h_6 = 12 \text{ }\mu\text{m}$, $h_7 = 33 \text{ }\mu\text{m}$, $L_1 = 57 \text{ }\mu\text{m}$, $L_2 = 63 \text{ }\mu\text{m}$, $L_3 = 18 \text{ }\mu\text{m}$, $L_4 = 15 \text{ }\mu\text{m}$, $L_5 = 48 \text{ }\mu\text{m}$, $w_1 = 15 \text{ }\mu\text{m}$, $w_2 = 24 \text{ }\mu\text{m}$, $d_1 = 48 \text{ }\mu\text{m}$.

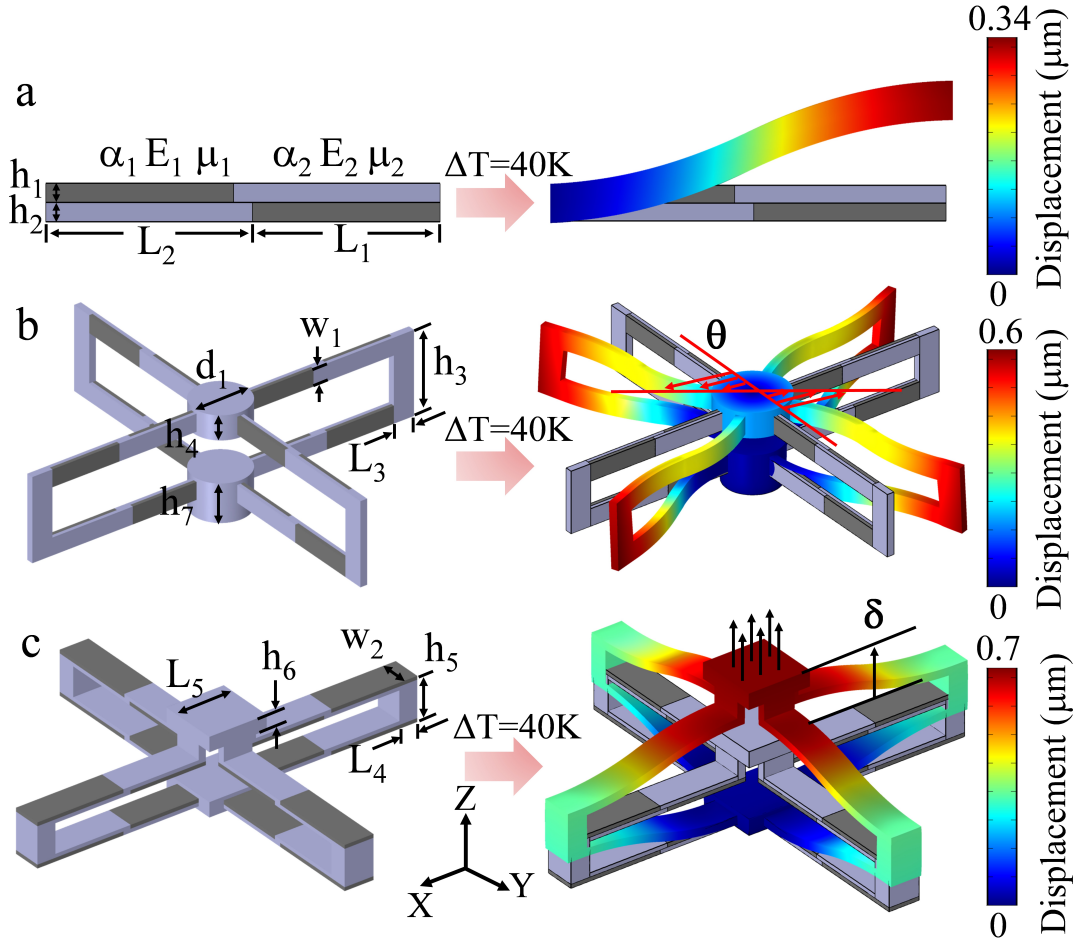


Figure V.3 – Illustration of the operating principle of rotational and translational stages. (a) Bi-material beam and its deformation under a change in surrounding temperature of 40 K. (b-c) Operating principle of the translational and rotational elements, respectively. The component with higher (lower) CTE is depicted in blue (gray). The initial positions of the elements are outlined for visual comparison. The directions of motion are indicated by arrows. For clarity, deformations in panel (a) and panels (b-c) are scaled by 10 times and 40 times, respectively.

The elements can build up a functional stack and further assemble into a robotic arm with three orthogonal orientations (see Fig. V.4). Such a robotic arm can realize multiple movements based on rotation and translation along each axis, which is vital to position a robotic tip in space. The induced translational (rotational)

motion of each element accumulates and enlarges the motional amplitudes at the end of the stack. By tailoring the translation (rotation) amplitudes for each axis, the robotic arm is capable of performing three-dimensional (3D) motion in response to an external thermal stimulus (see Fig. V.5). In addition, the motional amplitude of the tip end is well controlled by temperature changes.

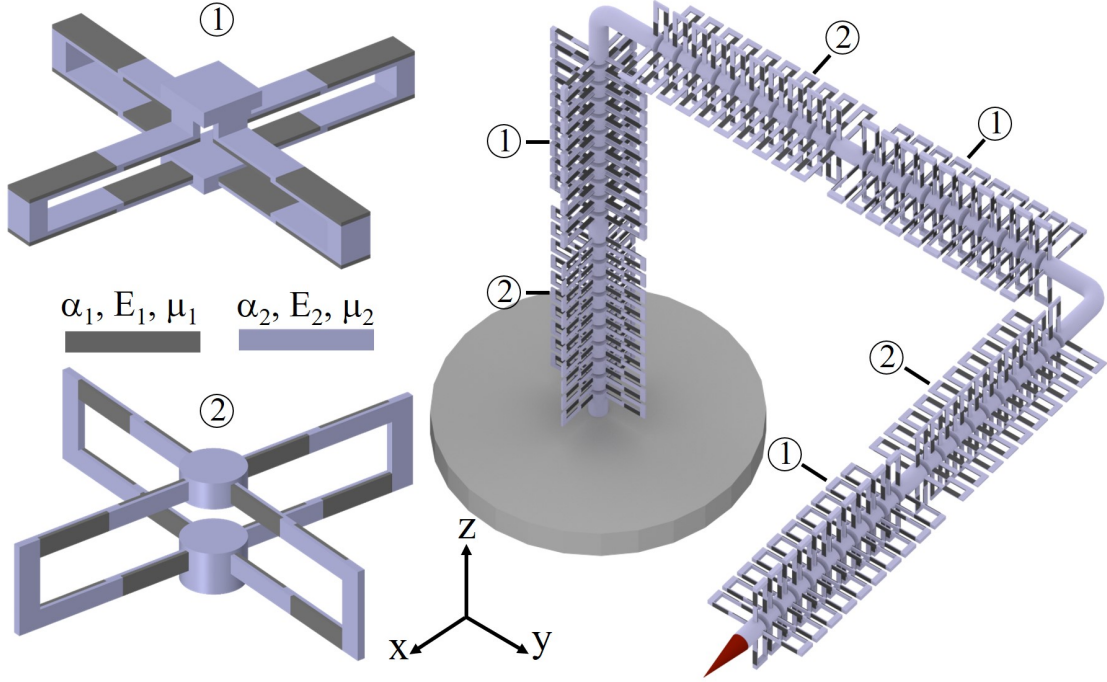


Figure V.4 – A microrobot consists of a three-dimensional assembly of rotational and translational elements. Along each axis, rotation and translation are produced upon temperature changes. Accumulation of these motions along each axis leads to mobility of the tip end (marked in red). The micro robotic arm can position the tip end in space controlled by external temperature changes.

V.2.3 Fabrication technique

In this work, we use 3D gray-tone two-photon lithography to fabricate complex two-component metamaterials. It is far from trivial to fabricate such structures with two different materials in a single step at the micro-scale. We note from Eq. (V.1-V.6) that the key to thermally responsive metamaterials primarily lies in the thermal expansion properties of the two different components. It was demonstrated in references [Qu 17, Rys 19] that the coefficient of thermal expansion (CTE) does not only depend on the type of polymer used, but for a given monomer it also depends on the laser writing power during photo-polymerization. As a proof, we have fabricated bulk polymer cubes with different writing powers (side length $50 \mu\text{m}$, made from IP-Dip, Nanoscribe GmbH) and we have measured their CTEs. In the fabrication process, an average value of 20 mW is defined as the reference

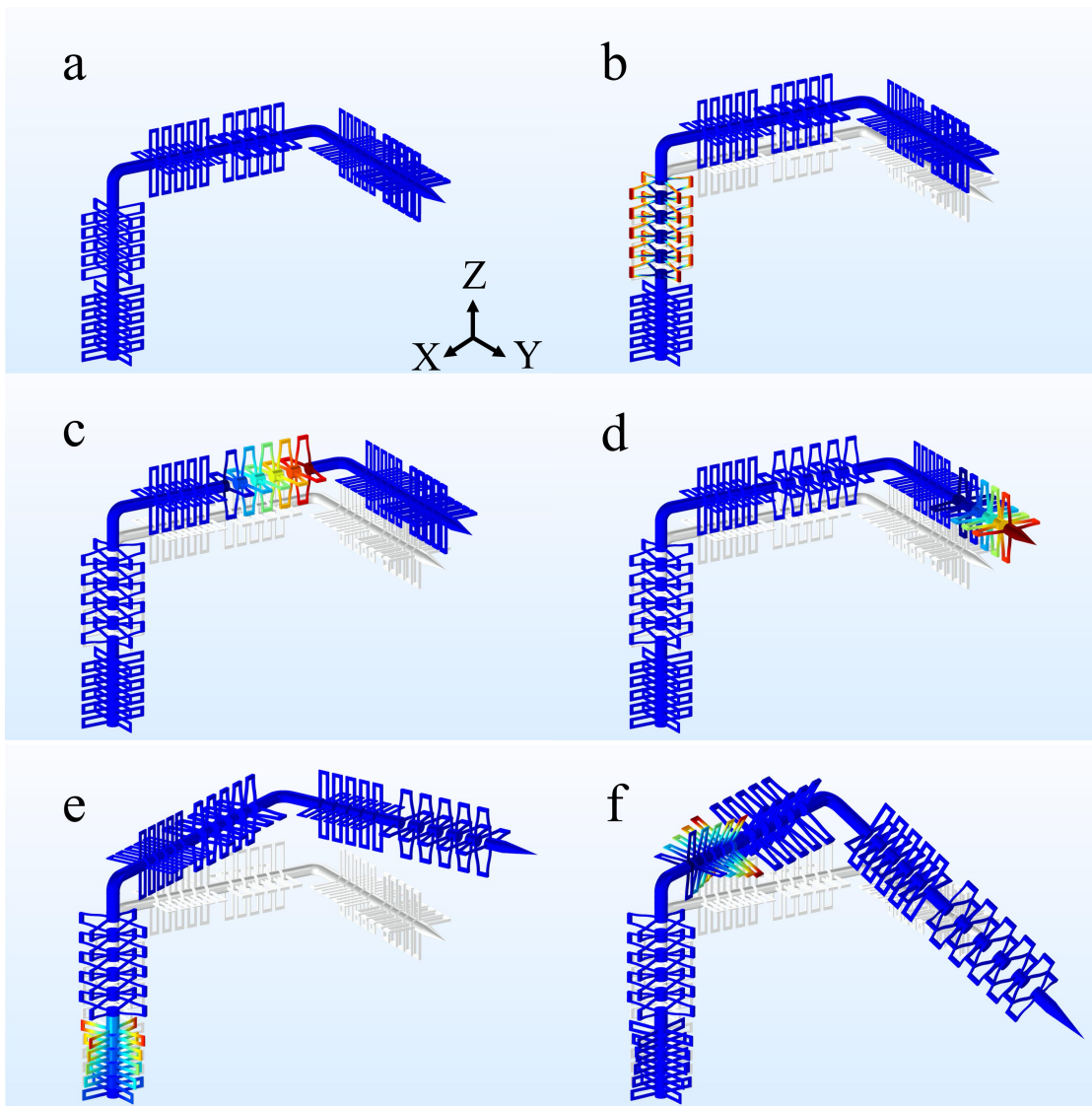


Figure V.5 – Illustration of controlling the motions of the microrobot by thermal stimuli: (a) a microrobot with each stack composed of five elements, (b-d) the tip end changes its position with thermally induced translation in Z , X and Y orientation, respectively. (e-f) the tip end changes its position with thermally induced rotation along Z and X orientation, respectively. As comparison, the original position is depicted by the white configuration.

power. The actual power is given by the reference power times the power scaling factor, which is varied locally in the spirit of gray-tone lithography. We change the power scaling factor (and hence the exposure power) to fabricate different cubes (see Fig. V.6a). During the measurement, we heat each polymer cube with a thermal gradient $\Delta T = 50$ K and capture images of the deformation. By using the public domain image processing software ImageJ, we proceed to convert each image to 8-bit format, then define edges and consequently convert the images to

binary ones. Closing and filling algorithms are successively performed to obtain the internal areas defined by the edges (see Fig. V.6f,g). Finally, based on the obtained areas measured in pixels, we estimate the CTE following

$$\alpha_L = \frac{A_f - A_b}{2A_b\Delta T} \quad (\text{V.8})$$

where A_b and A_f are the areas obtained from images captured before and after heating, respectively.

The mechanical properties (here Young's modulus E) for different laser powers are also obtained by measuring the aforementioned bulk polymer cuboid samples. Brillouin microscopy is employed here, as it offers non-invasive access to the internal micromechanics of soft structures at optical resolution. Recent reports have interpreted Brillouin micrographs in terms of the Young's modulus for cells and tissues [Scarcelli 11, Scarcelli 15, Zhang 17]. We use Brillouin light scattering to measure the longitudinal elastic modulus (see Fig. V.7), following

$$M_L = \rho \left(\frac{\lambda\omega_b}{2n \sin(\frac{\theta}{2})} \right)^2 \quad (\text{V.9})$$

where M_L is the longitudinal elastic modulus, λ and θ are the wavelength and angle between the incident and scattered wave vectors. λ and θ are typically prescribed by the step of the Brillouin microscope, taken to be 532 nm and π , respectively. Refractive index n and density ρ are 1.5534 and 1000 kg/m³, respectively. The Brillouin frequency shift was measured based on the frequency difference between the Rayleigh and the Stokes peaks, as described below. Young's modulus was then obtained from

$$E_L = M_L \frac{(1 + \nu)(1 - 2\nu)}{1 - \nu} \quad (\text{V.10})$$

where ν is Poisson's ratio taken as 0.4 here. We note that only the ratio E_1/E_2 actually enters into the effective deformation of bi-material beams [Qu 17].

The correlation between the CTE and Young's modulus versus the laser exposure power are established in Fig. V.8. We observe that the CTE decreases (Young's modulus increases) approximately linearly with the laser exposure power. We thus demonstrate that different materials properties can be realized with a single material system but varied local exposure powers. Specifically, Young's modulus for polymers written by laser exposure factor 50% and 45% are obtained as $E_1 = 3.98$ GPa and $E_2 = 3.9$ GPa, respectively. CTEs for polymers written by laser exposure factor 50% and 45% are obtained as $\alpha_1 = 3.84 \times 10^{-5}$ K⁻¹ and $\alpha_2 = 4.67 \times 10^{-5}$ K⁻¹, respectively.

As a proof of demonstration, we fabricate bilayer beams with two components defined by two different power scaling factors and beams with a single component for comparison (see Fig. V.9). Observations show that the two-component beams deform and bend as the surrounding temperature changes, but also that they shrink during development, whereas the single-component beams are almost not influenced by temperature variations, demonstrating that the two components

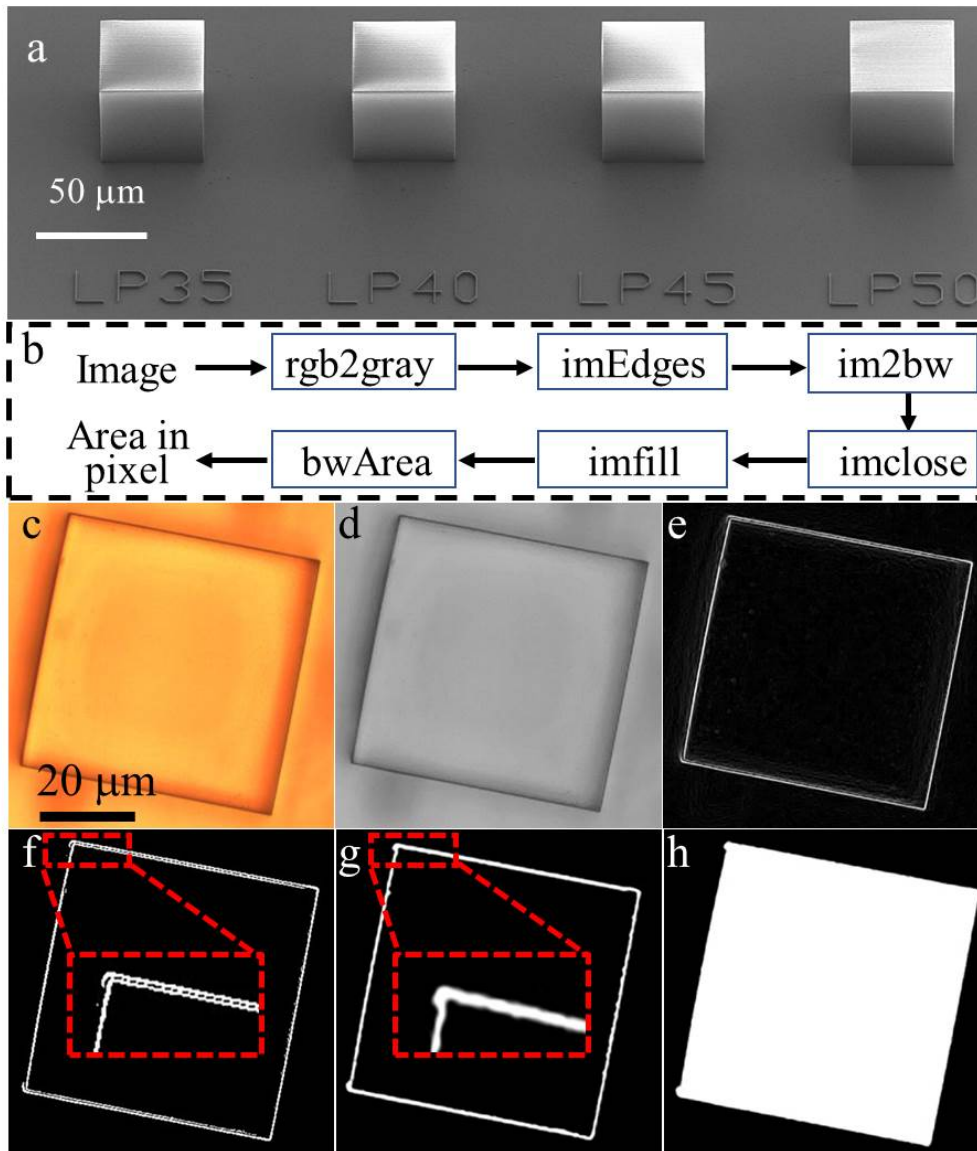


Figure V.6 – The CTE versus laser exposure power is obtained by measuring areas before and after heating. (a) Bulk polymer cubes written by different laser power scaling factors. (b) Outline of the general process in ImageJ to obtain areas measured in pixels: the optical image of a polymer cube in panel (c) is first converted into 8-bit format in panel (d). Then an edge detection algorithm is applied and the image is converted into a binary image in panel (e). After applying closing algorithms in panel (f) and filling algorithms in panel (g), we finally obtain the internal area defined by these edges in panel (h).

indeed have different properties. We thereby safely validate the fabrication strategy and demonstrate the possibility of printing a microrobot in only one step using a single photoresist and gray-tone lithography.

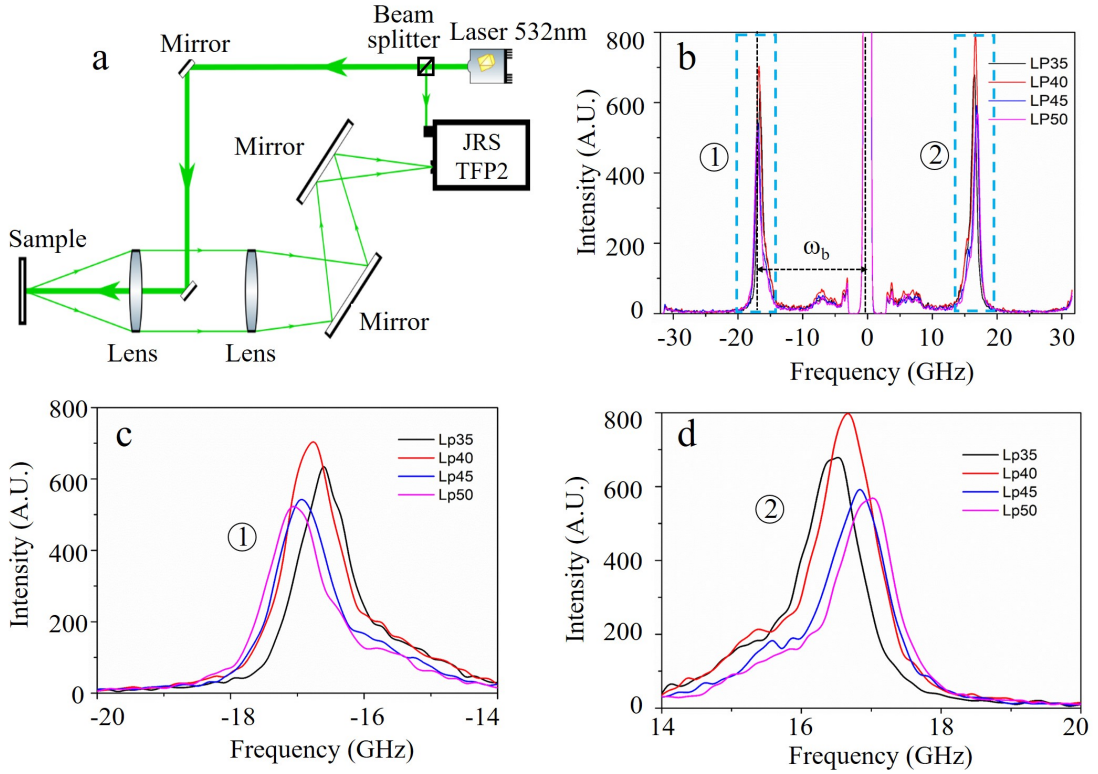


Figure V.7 – Measurement of mechanical properties. (a) Schematic of the Brillouin microscope. (b) The Brillouin frequency shift ω_b of longitudinal phonons is determined as the peak of the scattered intensity. (c, d) Magnified views of the left and right peaks, where the frequency differences between different cubes are clearly observed.

V.2.4 Sample fabrication

Based on the above laser writing strategy, we fabricate the metamaterials depicted in Fig. V.3 using a single photoresist but two laser writing powers. The rotational and translational stacks were both assembled in the z -direction by 5 elements. Samples were fabricated using a negative tone photoresist (IP-Dip, Nanoscribe GmbH) and a commercial 3D gray-tone two-photon lithography system (Photonics Professional, Nanoscribe GmbH). A drop of resin was deposited on a fused silica substrate with dimensions $25 \times 25 \times 0.7 \text{ mm}^3$ and photopolymerized with a femtosecond laser operating at $\lambda=780 \text{ nm}$. After printing, the sample was developed for 20 min in Propylene glycol methyl ether acetate (PGMEA) solution to remove the unexposed photoresist and rinsed for 3 min in Isopropyl alcohol (IPA) to clear the developer.

In the fabrication process, the reference power was defined as 20 mW. The actual power was given by the reference power times the power scaling factor, which was varied locally in the spirit of gray-tone lithography. We construct the less active component with a laser power scaling factor of 50% and the more active

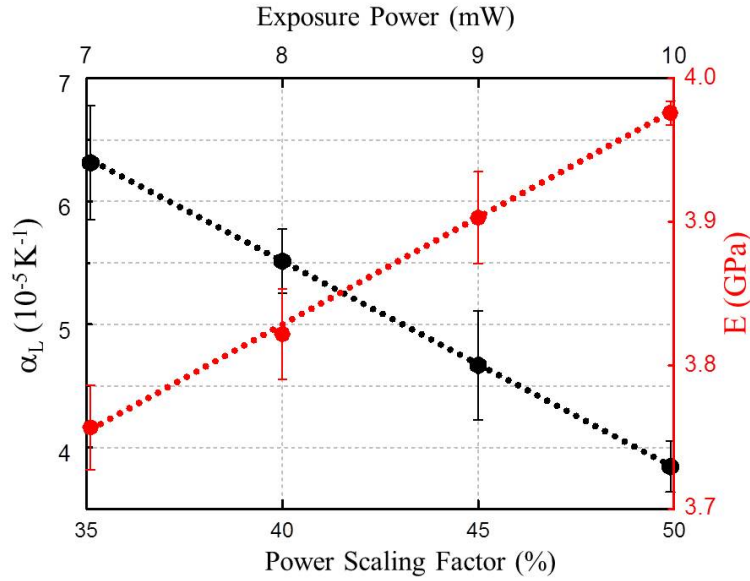


Figure V.8 – CTE and Young’s modulus versus different laser powers. The bottom horizontal axis gives the power scaling factor whereas the top horizontal axis gives the actual power. Standard deviations are added. The CTE decreases (Young’s modulus increases) with the laser exposure power. Both variations are approximately linear.

component with a factor of 45%. The more active component was first fabricated with a power scaling factor 45% (9 mW). Then the laser was drifted and another component was fabricated with power scaling factor 50% (10 mW).

Clearly, a larger difference in selected power scaling factors would bring in larger motional amplitudes; however, it would also add more difficulties during fabrication and would specially lead to less repeatable motions for poorly exposed polymers. Here, we aim at designing an accurate and repeatable response, we thus must use the less damageable material. Poorly exposed polymer structures are indeed porous, they shrink a lot and they are thus not resistant to ambient conditions. We have fabricated polymer cubes (side length $20 \mu\text{m}$, made from IP-Dip, Nanoscribe GmbH) with different power factors. It was observed in Fig. V.10 that the polymer cubes became more porous and the quality deteriorates with increasing power factors.

We further fabricated samples using the power factors less than 70 %. It was found that samples with a larger difference in laser powers are more prone to fabrication imperfections. Herein we present some samples in Fig. V.11. One group of samples are fabricated by combining laser power factors 65 % and 45 %, while another group combined laser power factors 70 % and 45 %. The samples consist of 5 layers. We checked each layer and show optical micrographs of the samples. In some layers, the bi-layer beams are disconnected and some parts of the beams are even missing. This is caused by the huge difference in shrinkage during development. By contrast, with the chosen power scaling factors (45 % and 50 %)

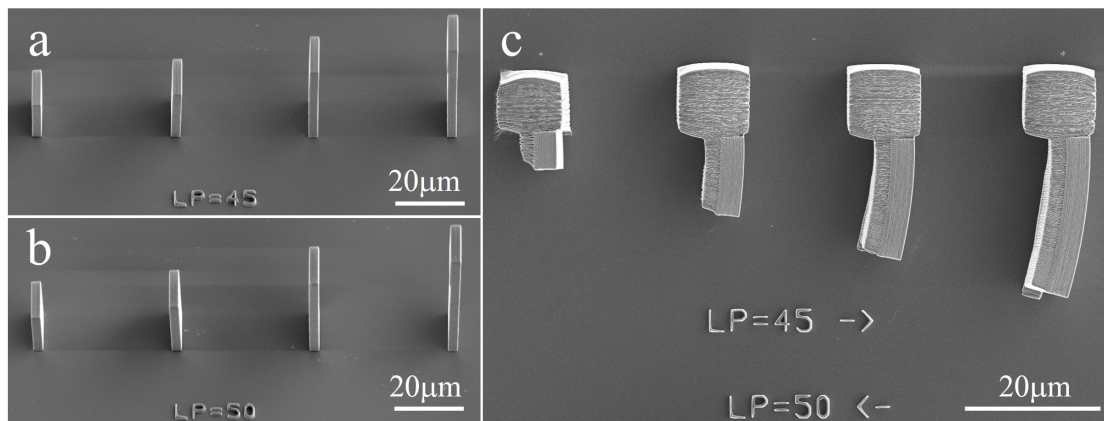


Figure V.9 – Electron micrographs of (a, b) beams fabricated by single laser exposure power and (c) two-component beams fabricated using different laser powers. The beam lengths from smallest to largest are $10\ \mu\text{m}$, $20\ \mu\text{m}$, $30\ \mu\text{m}$ and $40\ \mu\text{m}$, respectively. In the images, "LP" is the abbreviation of exposure laser power and the numbers denote the power scaling factors as a percentage of a nominal power. Pre-bending of the bi-material beams is observed and originates from the different volume shrinkages of the two different components during development.

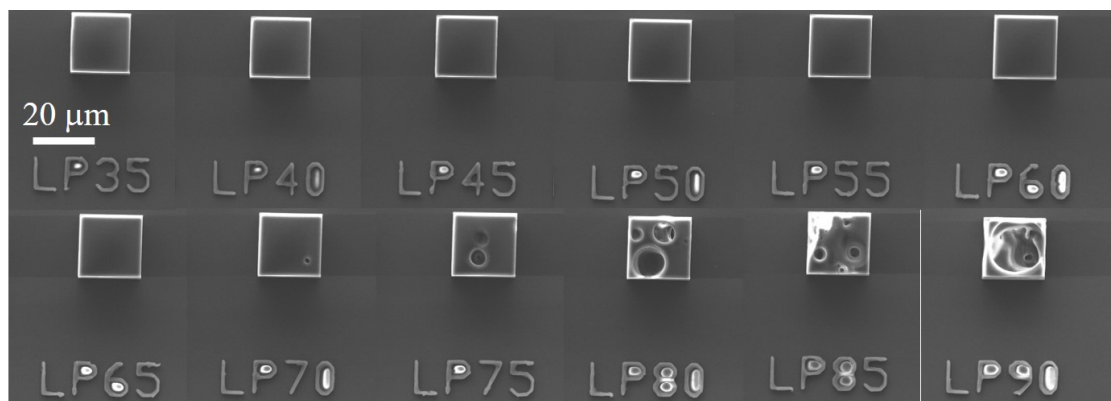


Figure V.10 – Electron micrographs of cubes fabricated by the same polymer but different exposure powers. The reference power is 20 mW. The material got more porous with the increment of laser powers

the fabricated samples show better mechanical stability and fewer imperfections. The compromise between functionality and quality of structuration leads to these two powers.

Optical and scanning electron microscopy (SEM) micrographs of the fabricated stacks with selected power scaling factors 45 % and 50 % are shown in Fig. V.12. The built components look alike in optical and electronic images, but that they are actually different in their thermal and mechanical properties. We notice the pre-bending of bi-material beams, which originates from different volume shrink-

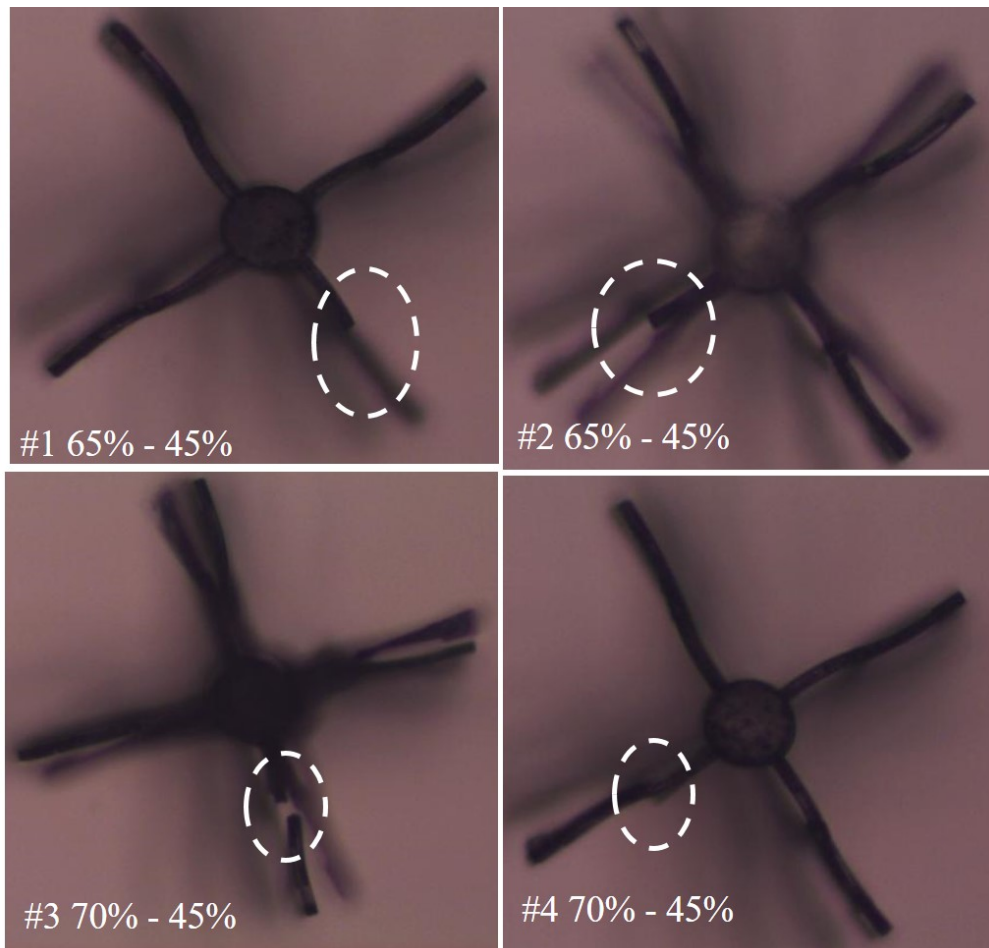


Figure V.11 – Optical micrographs of the samples showing fabrication imperfections. The larger the difference in shrinkage during development, the less resistant the beams are to ambient conditions.

age during the development process. Within the linear regime, this pre-bending does not change the thermal operation. Instead, it directly evidences that the two components with different exposure powers are different in their thermal and mechanical properties. We can also notice the rotation (or translation) that results from pre-bending, in agreement with the designed operation principle.

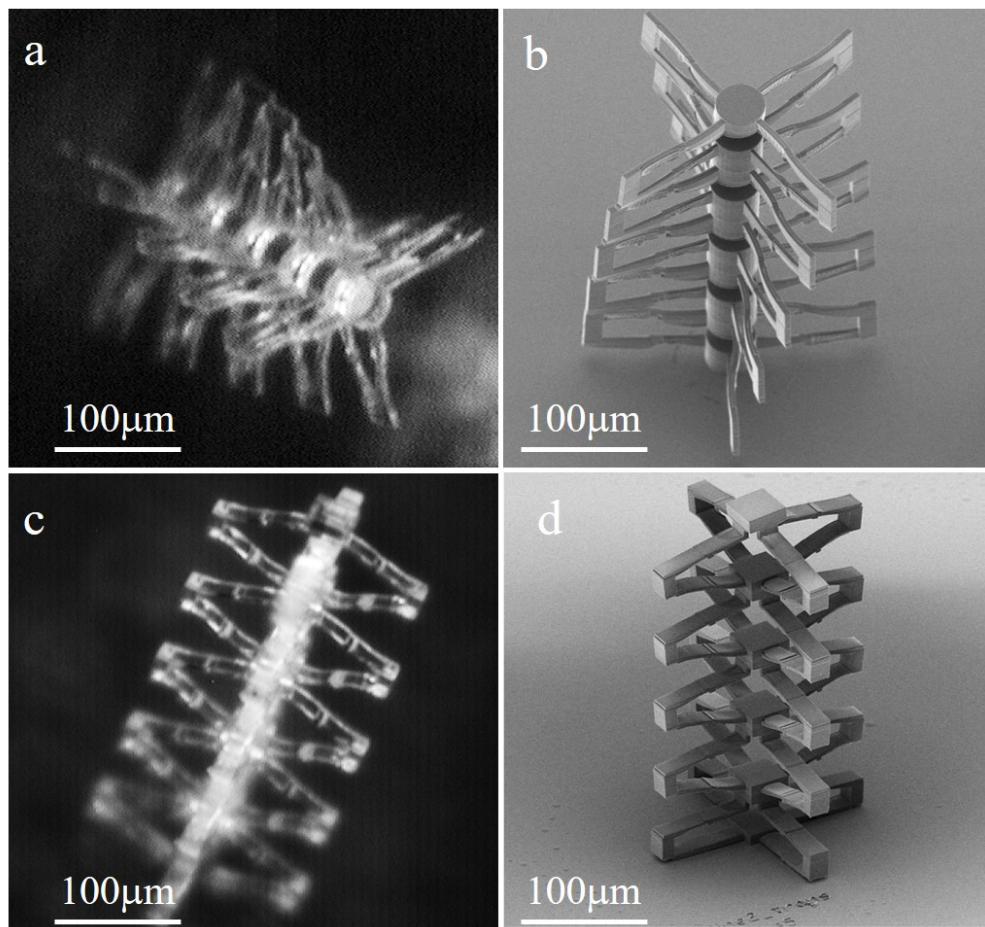


Figure V.12 – Functional stacks fabricated by gray-tone lithography. (a) (c) Optical micrographs and (b) (d) SEM images. Each stack is composed of five elements. The samples are composed of two constituent components fabricated with a single photoresist but two different laser exposure powers. Differential shrinkage during development leads to pre-bending of the bi-layer beams, further leading to rotation (translation) of the stack shown in the panels.

V.3 THERMALLY DRIVEN MOTIONS

V.3.1 Concept validation

To test the concept, we discuss the actuating performance of the functional stacks (see Fig. V.13). We use an electronic beam as external stimulus. Upon electron beam heating (for about 10 seconds), the structures exhibit a thermal-mechanical response with corresponding motion. We wait for a given time (here 60 minutes) for the environment and the samples to naturally cool back to the initial temperature. Note that such long cooling times are needed due to the absence

of active cooling. When external heating is released, motion gradually decreases until the initial rest point is retrieved. Such an observation suggests that the thermal-driven behavior is sensitive and reversible.

The electron heating process is conceived to conceptually and visually show the actuation mechanism. Due to the nature of heat diffusion and the fact that polymers are bad heat conductors, motion is mainly observed at the top layer. Considering the inaccuracy in controlling temperatures and heating/cooling speed, we quantitatively characterize actuation behavior in an enclosed chamber under well controlled external thermal conditions. The characterization is conducted in the dry environment which is more practical and widely used in engineering applications. In literatures, simple bending behavior of micro-beams under temperature changes are demonstrated in aqueous environment, which is easier for the experiment but will damage the porous polymer materials we used.

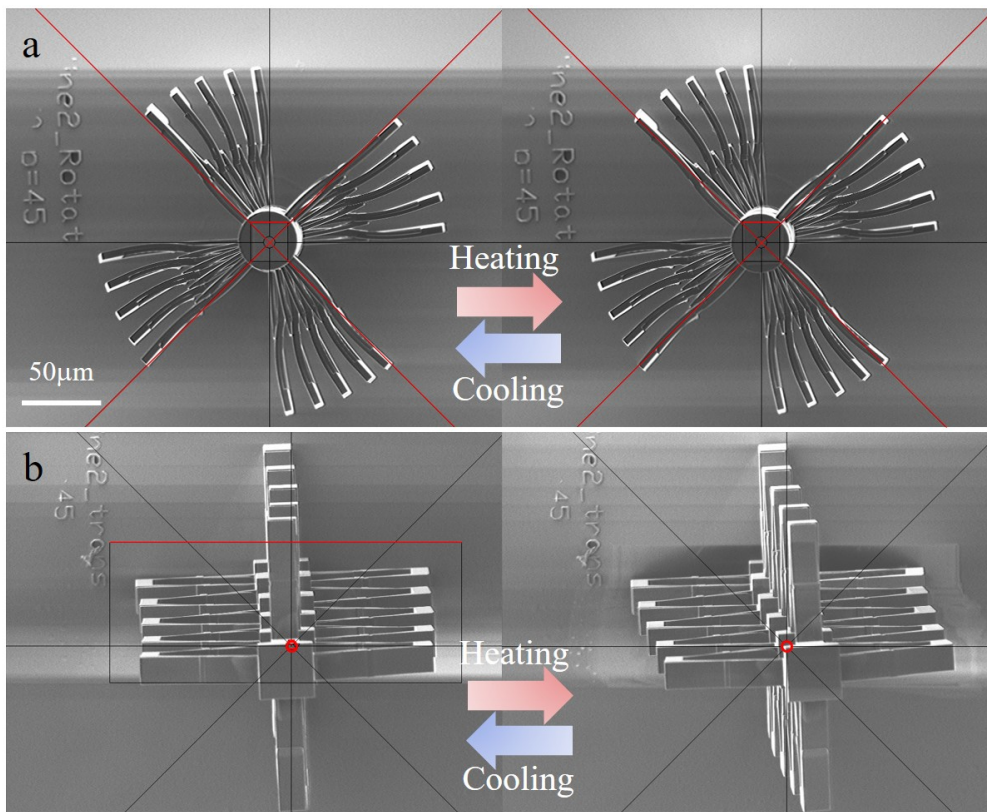


Figure V.13 – Conceptual validation of the actuation mechanism of (a) rotary lattices and (b) translation lattices. The thermal stimulus was applied on the top end of the structures by electronic beam exposure. When the thermal stimulus was set on, the structures showed overall motion; when the stimulus was set off, the relative deformation and motion disappeared gradually, demonstrating a sensitive and reversible thermal-driven process. The red cross-lines in panel (a) and the central circle are added to make deformations clearer.

V.3.2 Quantitative analysis on thermally driven motions

In order to evaluate quantitatively the thermally induced actuation mechanism, we conduct finite element analysis (FEA) and temperature-dependent measurements to check whether the structures behave exactly as designed. For FEA, we use the commercial software COMSOL Multiphysics. In the experiments, the structures are heated in an enclosed chamber with well controlled temperatures. We apply image cross-correlation analysis to obtain the temperature-induced displacement field and hence reveal the motion mechanism. Figure V.14 summarizes the temperature-dependent measurement results. It is observed in Fig. V.14a,c that the rotational and translational amplitudes increase linearly with the thermal gradient, in good agreement with FEA. Desired motional amplitudes can hence be accurately achieved by applying predefined temperature variations. Besides, motional amplitudes decrease to zero as the temperature returns to its initial value, revealing a well reversible performance. These results quantitatively demonstrate that the designed structures feature an accurate and reversible behavior under thermal stimuli.

The numerical and experimental results for the translational structures under temperature elevation 75K are then compared with theoretical prediction (obtained from Eq. V.6), shown in Table V.1. It is observed that the differences are all within an acceptable range, showing that the proposed structures are accurate in thermally controlled behavior. We also note that in the rotational structures the junctions also play a very important role and thus we switched to full 3D FEM model to avoid making too crude theoretical approximations on the design. Therefore, we displayed and compared the experimental and FEA results to validate the accuracy of our proposed structures.

	Normalized Disp.	Difference
Theoretical	14 ‰	0
Numerical	14.89 ‰	6.3%
Measure 1	15.12 ‰	8%
Measure 2	12.95 ‰	7.5%
Measure 3	13.45 ‰	4.2%

Table V.1 – Comparason between theoretical, numerical and experimental results for the translational structure.

We observe minor differences between the measured results, FEA results and theoretical predictions. The uncertainty mainly originates from the inaccuracy of the measured CTE and Young’s moduli. Imperfections of the fabricated samples also add to these differences. For example, due to a drift during writing, the two layers in some of the bi-material beams may not be well connected, even to the extent of detaching. We should note that in our design (especially for the rotation structure) the junctions also play a very important role and thus we switched to full 3D FEM model to avoid making too crude approximations on the thermally

induced motion. Therefore, we mainly display and compare the experimental and FEA results to validate the accuracy of our proposed structures throughout the work.

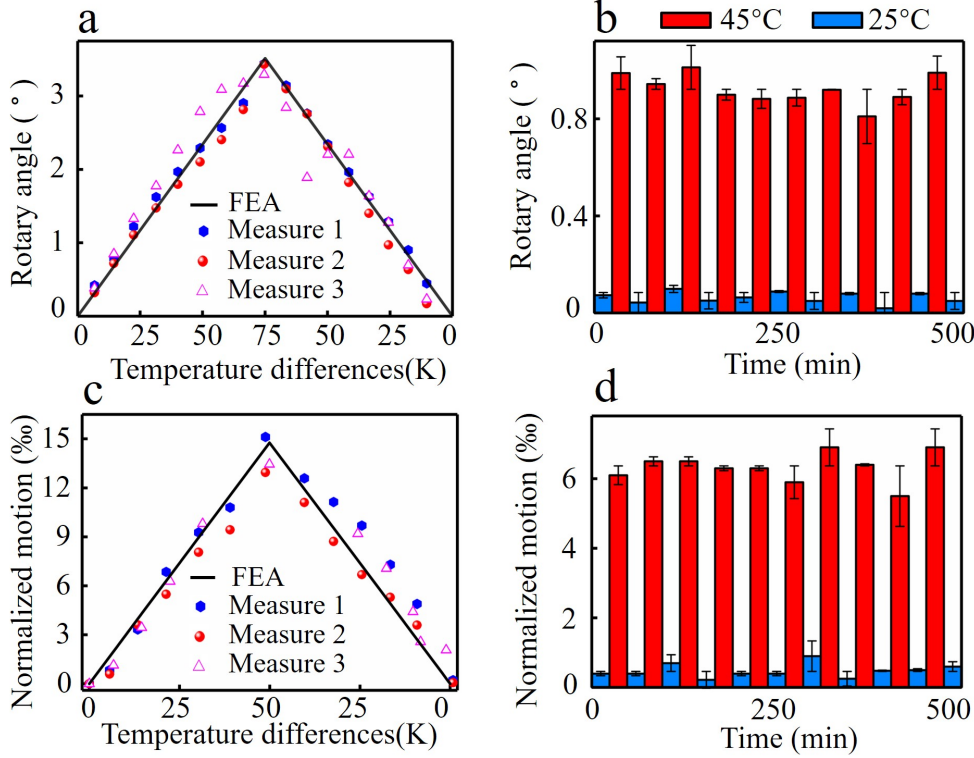


Figure V.14 – Temperature-dependent measurement of the fabricated stacks. (a) (c) Dependence of motional amplitudes of the stacks with the thermal gradient for rotation and translation, respectively. The plots show a symmetric, linear and reversible amplitude response. (b) (d) Cyclic stability of the structures for rotation and translation, respectively, where temperatures are switched between 25°C (marked in blue) and 45°C (marked in red). The error bars (marked in black) show the difference between experimental and numerical results. Note that the translational displacements in panels (c-d) are normalized to the initial non-heated stack length in the z -direction.

To check the robustness of the thermally-driven operation, we test the functional stack under several heating-and-cooling cycles. Both the heating process and the cooling process last for 25 minutes during each cycle, ensuring that the system can reach its steady state. Hence, the full cycle time of a reversible switch is 50 minutes for the thermal cycling conditions used. As shown in Fig. V.14b, the rotation angle changes from around 0.08° to 0.92° as temperatures are switched from 25°C to 45°C. This actuation is reversible and repeatable upon several heating-and-cooling cycles, and the thermally-induced motional amplitudes are stable with small deterioration, which demonstrates a predictable long and stable working life. Similar relations of translational stacks are also observed in Fig. V.14d.

V.3.3 Parameter analysis for further optimization

One may raise concerns regarding the small motion produced by the samples. In this work, the samples are fabricated to demonstrate extremely accurate and reversible operation, at the sacrifice of motional amplitudes. However, the observed motion is still comparable to what has been reported in the literatures for micro-structured thermally responsive metamaterials in a dry environment [Qu 17] and it has to be emphasized that actuation is remotely controlled and does not rely on an external mechanical actuation as is often the case.

We investigated by numerical simulation the relationship between motional amplitudes and constructed parameters (see Fig. V.15). It is found that the thermally induced amplitudes increase linearly with the increment of the aspect ratio and the differences between CTEs. More built layers will also add the amplitudes at the end of the stacks. Therefore, the amplitudes can be effectively adjusted by tuning structural and material parameters, or imposing larger temperature variations.

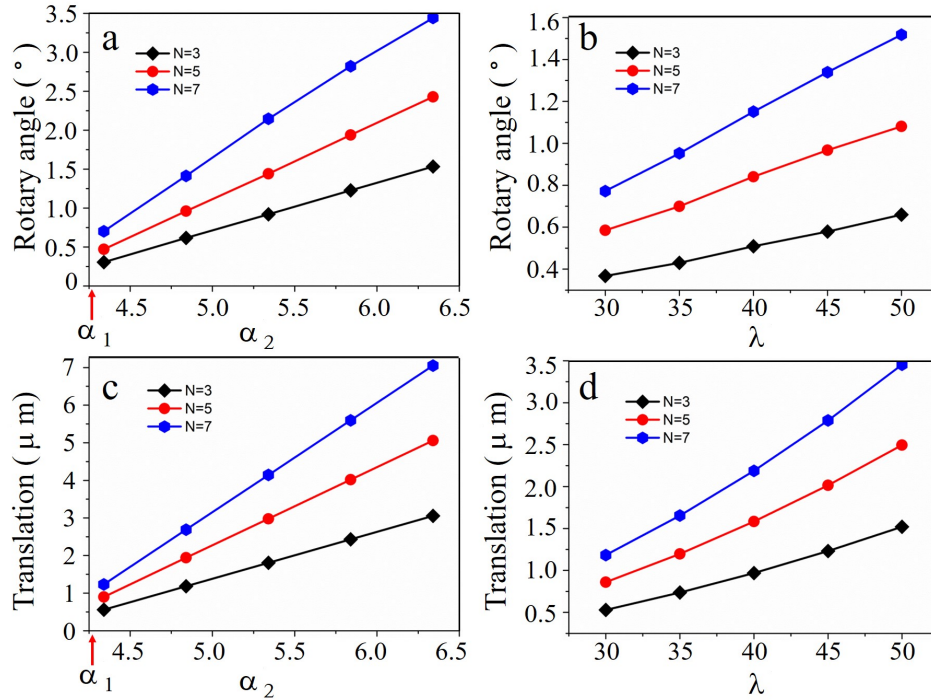


Figure V.15 – Influence of key parameters on motion amplitude. (a,c) Dependence of motion amplitude on thermal expansion coefficients for structures with 3, 5 and 7 layers, respectively. Note that α_1 is fixed and marked out in red, while α_2 is varied. (b, d) Dependence of motion amplitude on geometrical properties for structures with 3, 5 and 7 layers, respectively. Here we define the aspect ratio as $\lambda = \frac{L_1+L_2}{h_1+h_2}$, or the ratio between length and thickness for the bi-material beam. Geometrical nonlinearity has been accounted for.

V.4 THERMO-MECHANICAL PERFORMANCES

We finally estimate the potential torque (or force) that the designed structures can produce to move an object. The analysis of mechanical responses requires the correlation of the motional amplitude to an external load. Thereby, we use numerical calculations with the commercial software COMSOL Multiphysics. In our simulations, we consider a rotational (or translational) element with a torque (or force) applied to the sideways surface (or to the top end) in the opposite direction to the thermally induced displacement. A temperature elevation of 20 K is then imposed. Motional amplitudes are obtained versus increasing weight loading. The load-carrying capability is characterized by the applied load and by the specific work that the elements produce under the temperature elevation. The rotational (translational) elements work like Hooke's torsion (linear) springs by twisting (pushing) the end along its axis. Specifically, when a rotational (translational) element undergoes a temperature elevation, it exerts a torque (force) on external objects that is proportional to the angle (displacement), in analogy with a spring in a twisted (compressed) state (see the insets in Fig. V.16a,b). Note that the torsion (linear) spring strictly obeys Hooke's law, as the elastic limit is not reached in this work (see Fig. V.16c,d). We calibrate the cells as Hooke's springs and obtain the torsion coefficient (stiffness) for the rotary (translational) cell by linear fitting as $28453 \mu\text{N} \cdot \mu\text{m}/\text{rad}$ ($6.76 \mu\text{N}/\mu\text{m}$).

With increasing weight loading, the actuation angle (displacement) decreases linearly while the specific work first increases to the maximum value of $59 \times 10^{-3} \text{ J/kg}$ ($1.1 \times 10^{-3} \text{ J/kg}$) and then decreases gradually. Importantly, elements with a temperature elevation $\Delta T = 20\text{K}$ can offer a considerable actuation torque (or force) that is able to move roughly 1000 times their own weight (see Fig. V.16a,b). The results are comparable with the characterization results in literature [Kotikian 18] in which, however, only contraction at the millimeter scale are demonstrated. Note that one can obtain larger actuation torque (or force) by simply imposing larger temperature variations or by adjusting construction parameters.

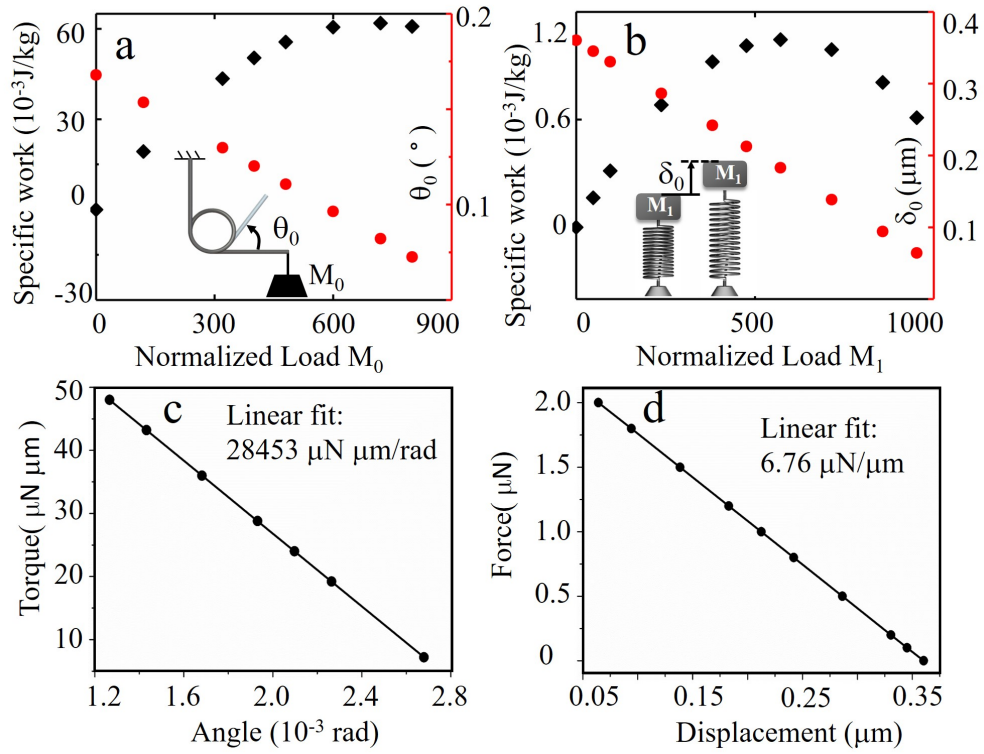


Figure V.16 – (a,b) The specific work (i.e., the work normalized to the mass of the structure) and the actuation motion of the elements under thermal stimuli are plotted versus the normalized load and represented in analogy with Hooke’s springs. Loads M_0 and M_1 have been normalized by the mass of the rotational element (2.5×10^{-10} kg) and translational element (2.1×10^{-10} kg), respectively. (c,d) Mechanical behavior of the elements. Torsion coefficients and stiffness in analogue with springs are obtained.

V.5 SUMMARY

In summary, we have developed thermomechanical metamaterials that achieve elementary motions (rotation and translation) under thermal stimuli and can further assemble into a three-axis microrobot. The thermally driven behavior is obtained in a controlled manner and in a dry environment. The proposed metamaterials are fabricated using a single polymer but two different laser writing powers, thus making each part different in its thermal and mechanical properties. We verified that the designed compact metamaterials show accurate, stable, and reversible response through numerical simulations and experiments. Their operation can be easily and accurately controlled by external thermal sources, with great potential in microrobotics and other related domains.

Conclusions and outlook

This thesis considered the design of thermal metamaterials, including thermal metadevices that manipulate heat flux and thermomechanical metamaterials that deform in response to heat stimuli. The specific contributions of this work are as follows.

1. A method of designing 3D arbitrary shaped thermal cloaks was presented, following a simple linear transformation. The resulting properties are anisotropic but inhomogeneous, which is simplified to engineering manufacture and can be realized easily with layered structures.
2. We establish a general road map to build thermal harvesting devices utilizing microstructures design. The devices are realized by naturally available materials. We demonstrate that this approach is applicable to a variety of microstructures which adds great flexibility to practical application.
3. A selective emission technique is proposed to realize manipulation of thermal radiation. Based on this approach, infrared camouflage, thermal coding and thermal illusion functionality are achieved and presented.
4. We design thermomechanical metamaterials towards microrobots using the bilayer beam scheme. The proposed actuating metamaterials can realize basic deformations (rotation and translation) under thermal stimuli. We verified excellent reversible, accurate and stable thermally induced performances by simulations and experiments.

These contributions are expanded in details as follows.

In general, transformation optics based cloaks produce properties that are anisotropic and inhomogeneous. For heat cloaks with arbitrary shapes, the properties are more complicated. To make them easier, three dimensional arbitrarily shaped cloaks were proposed with homogeneous materials properties. As most arbitrarily shaped cloaks can be approximated by polyhedra and further divided into a series of tetrahedra, we considered a linear mapping approach to design cloaks with tetrahedron shapes (i.e. tetrahedral cloaks). In this framework, homogeneous material properties are obtained for each division. We extended this approach to cloaks with more faces (8 faces and 32 faces) and cloaks with curved boundaries (cylindrical cloaks and spherical cloaks). Basing on the proposed approach, we analyzed the effectiveness of the polygonal cloak composed of an alternation of homogeneous isotropic layers, and noted that cloaking deteriorates at short times, then gradually becomes better.

We then proposed a general method to design thermal harvesting devices from naturally available materials. We designed a cross-shaped composite microstructure and calculated the effective conductivity by the two-scale homogenization

technique. The optimal Latin hypercube method was implemented to obtain geometrical parameters that can best mimic the desired transformed medium. It was found that with optimized parameters, the obtained conductivity has minor differences (less than 0.02%) compared to targeted values. We implanted the optimized microstructures into a thermal harvesting device. A sample was fabricated with copper by the CNC machining technique, and experiments were then conducted. Both numerical and experimental results demonstrate good thermal harvesting performance, thereby validating the effectiveness of the design method. To validate the wide application range of our approach, we illustrated other types of structures like split rings, alternative layered medium and void rectangles, and we showed that they also make thermal harvesting devices with excellent heat concentrating performances.

In addition to the above active control of in-plane heat conduction, we also investigated the manipulation of out-of-plane heat radiation. A multilayer film based selective emission strategy was proposed to realize flexible manipulation of thermal radiation within the infrared band 8 – 14 μm . Using this simple approach, we demonstrated spatial tunability and continuity in thermal emission. We validated this concept by constructing a multilayered medium with Carbon (thickness 4 μm) and ZnS film (tailorable thickness) on a silicon substrate. We showed that one can obtain a continuous change of emissive power by locally changing the thickness of the coating film ZnS. This technique was investigated for applications in infrared camouflage, thermal coding and thermal illusion. The technique features advantages of a simple structure, easy fabrication and size flexibility. Our work provides an alternative solution to infrared stealth and other thermal radiation management technology based on selective emission.

Using thermal stimuli as an additional physics, we have developed metamaterials that can achieve elementary motions (rotation and translation) towards microrobots, responding to external temperature changes. The thermally driven behavior is obtained at the microscale, in a controlled manner and in a dry environment. We fabricated the proposed metamaterials using a single materials system but varying local writing powers. It was found that components fabricated with larger writing powers show smaller Young's modulus and larger thermal expansion coefficients. We verified that the designed metamaterials show accurate, stable, and reversible response through numerical simulations and experiments. We finally estimated the potential torque (or force) that the designed structures can produce to move an object. The designed unit cells with a temperature elevation $\Delta T = 20\text{K}$ can offer a considerable actuation torque (or force) that is able to move roughly 1000 times their own weight.

Based on abovementioned works, we may go further on these aspects in the future, as detailed next.

Future work may partly focus on dynamic and tunable emissivity control. As mentioned in this thesis, thermal radiation can be manipulated by surface emissivity. In practical applications, the temperatures of the objects and surroundings can change dynamically. To achieve thermal camouflage responding to varying sur-

roundings, the emissivity should adjust itself correspondingly. Therefore, for the next step we may consider the design of metasurfaces that can tune their surface emissivity depending on thermal stimuli, realizing adaptive camouflage effects.

Controlling the directionality of an absorptive or thermally emissive material is a great challenge in contemporary materials and photonics research. High thermal emission at unwanted directions can lead to deteriorated effectiveness of the thermal devices like camouflage. Therefore, part of our future work will be on this aspect, that is, to design metasurfaces or metastructures that can realize thermal camouflage effects for broad angular ranges.

We have designed thermomechanical metamaterials controlled by external temperature changes. However, we sometimes need local deformation instead of the global one. In the next step, we plan to build metamaterials that respond to only selective laser wavelength ranges. Here, a laser will be employed as the heating source. In this way, we can choose which parts to deform intentionally, by simply selecting the laser wavelength used. This will imply great significance on the control of microrobots, micro/nano-actuators and so on.

Bibliography

- [Achaoui 20] Y. Achaoui, A. Diatta, M. Kadic & S. Guenneau. *Cloaking in-plane elastic waves with swiss rolls*. *Materials*, vol. 13, no. 2, page 449, 2020.
- [Acome 18] E. Acome, S. Mitchell, T. Morrissey, M. Emmett, C. Benjamin, M. King, M. Radakovitz & C. Keplinger. *Hydraulically amplified self-healing electrostatic actuators with muscle-like performance*. *Science*, vol. 359, no. 6371, pages 61–65, 2018.
- [Alekseev 19] G. V. Alekseev & D. A. Tereshko. *Particle swarm optimization-based algorithms for solving inverse problems of designing thermal cloaking and shielding devices*. *International Journal of Heat and Mass Transfer*, vol. 135, pages 1269–1277, 2019.
- [Allaire 92] G. Allaire. *Homogenization and two-scale convergence*. *SIAM Journal on Mathematical Analysis*, vol. 23, no. 6, pages 1482–1518, 1992.
- [Amjadi 18] M. Amjadi & M. Sitti. *Self-Sensing Paper Actuators Based on Graphite–Carbon Nanotube Hybrid Films*. *Advanced Science*, vol. 5, no. 7, page 1800239, 2018.
- [Arnold 12] C. Arnold, F. Marquier, M. Garin, F. Pardo, S. Collin, N. Bardou, J.-L. Pelouard & J.-J. Greffet. *Coherent thermal infrared emission by two-dimensional silicon carbide gratings*. *Physical Review B*, vol. 86, no. 3, page 035316, 2012.
- [Brandenbourger 19] M. Brandenbourger, X. Locsin, E. Lerner & C. Coulais. *Non-reciprocal robotic metamaterials*. *Nature Communications*, vol. 10, no. 1, pages 1–8, 2019.
- [Brar 15] V. W. Brar, M. C. Sherrott, M. S. Jang, S. Kim, L. Kim, M. Choi, L. A. Sweatlock & H. A. Atwater. *Electronic modulation of infrared radiation in graphene plasmonic resonators*. *Nature communications*, vol. 6, no. 1, pages 1–7, 2015.
- [Brun 09] M. Brun, S. Guenneau & A. B. Movchan. *Achieving control of in-plane elastic waves*. *Applied physics letters*, vol. 94, no. 6, page 061903, 2009.

- [Bückmann 14] T. Bückmann, M. Thiel, M. Kadic, R. Schittny & M. Wegener. *An elasto-mechanical unfeelability cloak made of pentamode metamaterials*. Nature Communications, vol. 5, page 4130, 2014.
- [Bückmann 15] T. Bückmann, M. Kadic, R. Schittny & M. Wegener. *Mechanical cloak design by direct lattice transformation*. Proceedings of the National Academy of Sciences, vol. 112, no. 16, pages 4930–4934, 2015.
- [Castaldo 19] R. Castaldo, G. C. Lama, P. Aprea, G. Gentile, V. Ambrogi, M. Lavorgna & P. Cerruti. *Humidity-driven mechanical and electrical response of graphene/cloisite hybrid films*. Advanced Functional Materials, vol. 29, no. 14, page 1807744, 2019.
- [Chandra 18] S. Chandra, D. Franklin, J. Cozart, A. Safaei & D. Chanda. *Adaptive multispectral infrared camouflage*. ACS Photonics, vol. 5, no. 11, pages 4513–4519, 2018.
- [Chen 10] H. Chen, C. T. Chan & P. Sheng. *Transformation optics and metamaterials*. Nature Materials, vol. 9, no. 5, page 387, 2010.
- [Chen 15] F. Chen & D. Y. Lei. *Experimental realization of extreme heat flux concentration with easy-to-make thermal metamaterials*. Scientific Reports, vol. 5, page 11552, 2015.
- [Cherkaev 01] E. Cherkaev. *Inverse homogenization for evaluation of effective properties of a mixture*. Inverse Problems, vol. 17, no. 4, page 1203, 2001.
- [Chin 18] S. M. Chin, C. V. Synatschke, S. Liu, R. J. Nap, N. A. Sather, Q. Wang, Z. Álvarez, A. N. Edelbrock, T. Fyrner, L. C. Palmer *et al.* *Covalent-supramolecular hybrid polymers as muscle-inspired anisotropic actuators*. Nature communications, vol. 9, no. 1, pages 1–11, 2018.
- [Christensen 15] J. Christensen, M. Kadic, O. Kraft & M. Wegener. *Vibrant times for mechanical metamaterials*. MRS Communications, vol. 5, no. 3, pages 453–462, 2015.
- [Coulais 17] C. Coulais, D. Sounas & A. Alù. *Static non-reciprocity in mechanical metamaterials*. Nature, vol. 542, no. 7642, pages 461–464, 2017.
- [Craster 18] R. V. Craster, S. Guenneau, H. Hutridurga & G. A. Pavliotis. *Cloaking via mapping for the heat equation*. Multiscale Modeling & Simulation, vol. 16, no. 3, pages 1146–1174, 2018.

-
- [Cui 18] Y. Cui, H. Gong, Y. Wang, D. Li & H. Bai. *A thermally insulating textile inspired by polar bear hair*. *Advanced Materials*, vol. 30, no. 14, page 1706807, 2018.
- [Cummer 07] S. A. Cummer & D. Schurig. *One path to acoustic cloaking*. *New Journal of Physics*, vol. 9, no. 3, page 45, 2007.
- [Deb 02] K. Deb, A. Pratap, S. Agarwal & T. Meyarivan. *A fast and elitist multiobjective genetic algorithm: NSGA-II*. *IEEE Transactions on Evolutionary Computation*, vol. 6, no. 2, pages 182–197, 2002.
- [Debenham 84] M. Debenham. *Refractive indices of zinc sulfide in the 0.405–13- μ m wavelength range*. *Applied optics*, vol. 23, no. 14, pages 2238–2239, 1984.
- [Diatta 09] A. Diatta, A. Nicolet, S. Guenneau & F. Zolla. *Tessellated and stellated invisibility*. *Optics express*, vol. 17, no. 16, pages 13389–13394, 2009.
- [Fan 08] C. Fan, Y. Gao & J. Huang. *Shaped graded materials with an apparent negative thermal conductivity*. *Applied Physics Letters*, vol. 92, no. 25, page 251907, 2008.
- [Farhat 08a] M. Farhat, S. Enoch, S. Guenneau & A. Movchan. *Broadband cylindrical acoustic cloak for linear surface waves in a fluid*. *Physical review letters*, vol. 101, no. 13, page 134501, 2008.
- [Farhat 08b] M. Farhat, S. Guenneau, S. Enoch, A. Movchan, F. Zolla & A. Nicolet. *A homogenization route towards square cylindrical acoustic cloaks*. *New Journal of Physics*, vol. 10, no. 11, page 115030, 2008.
- [Farhat 09] M. Farhat, S. Guenneau & S. Enoch. *Ultrabroadband elastic cloaking in thin plates*. *Physical Review Letters*, vol. 103, no. 2, page 024301, 2009.
- [Fleury 14] R. Fleury, D. L. Sounas, C. F. Sieck, M. R. Haberman & A. Alù. *Sound isolation and giant linear nonreciprocity in a compact acoustic circulator*. *Science*, vol. 343, no. 6170, pages 516–519, 2014.
- [Fleury 15a] R. Fleury, F. Monticone & A. Alù. *Invisibility and cloaking: Origins, present, and future perspectives*. *Physical Review Applied*, vol. 4, no. 3, page 037001, 2015.
- [Fleury 15b] R. Fleury, D. Sounas & A. Alu. *An invisible acoustic sensor based on parity-time symmetry*. *Nature communications*, vol. 6, no. 1, pages 1–7, 2015.
-

- [Florijn 14] B. Florijn, C. Coulais & M. van Hecke. *Programmable mechanical metamaterials*. Physical Review Letters, vol. 113, no. 17, page 175503, 2014.
- [Fujii 19] G. Fujii & Y. Akimoto. *Topology-optimized thermal carpet cloak expressed by an immersed-boundary level-set method via a covariance matrix adaptation evolution strategy*. International Journal of Heat and Mass Transfer, vol. 137, pages 1312–1322, 2019.
- [Fujii 20] G. Fujii & Y. Akimoto. *Cloaking a concentrator in thermal conduction via topology optimization*. International Journal of Heat and Mass Transfer, vol. 159, page 120082, 2020.
- [Gernhardt 19] M. Gernhardt, E. Blasco, M. Hippler, J. Blinco, M. Bastmeyer, M. Wegener, H. Frisch & C. Barner-Kowollik. *Tailoring the mechanical properties of 3D microstructures using visible light post-manufacturing*. Advanced Materials, vol. 31, no. 30, page 1901269, 2019.
- [Guenneau 12] S. Guenneau, C. Amra & D. Veynante. *Transformation thermodynamics: cloaking and concentrating heat flux*. Optics Express, vol. 20, no. 7, pages 8207–8218, 2012.
- [Guenneau 13a] S. Guenneau & C. Amra. *Anisotropic conductivity rotates heat fluxes in transient regimes*. Optics express, vol. 21, no. 5, pages 6578–6583, 2013.
- [Guenneau 13b] S. Guenneau & T. Puvirajesinghe. *Fick’s second law transformed: one path to cloaking in mass diffusion*. Journal of The Royal Society Interface, vol. 10, no. 83, page 20130106, 2013.
- [Haines 14] C. S. Haines, M. D. Lima, N. Li, G. M. Spinks, J. Foroughi, J. D. Madden, S. H. Kim, S. Fang, M. J. De Andrade, F. Göktepeet *al.* *Artificial muscles from fishing line and sewing thread*. Science, vol. 343, no. 6173, pages 868–872, 2014.
- [Han 10] T. Han, C. Qiu & X. Tang. *An arbitrarily shaped cloak with nonsingular and homogeneous parameters designed using a twofold transformation*. Journal of Optics, vol. 12, no. 9, page 095103, 2010.
- [Han 13] T. Han, J. Zhao, T. Yuan, D. Y. Lei, B. Li & C.-W. Qiu. *Theoretical realization of an ultra-efficient thermal-energy harvesting cell made of natural materials*. Energy & Environmental Science, vol. 6, no. 12, pages 3537–3541, 2013.

- [Han 14a] T. Han, X. Bai, D. Gao, J. T. Thong, B. Li & C.-W. Qiu. *Experimental demonstration of a bilayer thermal cloak*. *Physical Review Letters*, vol. 112, no. 5, page 054302, 2014.
- [Han 14b] T. Han, X. Bai, J. T. Thong, B. Li & C.-W. Qiu. *Full control and manipulation of heat signatures: Cloaking, camouflage and thermal metamaterials*. *Advanced Materials*, vol. 26, no. 11, pages 1731–1734, 2014.
- [Han 15a] D.-D. Han, Y.-L. Zhang, H.-B. Jiang, H. Xia, J. Feng, Q.-D. Chen, H.-L. Xu & H.-B. Sun. *Moisture-responsive graphene paper prepared by self-controlled photoreduction*. *Advanced Materials*, vol. 27, no. 2, pages 332–338, 2015.
- [Han 15b] T. Han, X. Bai, D. Liu, D. Gao, B. Li, J. T. Thong & C.-W. Qiu. *Manipulating steady heat conduction by sensu-shaped thermal metamaterials*. *Scientific Reports*, vol. 5, page 10242, 2015.
- [Han 16] D.-D. Han, Y.-L. Zhang, J.-N. Ma, Y.-Q. Liu, B. Han & H.-B. Sun. *Light-mediated manufacture and manipulation of actuators*. *Advanced Materials*, vol. 28, no. 38, pages 8328–8343, 2016.
- [Han 18] T. Han, P. Yang, Y. Li, D. Lei, B. Li, K. Hippalgaonkar & C.-W. Qiu. *Full-Parameter Omnidirectional Thermal Metadevices of Anisotropic Geometry*. *Advanced Materials*, vol. 30, no. 49, page 1804019, 2018.
- [Hippler 19a] M. Hippler, E. Blasco, J. Qu, M. Tanaka, C. Barner-Kowollik, M. Wegener & M. Bastmeyer. *Controlling the shape of 3D microstructures by temperature and light*. *Nature Communications*, vol. 10, no. 1, pages 1–8, 2019.
- [Hippler 19b] M. Hippler, E. D. Lemma, S. Bertels, E. Blasco, C. Barner-Kowollik, M. Wegener & M. Bastmeyer. *3D scaffolds to study basic cell biology*. *Advanced Materials*, vol. 31, no. 26, page 1808110, 2019.
- [Hippler 20] M. Hippler, K. Weißenbruch, K. Richler, E. D. Lemma, M. Nakahata, B. Richter, C. Barner-Kowollik, Y. Takashima, A. Harada, E. Blasco *et al.* *Mechanical stimulation of single cells by reversible host-guest interactions in 3D microscaffolds*. *Science Advances*, vol. 6, no. 39, page eabc2648, 2020.

- [Hong 20] S. Hong, S. Shin & R. Chen. *An Adaptive and Wearable Thermal Camouflage Device*. *Advanced Functional Materials*, vol. 30, no. 11, page 1909788, 2020.
- [Hu 18] R. Hu, S. Zhou, Y. Li, D.-Y. Lei, X. Luo & C.-W. Qiu. *Illusion thermotics*. *Advanced Materials*, vol. 30, no. 22, page 1707237, 2018.
- [Huang 19] S. Huang, J. Zhang, M. Wang, R. Hu & X. Luo. *Macroscale thermal diode-like black box with high transient rectification ratio*. *ES Energy & Environment*, vol. 6, pages 51–6, 2019.
- [Huang 20] T.-Y. Huang, H.-W. Huang, D. Jin, Q. Chen, J. Huang, L. Zhang & H. Duan. *Four-dimensional micro-building blocks*. *Science Advances*, vol. 6, no. 3, page eaav8219, 2020.
- [Inoue 14] T. Inoue, M. De Zoysa, T. Asano & S. Noda. *Realization of dynamic thermal emission control*. *Nature materials*, vol. 13, no. 10, pages 928–931, 2014.
- [Ji 18] Q. Ji, G. Fang & J. Liang. *Achieving thermal concentration based on fiber reinforced composite microstructures design*. *Journal of Physics D: Applied Physics*, vol. 51, no. 31, page 315304, 2018.
- [Ji 21] Q. Ji, X. Chen, J. Liang, V. Laude, S. Guenneau, G. Fang & M. Kadic. *Designing thermal energy harvesting devices with natural materials through optimized microstructures*. *International Journal of Heat and Mass Transfer*, vol. 169, page 120948, 2021.
- [Jia 09] K. Jia, S. Pal & H. Xie. *An electrothermal tip-tilt-piston micromirror based on folded dual S-shaped bimorphs*. *Journal of Microelectromechanical systems*, vol. 18, no. 5, pages 1004–1015, 2009.
- [Jiang 08] W. X. Jiang, J. Y. Chin, Z. Li, Q. Cheng, R. Liu & T. J. Cui. *Analytical design of conformally invisible cloaks for arbitrarily shaped objects*. *Physical Review E*, vol. 77, no. 6, page 066607, 2008.
- [Jiang 14] W. Jiang, D. Niu, H. Liu, C. Wang, T. Zhao, L. Yin, Y. Shi, B. Chen, Y. Ding & B. Lu. *Photoresponsive soft-robotic platform: biomimetic fabrication and remote actuation*. *Advanced Functional Materials*, vol. 24, no. 48, pages 7598–7604, 2014.

- [Kadic 11] M. Kadic, S. Guenneau, S. Enoch & S. A. Ramakrishna. *Plasmonic space folding: Focusing surface plasmons via negative refraction in complementary media*. ACS nano, vol. 5, no. 9, pages 6819–6825, 2011.
- [Kadic 13] M. Kadic, T. Bückmann, R. Schittny & M. Wegener. *Metamaterials beyond electromagnetism*. Reports on Progress in Physics, vol. 76, no. 12, page 126501, 2013.
- [Kadic 15] M. Kadic, R. Schittny, T. Bückmann, C. Kern & M. Wegener. *Hall-effect sign inversion in a realizable 3D metamaterial*. Physical Review X, vol. 5, no. 2, page 021030, 2015.
- [Kadic 19] M. Kadic, G. W. Milton, M. van Hecke & M. Wegener. *3D metamaterials*. Nature Reviews Physics, vol. 1, no. 3, pages 198–210, 2019.
- [Kadic 20] M. Kadic, M. Wegener, A. Nicolet, F. Zolla, S. Guenneau & A. Diatta. *Elastodynamic behavior of mechanical cloaks designed by direct lattice transformations*. Wave Motion, vol. 92, page 102419, 2020.
- [Kim 19] T. Kim, J.-Y. Bae, N. Lee & H. H. Cho. *Hierarchical metamaterials for multispectral camouflage of infrared and microwaves*. Advanced Functional Materials, vol. 29, no. 10, page 1807319, 2019.
- [Kohn 08] R. V. Kohn, H. Shen, M. S. Vogelius & M. I. Weinstein. *Cloaking via change of variables in electric impedance tomography*. Inverse Problems, vol. 24, no. 1, page 015016, 2008.
- [Koschny 17] T. Koschny, C. M. Soukoulis & M. Wegener. *Metamaterials in microwaves, optics, mechanics, thermodynamics, and transport*. Journal of Optics, vol. 19, no. 8, page 084005, 2017.
- [Kotikian 18] A. Kotikian, R. L. Truby, J. W. Boley, T. J. White & J. A. Lewis. *3D printing of liquid crystal elastomeric actuators with spatially programmed nematic order*. Advanced Materials, vol. 30, no. 10, page 1706164, 2018.
- [Krishna 19] A. Krishna, J. M. Kim, J. Leem, M. C. Wang, S. Nam & J. Lee. *Ultraviolet to mid-infrared emissivity control by mechanically reconfigurable graphene*. Nano letters, vol. 19, no. 8, pages 5086–5092, 2019.

- [Lee 13] S.-W. Lee, J. H. Prosser, P. K. Purohit & D. Lee. *Bioinspired hygromorphic actuator exhibiting controlled locomotion*. ACS Macro Letters, vol. 2, no. 11, pages 960–965, 2013.
- [Lee 19] N. Lee, T. Kim, J.-S. Lim, I. Chang & H. H. Cho. *Metamaterial-selective emitter for maximizing infrared camouflage performance with energy dissipation*. ACS applied materials & interfaces, vol. 11, no. 23, pages 21250–21257, 2019.
- [Li 08] J. Li & J. B. Pendry. *Hiding under the carpet: a new strategy for cloaking*. Physical Review Letters, vol. 101, no. 20, page 203901, 2008.
- [Li 09] J. Li, L. Fok, X. Yin, G. Bartal & X. Zhang. *Experimental demonstration of an acoustic magnifying hyperlens*. Nature Materials, vol. 8, no. 12, pages 931–934, 2009.
- [Li 14] Q. Li & J. S. Vipperman. *Two-dimensional acoustic cloaks of arbitrary shape with layered structure based on transformation acoustics*. Applied Physics Letters, vol. 105, no. 10, page 101906, 2014.
- [Li 15] Y. Li, X. Shen, Z. Wu, J. Huang, Y. Chen, Y. Ni & J. Huang. *Temperature-dependent transformation thermotics: From switchable thermal cloaks to macroscopic thermal diodes*. Physical review letters, vol. 115, no. 19, page 195503, 2015.
- [Li 16] T.-H. Li, D.-L. Zhu, F.-C. Mao, M. Huang, J.-J. Yang & S.-B. Li. *Design of diamond-shaped transient thermal cloaks with homogeneous isotropic materials*. Frontiers of Physics, vol. 11, no. 5, page 110503, 2016.
- [Li 18a] Q. Li & J. S. Vipperman. *Non-singular three-dimensional arbitrarily shaped acoustic cloaks composed of homogeneous parts*. Journal of Applied Physics, vol. 124, no. 3, page 035103, 2018.
- [Li 18b] Y. Li, X. Bai, T. Yang, H. Luo & C.-W. Qiu. *Structured thermal surface for radiative camouflage*. Nature communications, vol. 9, no. 1, pages 1–7, 2018.
- [Li 19a] K. Li, T.-H. Chang, Q. Xie, Y. Cheng, H. Yang, J. Chen & P.-Y. Chen. *Tunable Magnetic Response in 2D Materials via Reversible Intercalation of Paramagnetic Ions*. Advanced Electronic Materials, vol. 5, no. 6, page 1900040, 2019.

-
- [Li 19b] Y. Li, K.-J. Zhu, Y.-G. Peng, W. Li, T. Yang, H.-X. Xu, H. Chen, X.-F. Zhu, S. Fan & C.-W. Qiu. *Thermal meta-device in analogue of zero-index photonics*. *Nature materials*, vol. 18, no. 1, page 48, 2019.
- [Lim 19] T.-C. Lim. *A class of shape-shifting composite metamaterial honeycomb structures with thermally-adaptive Poisson's ratio signs*. *Composite Structures*, vol. 226, page 111256, 2019.
- [Liu 07] Z. Liu, H. Lee, Y. Xiong, C. Sun & X. Zhang. *Far-field optical hyperlens magnifying sub-diffraction-limited objects*. *Science*, vol. 315, no. 5819, pages 1686–1686, 2007.
- [Liu 10] N. Liu, M. Mesch, T. Weiss, M. Hentschel & H. Giessen. *Infrared perfect absorber and its application as plasmonic sensor*. *Nano letters*, vol. 10, no. 7, pages 2342–2348, 2010.
- [Liu 12] M. Liu, Z. Lei Mei, X. Ma & T. J. Cui. *Dc illusion and its experimental verification*. *Applied Physics Letters*, vol. 101, no. 5, page 051905, 2012.
- [Liu 15] Z. Liu, S. Fang, F. Moura, J. Ding, N. Jiang, J. Di, M. Zhang, X. Lepró, D. Galvão, C. Haines *et al.* *Hierarchically buckled sheath-core fibers for superelastic electronics, sensors, and muscles*. *Science*, vol. 349, no. 6246, pages 400–404, 2015.
- [Liu 16] X. Liu & W. J. Padilla. *Thermochromic infrared metamaterials*. *Advanced Materials*, vol. 28, no. 5, pages 871–875, 2016.
- [Liu 17] Y. Liu, W. Guo & T. Han. *Arbitrarily polygonal transient thermal cloaks with natural bulk materials in bilayer configurations*. *International Journal of Heat and Mass Transfer*, vol. 115, pages 1–5, 2017.
- [Lyu 19] J. Lyu, Z. Liu, X. Wu, G. Li, D. Fang & X. Zhang. *Nanofibrous Kevlar aerogel films and their phase-change composites for highly efficient infrared stealth*. *ACS nano*, vol. 13, no. 2, pages 2236–2245, 2019.
- [Ma 08] H. Ma, S. Qu, Z. Xu & J. Wang. *Approximation approach of designing practical cloaks with arbitrary shapes*. *Optics express*, vol. 16, no. 20, pages 15449–15454, 2008.
- [Magdanz 13] V. Magdanz, S. Sanchez & O. G. Schmidt. *Development of a sperm-flagella driven micro-bio-robot*. *Advanced Materials*, vol. 25, no. 45, pages 6581–6588, 2013.
-

- [Mak 00] M.-W. Mak & S.-Y. Kung. *Estimation of elliptical basis function parameters by the EM algorithm with application to speaker verification*. IEEE Transactions on Neural Networks, vol. 11, no. 4, pages 961–969, 2000.
- [McCall 18] M. McCall, J. B. Pendry, V. Galdi, Y. Lai, S. Horsley, J. Li, J. Zhu, R. C. Mitchell-Thomas, O. Quevedo-Teruel, P. Tassin *et al.* *Roadmap on transformation optics*. Journal of Optics, vol. 20, no. 6, page 063001, 2018.
- [Mei 07] J. Mei, Z. Liu, W. Wen & P. Sheng. *Effective dynamic mass density of composites*. Physical Review B, vol. 76, no. 13, page 134205, 2007.
- [Milton 02] G. W. Milton. *The theory of composites*. Cambridge Monographs on Applied and Computational Mathematics. Cambridge University Press, 2002.
- [Milton 06] G. W. Milton, M. Briane & J. R. Willis. *On cloaking for elasticity and physical equations with a transformation invariant form*. New Journal of Physics, vol. 8, no. 10, page 248, 2006.
- [Mirzaali 18] M. Mirzaali, S. Janbaz, M. Strano, L. Vergani & A. A. Zadpoor. *Shape-matching soft mechanical metamaterials*. Scientific Reports, vol. 8, no. 1, pages 1–7, 2018.
- [Moghimi 18] M. J. Moghimi, G. Lin & H. Jiang. *Broadband and ultra-thin infrared stealth sheets*. Advanced Engineering Materials, vol. 20, no. 11, page 1800038, 2018.
- [Narayana 12] S. Narayana & Y. Sato. *Heat flux manipulation with engineered thermal materials*. Physical Review Letters, vol. 108, no. 21, page 214303, 2012.
- [Nicolet 08] A. Nicolet, F. Zolla & S. Guenneau. *Electromagnetic analysis of cylindrical cloaks of an arbitrary cross section*. Optics letters, vol. 33, no. 14, pages 1584–1586, 2008.
- [Pakhnin 13] M. Pakhnin & T. Suslina. *Operator error estimates for homogenization of the elliptic Dirichlet problem in a bounded domain*. St. Petersburg Mathematical Journal, vol. 24, no. 6, pages 949–976, 2013.
- [Pan 20] M. Pan, Y. Huang, Q. Li, H. Luo, H. Zhu, S. Kaur & M. Qiu. *Multi-band middle-infrared-compatible camouflage with thermal management via simple photonic structures*. Nano Energy, vol. 69, page 104449, 2020.

- [Park 94] J.-S. Park. *Optimal Latin-hypercube designs for computer experiments*. Journal of Statistical Planning and Inference, vol. 39, no. 1, pages 95–111, 1994.
- [Pendry 06] J. B. Pendry, D. Schurig & D. R. Smith. *Controlling electromagnetic fields*. Science, vol. 312, no. 5781, pages 1780–1782, 2006.
- [Peng 18] L. Peng, D. Liu, H. Cheng, S. Zhou & M. Zu. *A multi-layer film based selective thermal emitter for infrared stealth technology*. Advanced Optical Materials, vol. 6, no. 23, page 1801006, 2018.
- [Peng 19] X. Peng & R. Hu. *Three-dimensional illusion thermostics with separated thermal illusions*. ES Energy & Environment, vol. 6, pages 39–44, 2019.
- [Peng 20] Y.-G. Peng, Y. Li, P.-C. Cao, X.-F. Zhu & C.-W. Qiu. *3D Printed Meta-Helmet for Wide-Angle Thermal Camouflages*. Advanced Functional Materials, page 2002061, 2020.
- [Peralta 17] I. Peralta & V. D. Fachinotti. *Optimization-based design of heat flux manipulation devices with emphasis on fabricability*. Scientific reports, vol. 7, no. 1, page 6261, 2017.
- [Petiteau 14] D. Petiteau, S. Guenneau, M. Bellieud, M. Zerrad & C. Amra. *Spectral effectiveness of engineered thermal cloaks in the frequency regime*. Scientific reports, vol. 4, page 7386, 2014.
- [Petiteau 15] D. Petiteau, S. Guenneau, M. Bellieud, M. Zerrad & C. Amra. *Thermal concentrator homogenized with solar-shaped mantle*. arXiv preprint arXiv:1508.05081, 2015.
- [Pomot 20] L. Pomot, C. Payan, M. Remillieux & S. Guenneau. *Acoustic cloaking: Geometric transform, homogenization and a genetic algorithm*. Wave Motion, vol. 92, page 102413, 2020.
- [Qin 19] J. Qin, W. Luo, P. Yang, B. Wang, T. Deng & T. Han. *Experimental demonstration of irregular thermal carpet cloaks with natural bulk material*. International Journal of Heat and Mass Transfer, vol. 141, pages 487–490, 2019.
- [Qu 17] J. Qu, M. Kadic, A. Naber & M. Wegener. *Micro-structured two-component 3D metamaterials with negative thermal-expansion coefficient from positive constituents*. Scientific Reports, vol. 7, page 40643, 2017.

- [Qu 18] Y. Qu, Q. Li, L. Cai, M. Pan, P. Ghosh, K. Du & M. Qiu. *Thermal camouflage based on the phase-changing material GST*. *Light: Science & Applications*, vol. 7, no. 1, pages 1–10, 2018.
- [Rafsanjani 19] A. Rafsanjani, K. Bertoldi & A. R. Studart. *Programming soft robots with flexible mechanical metamaterials*. arXiv preprint arXiv:1906.00306, 2019.
- [Rahm 08] M. Rahm, D. Roberts, J. Pendry & D. Smith. *Transformation-optical design of adaptive beam bends and beam expanders*. *Optics Express*, vol. 16, no. 15, pages 11555–11567, 2008.
- [Rys 19] J. Rys, S. Steenhusen, C. Schumacher, C. Cronauer & C. Daraio. *Locally addressable material properties in 3D micro-architectures*. *Extreme Mechanics Letters*, vol. 28, pages 31–36, 2019.
- [Sakat 12] E. Sakat, G. Vincent, P. Ghenuche, N. Bardou, C. Dupuis, S. Collin, F. Pardo, R. Haïdar & J.-L. Pelouard. *Free-standing guided-mode resonance band-pass filters: from 1D to 2D structures*. *Optics Express*, vol. 20, no. 12, pages 13082–13090, 2012.
- [Salihoglu 18] O. Salihoglu, H. B. Uzlu, O. Yakar, S. Aas, O. Balci, N. Kakenov, S. Balci, S. Olcum, S. Su?zer & C. Kocabas. *Graphene-based adaptive thermal camouflage*. *Nano letters*, vol. 18, no. 7, pages 4541–4548, 2018.
- [Scarcelli 11] G. Scarcelli, P. Kim & S. H. Yun. *In vivo measurement of age-related stiffening in the crystalline lens by Brillouin optical microscopy*. *Biophysical journal*, vol. 101, no. 6, pages 1539–1545, 2011.
- [Scarcelli 15] G. Scarcelli, W. J. Polacheck, H. T. Nia, K. Patel, A. J. Grodzinsky, R. D. Kamm & S. H. Yun. *Noncontact three-dimensional mapping of intracellular hydromechanical properties by Brillouin microscopy*. *Nature methods*, vol. 12, no. 12, pages 1132–1134, 2015.
- [Schittny 13] R. Schittny, M. Kadic, S. Guenneau & M. Wegener. *Experiments on transformation thermodynamics: molding the flow of heat*. *Physical Review Letters*, vol. 110, no. 19, page 195901, 2013.

- [Schittny 14] R. Schittny, M. Kadic, T. Bückmann & M. Wegener. *Invisibility cloaking in a diffusive light scattering medium*. Science, vol. 345, no. 6195, pages 427–429, 2014.
- [Schittny 15] R. Schittny, A. Niemeyer, M. Kadic, T. Bückmann, A. Naber & M. Wegener. *Transient behavior of invisibility cloaks for diffusive light propagation*. Optica, vol. 2, no. 2, pages 84–87, 2015.
- [Schurig 06] D. Schurig, J. Mock, B. Justice, S. A. Cummer, J. B. Pendry, A. Starr & D. R. Smith. *Metamaterial electromagnetic cloak at microwave frequencies*. Science, vol. 314, no. 5801, pages 977–980, 2006.
- [Shang 18] J. Shang, B. Tian, C. Jiang & J. Huang. *Digital thermal metasurface with arbitrary infrared thermogram*. Applied Physics Letters, vol. 113, no. 26, page 261902, 2018.
- [Shen 14] X. Shen & J. Huang. *Thermally hiding an object inside a cloak with feeling*. International Journal of Heat and Mass Transfer, vol. 78, pages 1–6, 2014.
- [Shen 16] X. Shen, Y. Li, C. Jiang, Y. Ni & J. Huang. *Thermal cloak-concentrator*. Applied Physics Letters, vol. 109, no. 3, page 031907, 2016.
- [Shi 17] Q. Shi, J. Li, C. Hou, Y. Shao, Q. Zhang, Y. Li & H. Wang. *A remote controllable fiber-type near-infrared light-responsive actuator*. Chemical Communications, vol. 53, no. 81, pages 11118–11121, 2017.
- [Shin 18] B. Shin, J. Ha, M. Lee, K. Park, G. H. Park, T. H. Choi, K.-J. Cho & H.-Y. Kim. *Hygrobot: A self-locomotive ratcheted actuator powered by environmental humidity*. Science Robotics, vol. 3, no. 14, 2018.
- [Siegel 01] R. Siegel. Thermal radiation heat transfer. CRC press, 2001.
- [Song 20] J. Song, S. Huang, Y. Ma, Q. Cheng, R. Hu & X. Luo. *Radiative metasurface for thermal camouflage, illusion and messaging*. Optics Express, vol. 28, no. 2, pages 875–885, 2020.
- [Spiegel 19] C. A. Spiegel, M. Hippler, A. Münchinger, M. Bastmeyer, C. Barner-Kowollik, M. Wegener & E. Blasco. *4D Printing at the Microscale*. Advanced Functional Materials, page 1907615, 2019.

- [Stenger 12] N. Stenger, M. Wilhelm & M. Wegener. *Experiments on elastic cloaking in thin plates*. Physical Review Letters, vol. 108, no. 1, page 014301, 2012.
- [Tang 20] K. Tang, X. Wang, K. Dong, Y. Li, J. Li, B. Sun, X. Zhang, C. Dames, C. Qiu, J. Yao *et al.* *A Thermal Radiation Modulation Platform by Emissivity Engineering with Graded Metal–Insulator Transition*. Advanced Materials, page 1907071, 2020.
- [Torrent 08] D. Torrent & J. Sánchez-Dehesa. *Acoustic cloaking in two dimensions: a feasible approach*. New Journal of Physics, vol. 10, no. 6, page 063015, 2008.
- [Tottori 12] S. Tottori, L. Zhang, F. Qiu, K. K. Krawczyk, A. Franco-Obregón & B. J. Nelson. *Magnetic helical micromachines: fabrication, controlled swimming, and cargo transport*. Advanced Materials, vol. 24, no. 6, pages 811–816, 2012.
- [Ueba 12] Y. Ueba & J. Takahara. *Spectral control of thermal radiation by metasurface with split-ring resonator*. Applied Physics Express, vol. 5, no. 12, page 122001, 2012.
- [Vassant 13] S. Vassant, I. Moldovan Doyen, F. Marquier, F. Pardo, U. Gennser, A. Cavanna, J.-L. Pelouard & J.-J. Greffet. *Electrical modulation of emissivity*. Applied Physics Letters, vol. 102, no. 8, page 081125, 2013.
- [Veselago 06] V. Veselago, L. Braginsky, V. Shklover & C. Hafner. *Negative refractive index materials*. Journal of Computational and Theoretical Nanoscience, vol. 3, no. 2, pages 189–218, 2006.
- [Wang 10] X. Wang, S. Qu, X. Wu, J. Wang, Z. Xu & H. Ma. *Broadband three-dimensional diamond-shaped invisible cloaks composed of tetrahedral homogeneous blocks*. Journal of Physics D: Applied Physics, vol. 43, no. 30, page 305501, 2010.
- [Wang 12] J. Wang & W. Gao. *Nano/microscale motors: biomedical opportunities and challenges*. ACS nano, vol. 6, no. 7, pages 5745–5751, 2012.
- [Wang 19] D. Wang, Y. Zhu, C. Fang, P. He & Y. Ye. *Example of metal-multi-dielectric-metal cooling metamaterial use in engineering thermal radiation*. Applied optics, vol. 58, no. 26, pages 7035–7041, 2019.
- [Xu 14] H. Xu, X. Shi, F. Gao, H. Sun & B. Zhang. *Ultrathin three-dimensional thermal cloak*. Physical Review Letters, vol. 112, no. 5, page 054301, 2014.

- [Xu 18a] C. Xu, G. T. Stiubianu & A. A. Gorodetsky. *Adaptive infrared-reflecting systems inspired by cephalopods*. *Science*, vol. 359, no. 6383, pages 1495–1500, 2018.
- [Xu 18b] G. Xu, H. Zhang & Y. Jin. *Achieving arbitrarily polygonal thermal harvesting devices with homogeneous parameters through linear mapping function*. *Energy Conversion and Management*, vol. 165, pages 253–262, 2018.
- [Xu 19a] G. Xu, X. Zhou & Z. Liu. *Converging heat transfer in completely arbitrary profiles with unconventional thermal concentrator*. *International Communications in Heat and Mass Transfer*, vol. 108, page 104337, 2019.
- [Xu 19b] G. Xu, X. Zhou & J. Zhang. *Bilayer thermal harvesters for concentrating temperature distribution*. *International Journal of Heat and Mass Transfer*, vol. 142, page 118434, 2019.
- [Xu 20] L. Xu & J. Huang. *Controlling thermal waves with transformation complex thermotics*. *International Journal of Heat and Mass Transfer*, vol. 159, page 120133, 2020.
- [Yang 13] T. Yang, L. Huang, F. Chen & W. Xu. *Heat flux and temperature field cloaks for arbitrarily shaped objects*. *Journal of Physics D: Applied Physics*, vol. 46, no. 30, page 305102, 2013.
- [Yang 15] T. Yang, X. Bai, D. Gao, L. Wu, B. Li, J. T. Thong & C.-W. Qiu. *Invisible sensors: Simultaneous sensing and camouflaging in multiphysical fields*. *Advanced Materials*, vol. 27, no. 47, pages 7752–7758, 2015.
- [Yang 17] S. Yang, L. Xu, R. Wang & J. Huang. *Full control of heat transfer in single-particle structural materials*. *Applied Physics Letters*, vol. 111, no. 12, page 121908, 2017.
- [Zangeneh-Nejad 20] F. Zangeneh-Nejad, D. L. Sounas, A. Alù & R. Fleury. *Analogue computing with metamaterials*. *Nature Reviews Materials*, pages 1–19, 2020.
- [Zhang 08] J. Zhang, Y. Luo, H. Chen & B.-I. Wu. *Cloak of arbitrary shape*. *JOSA B*, vol. 25, no. 11, pages 1776–1779, 2008.
- [Zhang 17] J. Zhang, X. A. Nou, H. Kim & G. Scarcelli. *Brillouin flow cytometry for label-free mechanical phenotyping of the nucleus*. *Lab on a Chip*, vol. 17, no. 4, pages 663–670, 2017.

- [Zhang 19] X. A. Zhang, S. Yu, B. Xu, M. Li, Z. Peng, Y. Wang, S. Deng, X. Wu, Z. Wu, M. Ouyang *et al.* *Dynamic gating of infrared radiation in a textile*. *Science*, vol. 363, no. 6427, pages 619–623, 2019.
- [Zhang 20] X. Zhang, X. He & L. Wu. *Ellipsoidal bifunctional thermal-electric transparent device*. *Composite Structures*, vol. 234, page 111717, 2020.
- [Zhou 18] S. Zhou, R. Hu & X. Luo. *Thermal illusion with twinborn-like heat signatures*. *International Journal of Heat and Mass Transfer*, vol. 127, pages 607–613, 2018.
- [Zhu 13] G. Zhu. *Designing a square invisibility cloak using metamaterials made of stacked positive-negative index slabs*. *Journal of Applied Physics*, vol. 113, no. 16, page 163103, 2013.
- [Zolla 03] F. Zolla & S. Guenneau. *Artificial ferro-magnetic anisotropy: homogenization of 3D finite photonic crystals*. In *IUTAM Symposium on Asymptotics, Singularities and Homogenisation in Problems of Mechanics*, pages 375–384. Springer, 2003.

List of Figures

I.1	The principle of transformation optics: (a) A field line in the virtual space with the background Cartesian coordinate grid shown. (b) The distorted field line in the physical space with the background coordinates distorted in the same fashion. (c) A 3D ray-tracing program has been used to show the cloaking effects. The object (in red) is hidden [Pendry 06].	3
I.2	The principle of an invisibility cloak and a concentrator for heat flux. Sketch of the transformed metric (dotted lines) for (a) an invisibility cloak and (b) a concentrator. The coating (marked in blue) is realized with metamaterials with anisotropic heterogeneous conductivity. The object is shown in red [Guenneau 12].	3
II.1	Coordinate transformation between two arbitrary tetrahedra. The virtual tetrahedral space (left) is mapped to a physical tetrahedral space (right) by linear transformation.	11
II.2	Division of a tetrahedron in coordinate transformation: (a) A general tetrahedron cloak and (b-d) the sub-domains of the cloaking domain.	13
II.3	Schematic of (a) an octahedral heat cloak and (b) its steady-state cloaking performance.	16
II.4	Dynamic cloaking performances of the octahedral cloak with the left boundary $T_1 = T_0 \exp(-t^2/2) + 1$	17
II.5	Dynamic cloaking performances of the octahedral cloak with the left boundary $T_2 = T_0 \sin(\pi t/2) + 2$	18
II.6	Schematic of (a) a polyhedral heat cloak and (b) its steady-state cloaking performance.	19
II.7	Dynamic cloaking performances of the polyhedral cloak with the left boundary $T_1 = T_0 \exp(-t^2/2) + 1$	20
II.8	Dynamic cloaking performances of the polyhedral cloak with the left boundary $T_2 = T_0 \sin(\pi t/2) + 2$	20
II.9	Diagram demonstration of (a) an tetrahedron derived from the sphere and (b) the studied tetrahedron with simplifying conditions.	21
II.10	Performances of the approximated spherical cloak with varied parameters η_1	22

II.11	Performances of the approximated cylindrical cloak with varied parameters η_1	23
II.12	Effects of the geometry parameters on cloaking performances and material properties. (a) Comparisons of perturbations between a small hollow tetrahedron and the proposed cloak. (b-d) Materials properties via varied parameters for the three sub-domains.	24
II.13	Two-dimensional polygonal cloak composed of four isotropic materials (left) and the cloaking performances (right).	25
II.14	Logarithm of the standard deviation for the measured isotherm as a function of $\log_{10}(N)$. For clarity, the values of $\log_{10}(N)$ are replaced by values of N . The convergence rate was obtained by a polynomial fit.	26
II.15	Standard deviation of the measured isotherm at different time steps with (a) varied time (b) varied number of layers.	28
III.1	Schematic representation of a possible realization of the thermal harvesting device. The shell displays some periodicity along the azimuthal direction, which is a hallmark of a concentrator. Such a device can harvest thermal energy from its surroundings. Heat flows are concentrated into the inner domain $r' < r_1$ thanks to the designed shell region $r_1 \leq r' \leq r_2$	33
III.2	Schematic illustration of 2D periodic lattices defined by 2 parameters (area fractions f_1 and f_2). We choose this microstructure to mimic the desired medium of the shell region through homogenization and optimization.	34
III.3	Potentials $V_1(x, y)$ and $V_2(x, y)$ of the illustrative case where $f_1 = 0.6576$, $f_2 = 0.0835$	35
III.4	Panels (a) and (b) show the relation between design targets (heat conductivities k_1 and k_2) and design variables (geometrical parameters f_1 and f_2). The results are obtained basing on the chosen sample points and using two-scale homogenization theory. Panels (c) and (d) show good agreement between actual values and predicted values of the heat conductivities, demonstrating the reliability of the surrogate model. The indices k_1 and k_2 denote heat conductivity of the elementary cell in the x and y directions, respectively.	37
III.5	Temperature fields in the steady state for (a) the ideal case and (b) the proposed thermal harvesting device. In both cases, heat flows are concentrated to the inner domain without much perturbations to the external thermal field.	39

-
- III.6 Comparison of temperature profiles between the harvesting device and the contrast plate along the measurement lines (a) $y = 0$ and (b) $x = r_2$. All results are obtained in the steady-state and the insets denote positions of measurement lines. We define $\Delta T = |T(x, y, z) - T_r(x, y, z)|$ to quantitatively demonstrate the heat harvesting performances. Significant heat-focusing in the inner domain ($-r_1 < x < r_1$) and minor fluctuations in external domain (along $x = r_2$) are both observed, demonstrating good heat concentrating performances. 40
- III.7 Thermal harvesting performances of the proposed device in the transient regime. (a) Temperature fields are illustrated at different times t . The performances get gradually better after a certain lapse of time. The scale bar denotes 20mm. (b) Thermal gradients of the inner domain ($\Delta T_{in} = |T_{x=r_1} - T_{x=-r_1}|$) and perturbations to external thermal field (M_V) are plotted as functions of time. The quantitative results agree well with those revealed in (a). 43
- III.8 Relation between design variables (area fractions f_1 and f_2) and the concentration efficiency. The inset shows the studied elementary cell where one material is pre-defined as $k_A = 0$ and another material is varied. In addition to material B ($k_B = 400 \text{ Wm}^{-1}\text{K}^{-1}$), we also considered material C ($k_C = 300 \text{ Wm}^{-1}\text{K}^{-1}$) and material D ($k_D = 600 \text{ Wm}^{-1}\text{K}^{-1}$) for a comparison. 44
- III.9 (a) Lamina structures defined by two material parameters (k_1 and k_2) if $L_1 = L_2$ and two additional geometrical parameters if $L_1 \neq L_2$. The optimized parameters are $k_1 = 0.26782$ and $k_2 = 3.7328$ if we impose $L_1 = L_2$. (b) Corresponding thermal harvesting performance. 44
- III.10 Additional optimized microstructures and corresponding thermal harvesting performance. (a) Elementary cell defined by two geometrical parameters $f_1 = 0.34238$, $f_2 = 0.91675$. The materials used are same with those in Fig. III.2. (b) Corresponding thermal harvesting performance. The scatters denote temperatures of the proposed device while the solid line are the temperatures from a bare plate. Following the proposed design process, we have dealt with different microstructures and obtained same thermal conductivities as $k'_r = 264 \text{ Wm}^{-1}\text{K}^{-1}$, $k'_\theta = 66 \text{ Wm}^{-1}\text{K}^{-1}$ 45
- III.11(a) Split ring structure defined by five geometrical parameters. The optimized parameters are $f_1 = 0.1037$, $f_2 = 0.1261$, $f_3 = 0.4799$, $f_4 = 0.2614$, and $f_5 = 0.0994$. (b) Corresponding thermal harvesting performance. 45
-

III.12	Fabricated samples and experimental setup. (a) Photograph of the experimental setup. (b) Blueprint of the designed thermal harvesting device. The red areas are bulk copper ($k_B = 400 \text{ Wm}^{-1}\text{K}^{-1}$) whereas the white regions denote air ($k_A = 0.026 \text{ Wm}^{-1}\text{K}^{-1}$). (c) Photograph of the sample made by CNC machining. White paint and thin PDMS layer are added on the sample to reduce surface reflectivity. The PDMS layer also acts as a heat insulating layer that reduces heat convection to the surroundings.	47
III.13	Measured temperature distributions at different times t as indicated. At $t = 0 \text{ s}$ we start from a homogeneous room temperature profile. Numerical results are shown in the left column, whereas experimental results are depicted in the right column. The white lines are isothermperature lines.....	48
III.14	Temperature distributions in the steady state for (a) a bare plate; (b) transformed parameters without considering thermal convection and emission; (c) transformed parameters considering thermal convection and emission; (d) experiments.....	49
IV.1	Illustration of the working principle of an infrared camera: capture thermal radiation of an object and transfer the detected radiation to signal voltage, and further plot contour images.	53
IV.2	Notation of electric field amplitudes within an arbitrary multilayer. The subscripts indicate the medium, the signs + and - distinguish between incident and reflected waves, respectively.	54
IV.3	(a) Schematic of the bilayer film deposited on a substrate (silicon). (b) Spectral emissivity as a function of wavelength. (c) Dependence of surface emissivity on film thickness and wavelength, obtained from Eq. (IV.10). (d) Integrated radiation power as a function of film thickness and temperature, obtained from Eq. (IV.11). The white iso-contour line depicts the radiation power of $P_{\text{obj}}(T) = 72.72 \text{ Wm}^{-2}$	55

IV.4	Outline of the process to realize thermal camouflage. (a) A continuous temperature distribution generated by a heat spot located at the center of the silicon substrate. We aim to make the detected temperatures uniform along the white center line. (b) Original temperature distribution (red line) and pseudo camera temperature (black line) observed along the center line. (b) Integrated radiation power at three typical points along the center line versus film thickness. The grey region outlines the available integrated radiation power range that is accessible to camouflage by thickness engineering. The dashed line is for $P_{\text{obj}}(T) = 72.72 \text{ Wm}^{-2}$. (d) Film thickness distribution required to obtain the apparent uniform temperature in panel b, plotted along the center line.	58
IV.5	Demonstration of different thermal functionalities. Thermal camouflage: a heat source in the background plate (see panel a1) is hidden to the IR camera (see panel a3) after thickness engineering (see panel a2). Pseudo camera temperature is $T_r = 319.8 \text{ K}$. Thermal coding: For an uniform temperature field (see panel b1), the message "HI" is observed by the IR camera instead (see panel b3). The sub-area "HI" is unchanged while the remaining area is coated with a film of thickness $0.5 \mu\text{m}$ (see panel b2). Camera temperatures of the subarea "HI" and the remaining area are $T_r = 360 \text{ K}$ and $T_r = 319.8 \text{ K}$, respectively. Thermal illusion: An original thermal image "YES" (see panel c1) is recorded as a different image "NO" in the IR camera (see panel c3). Original temperatures of the sub-area "YES" and other regions are 380 K and 360 K , while after thickness engineering camera temperatures in the sub-area "NO" and other area are 360 K and 319.8 K , respectively. For all cases, the selected radiation power is $P_{\text{obj}} = 72.72 \text{ Wm}^{-2}$	60
V.1	Illustration of the changes in bilayer beam length caused by thermal expansion.	65
V.2	Deformation of the bilayer beams. (a) Schematic of a simple single bilayer beam showing the tangential tilt end in response to a temperature change. (b) Two bilayer beams with inverted layer compositions are connected to form an S-shaped beam. (c) The proposed structure with an overlap shows no tilt angle at the end of the beams. It is also mechanically more robust.	66

-
- V.3 Illustration of the operating principle of rotational and translational stages. (a) Bi-material beam and its deformation under a change in surrounding temperature of 40 K. (b-c) Operating principle of the translational and rotational elements, respectively. The component with higher (lower) CTE is depicted in blue (gray). The initial positions of the elements are outlined for visual comparison. The directions of motion are indicated by arrows. For clarity, deformations in panel (a) and panels (b-c) are scaled by 10 times and 40 times, respectively. 67
- V.4 A microrobot consists of a three-dimensional assembly of rotational and translational elements. Along each axis, rotation and translation are produced upon temperature changes. Accumulation of these motions along each axis leads to mobility of the tip end (marked in red). The micro robotic arm can position the tip end in space controlled by external temperature changes. 68
- V.5 Illustration of controlling the motions of the microrobot by thermal stimuli: (a) a microrobot with each stack composed of five elements, (b-d) the tip end changes its position with thermally induced translation in Z , X and Y orientation, respectively. (e-f) the tip end changes its position with thermally induced rotation along Z and X orientation, respectively. As comparison, the original position is depicted by the white configuration. 69
- V.6 The CTE versus laser exposure power is obtained by measuring areas before and after heating. (a) Bulk polymer cubes written by different laser power scaling factors. (b) Outline of the general process in ImageJ to obtain areas measured in pixels: the optical image of a polymer cube in panel (c) is first converted into 8-bit format in panel (d). Then an edge detection algorithm is applied and the image is converted into a binary image in panel (e). After applying closing algorithms in panel (f) and filling algorithms in panel (g), we finally obtain the internal area defined by these edges in panel (h). 71
- V.7 Measurement of mechanical properties. (a) Schematic of the Brillouin microscope. (b) The Brillouin frequency shift ω_b of longitudinal phonons is determined as the peak of the scattered intensity. (c, d) Magnified views of the left and right peaks, where the frequency differences between different cubes are clearly observed. 72
- V.8 CTE and Young's modulus versus different laser powers. The bottom horizontal axis gives the power scaling factor whereas the top horizontal axis gives the actual power. Standard deviations are added. The CTE decreases (Young's modulus increases) with the laser exposure power. Both variations are approximately linear. 73
-

-
- V.9 Electron micrographs of (a, b) beams fabricated by single laser exposure power and (c) two-component beams fabricated using different laser powers. The beam lengths from smallest to largest are 10 μm , 20 μm , 30 μm and 40 μm , respectively. In the images, "LP" is the abbreviation of exposure laser power and the numbers denote the power scaling factors as a percentage of a nominal power. Pre-bending of the bi-material beams is observed and originates from the different volume shrinkages of the two different components during development..... 74
- V.10 Electron micrographs of cubes fabricated by the same polymer but different exposure powers. The reference power is 20 mW. The material got more porous with the increment of laser powers..... 74
- V.11 Optical micrographs of the samples showing fabrication imperfections. The larger the difference in shrinkage during development, the less resistant the beams are to ambient conditions. 75
- V.12 Functional stacks fabricated by gray-tone lithography. (a) (c) Optical micrographs and (b) (d) SEM images. Each stack is composed of five elements. The samples are composed of two constituent components fabricated with a single photoresist but two different laser exposure powers. Differential shrinkage during development leads to pre-bending of the bi-layer beams, further leading to rotation (translation) of the stack shown in the panels..... 76
- V.13 Conceptual validation of the actuation mechanism of (a) rotary lattices and (b) translation lattices. The thermal stimulus was applied on the top end of the structures by electronic beam exposure. When the thermal stimulus was set on, the structures showed overall motion; when the stimulus was set off, the relative deformation and motion disappeared gradually, demonstrating a sensitive and reversible thermal-driven process. The red cross-lines in panel (a) and the central circle are added to make deformations clearer. 77
- V.14 Temperature-dependent measurement of the fabricated stacks.(a) (c) Dependence of motional amplitudes of the stacks with the thermal gradient for rotation and translation, respectively. The plots show a symmetric, linear and reversible amplitude response. (b) (d) Cyclic stability of the structures for rotation and translation, respectively, where temperatures are switched between 25°C (marked in blue) and 45°C (marked in red). The error bars (marked in black) show the difference between experimental and numerical results. Note that the translational displacements in panels (c-d) are normalized to the initial non-heated stack length in the z -direction. . 79
-

- V.15 Influence of key parameters on motion amplitude. (a,c) Dependence of motion amplitude on thermal expansion coefficients for structures with 3, 5 and 7 layers, respectively. Note that α_1 is fixed and marked out in red, while α_2 is varied. (b, d) Dependence of motion amplitude on geometrical properties for structures with 3, 5 and 7 layers, respectively. Here we define the aspect ratio as $\lambda = \frac{L_1+L_2}{h_1+h_2}$, or the ratio between length and thickness for the bi-material beam. Geometrical nonlinearity has been accounted for..... 80
- V.16 (a,b) The specific work (i.e., the work normalized to the mass of the structure) and the actuation motion of the elements under thermal stimuli are plotted versus the normalized load and represented in analogy with Hooke's springs. Loads M_0 and M_1 have been normalized by the mass of the rotational element (2.5×10^{-10} kg) and translational element (2.1×10^{-10} kg), respectively. (c,d) Mechanical behavior of the elements. Torsion coefficients and stiffness in analogue with springs are obtained. 82

List of Tables

III.1	Accuracy of the constructed surrogate model.	37
III.2	Comparison of predicted value and targeted value for the derived set of parameters.	38
III.3	Thermal harvesting performances for different cases.	41
V.1	Comparason between theoretical, numerical and experimental results for the translational structure.	78

Titre : Métamatériaux thermiques intelligents

Mots clefs: Métamatériaux thermiques, manipulation de la chaleur, camouflage d'invisibilité

Résumé :

Cette thèse porte principalement sur les métamatériaux thermiques, y compris les méta-composants thermiques qui peuvent manipuler activement un flux de chaleur, et les métamatériaux sensibles à la chaleur qui peuvent se déformer de manière contrôlée en réponse à des stimuli thermiques externes. Nous proposons une méthode pour concevoir des capes de camouflage thermique 3D de forme arbitraire. Sur la base de cette approche, nous étudions les performances de camouflage en régime permanent et transitoire. Ensuite, nous proposons une feuille de route générale pour construire des dispositifs de récupération thermique avec une conception de la microstructure. Le dispositif est réalisé avec des matériaux naturellement disponibles. Les résultats tant numériques qu'expérimentaux démontrent

de bonnes performances de récupération thermique. En plus des travaux mentionnés ci-dessus sur le contrôle de la conduction thermique dans le plan, nous proposons également une approche de milieu multicouche pour manipuler de manière flexible le rayonnement thermique hors plan. Sur la base de cette approche, nous réalisons des fonctionnalités telles que le camouflage infrarouge, le codage thermique et l'illusion thermique. Enfin, nous proposons des métamatériaux thermomécaniques capables de générer des déformations élémentaires (translation et rotation) en réaction à des stimuli thermiques. Nous vérifions que les performances induites sont thermiquement précises, stables et réversibles par des simulations et des expériences. Le comportement d'actionnement est également étudié.

Title : Thermally driven smart metamaterials

Keywords : Thermal metamaterials, heat manipulation, invisibility cloaking

Abstract :

This thesis mainly focuses on thermal metamaterials, including thermal metadevices that can actively manipulate heat flux, and thermally responsive metamaterials that can deform in response to external heat stimuli in a controlled manner. We propose a method to design arbitrarily shaped 3D thermal cloaks with anisotropic and homogeneous material properties. Based on this approach, we study the steady-state and transient cloaking performance of multilayered cloaks. Then we propose a general road map to build thermal harvesting devices with microstructure design. The device is realized by naturally available materials. Both numerical and experimental re-

sults demonstrate good thermal harvesting performance. In addition to the above mentioned works on in-plane heat conduction control, we further propose a multilayered medium approach to flexibly manipulate out-of-plane thermal radiation. Based on this approach we realize functionalities like infrared camouflage, thermal coding and thermal illusion. Finally, we propose thermomechanical metamaterials that can generate basic deformations (translation and rotation) in reaction to heat stimuli. We verify their accurate, stable and reversible thermally induced performance by simulations and experiments. Actuation operation is also investigated.